A Novel Semi-Active Control Approach for Flexible Structures: Vibration Control through Boundary Conditioning using Magnetorheological Elastomers

Jomar Christopher Morales

A Thesis

In the Department of

Mechanical, Industrial, and Aerospace Engineering

Presented in Partial Fulfillment of the Requirements

For the Degree of

Master of Applied Science (Mechanical, Industrial, and Aerospace Engineering)

At Concordia University

Montreal, Quebec, Canada

August 2023

CONCORDIA UNIVERSITY

SCHOOL OF GRADUATE STUDIES

This is to certify that the thesis prepared

By: **Jomar Christopher Morales**

Entitled: **A Novel Semi-Active Control Approach for Flexible Structures: Vibration Control through Boundary Conditioning using Magnetorheological Elastomers**

and submitted in partial fulfillment of the requirements for the degree of

Master of Applied Science (Mechanical Engineering)

complies with the regulations of the University and meets the accepted standards with respect to originality and quality.

Signed by the final Examining Committee:

_____ Chair

Dr. Behrooz Yousefzadeh

_____ Examiner

Dr. Behrooz Yousefzadeh

_____ Examiner

Dr. Fariborz Haghighat

_____ Supervisor

Dr. Ramin Sedaghati

Approved by   _____

Dr. Sivakumar Narayanswamy, Graduate Program Director

October 31, 2023   _____

Dr. Mourad Debbabi, Dean
Gina Cody School of Engineering and Computer Science

ABSTRACT

A Novel Semi-Active Control Approach: Vibration Control through Boundary Conditioning using Magnetorheological Elastomers

Jomar Christopher Morales

Magnetorheological elastomers (MREs) are solid analogue of the well-known smart material magnetorheological fluids (MRFs). They are composed of micron-sized ferromagnetic particles embedded in an elastomeric medium. Compared to MRFs which generally provide variable damping by variation of an applied magnetic field, MREs are capable of altering both stiffness and damping in the presence of an external magnetic field. The field-dependent viscoelastic properties of MREs can be effectively used for the development of MRE-based adaptive devices and structures to mitigate vibration semi-actively over a broad range of frequencies.

Extensive research studies have been carried out on the application of MREs in semi-active vibration isolators and absorbers. One emerging application is the use of MREs as part of structures, such as MRE-based sandwich beams and plates, with MRE acting as the core layer. MRE-based sandwich structures may be used for vibration control of light-weight flexible structures; however, their practical implementation is limited partially due to the weight of the integrated electromagnet having to be mounted onto these vibrating structures in order to activate the MRE layer.

This research explores an alternative method of vibration control of flexible beam type structures via boundary conditioning using MRE at the support location. Having the MRE at the beam support rather than the core layer resolves the mounting issue of the electromagnet on the structure itself. This study explores a novel MRE-based control method on a cantilever beam, where the cantilever beam is approximately modelled using an overhanging flexible continuous beam. The overhang support is replaced with MRE support to control the rigidity of the boundary condition. The Rayleigh-Ritz method has been effectively used to formulate dynamic equations of motions of the beam with MRE support and to extract its natural frequencies and mode shapes. The MRE based adaptive continuous beam is then converted into an equivalent single-degree-of-freedom system for the purpose of control implementation, assuming that the system's response is dominated by its fundamental mode. Three different types of control methods are explored

including optimal control based on nonlinear mathematical programming technique (NLP), proportional-integral-derivative control, and on-off control. The performance of controllers is evaluated for three different loading conditions including shock, harmonic and random vibration excitations.

The proposed method of vibration control through boundary conditioning using MRE technology can provide essential guidance on the vibration control of light-weight structures using MREs without directly integrating heavy electromagnets to energize MREs. Such a design can be retroactively fitted onto an existing structure. Applications can include electronics packaging, where the electromagnet can be placed at a safe distance from electronics that are sensitive to a magnetic field.

Acknowledgement

Firstly, I would like to thank Dr. Sedaghati for giving me this research opportunity. His guidance along the way has been very helpful as I try and achieve my academic goals. His help made me feel more confident in my research capabilities and writing skills. I can never express enough gratitude for his patience and mentorship throughout this process.

I would like to also thank all my past professors for all the knowledge they have imparted to me. Without them, I would not have been able to advance my knowledge and accomplish this research.

I would also like to thank my parents for their constant push for me to do well in my studies. Without their encouragement, I would not have the drive I have today in pursuing my studies. They were always there to recognize and remind me of my skills.

Last and most importantly, I would like to thank my wife for her endless support and love as I continue to pursue my dreams. Her sacrifice in helping me focus on my research is what helps me continue on working towards our goals.

Dedication

This thesis is dedicated to my wife.

for her continual love, support, and encouragement

throughout all the years in my pursuit for education.

Table of Contents

List of Figures

List of Tables

Chapter 1: Introduction

1.1 Overview

Structural integrity and the implications on users are factors that must be considered in engineering design. Structural integrity includes machines running for a required specific number of cycles under vibratory loads, where the number of cycles can be significantly decreased under harsher conditions. These dynamic, vibration-inducing loads can cause negative effects on many engineering systems and their users. For example, seismic loadings can cause major damage to building structures and is a definite danger to people within the building. Another example is the vibration caused by a vehicle travelling on rough terrain, where the vibration is a source of human discomfort but also a source of high stress levels on the vehicle structure. Vibration control, therefore, becomes crucial in preserving structural integrity, enhancing operational efficiency, and ensuring human comfort in various industries, from construction and manufacturing to transportation and electronics.

Vibration control is an ongoing research topic and generally categorizes into passive, fully active, and semi-active control strategies. Passive vibration absorbers and isolators are generally designed and tuned for a particular frequency. While passive systems are reliable and cost effective, they have performance limitation under mistuned conditions and varying excitation conditions. Fully active vibration control can be accomplished through destructive interference between an external disturbance and the out-of-phase vibration from an active actuator [1]. Alternatively, vibration control can be done semi-actively through tunable vibration isolators and absorbers, which can be achieved through smart materials capable of changing their mechanical properties. Semi-active systems are generally fail-safe and have the reliability of passive systems while they maintain adaptability of fully active systems to suppress vibration for a broad range of frequencies.

Magnetorheological elastomers (MREs) are an emerging multifunctional smart material that are able to change their mechanical properties in the presence of a magnetic field. The ability to change both stiffness and damping in the presence of a magnetic field is called the magnetorheological effect, which is possible due to the construction of the MRE. MRE is composed of micron-sized ferromagnetic particles embedded into a polymeric medium. The polymeric medium gives the MRE the viscoelastic properties; however, the behavior of the

ferromagnetic particles in the presence of a magnetic field is what causes the viscoelastic properties to change. Upon application of a magnetic field, the magnetic dipoles attempt to align themselves along the direction of an external magnetic field. This realignment of particles leads to a reversible alteration in the material's viscosity and stiffness, allowing for dynamic tunability and adaptability in its mechanical behavior. This unique feature enables MREs to be effectively used in the development of adaptive semi-active control devices and systems. The application of MREs has been extensively explored in adaptive tunable vibration absorbers (ATVAs) and isolators in semi-active suspension [2]–[12]. However limited studies have been conducted on vibration control of flexible structures using MREs. Recently, MRE has been used in flexible sandwich structures as the core layer [13]–[22]. However, the practical implementation of MRE-based sandwich structures has become limited due to integration of the bulky electromagnet within the flexible structures.

The purpose of this dissertation is to present a novel approach in the control of flexible structures through boundary conditioning using MRE. In this study, a cantilever beam with MRE at the support location has been studied to demonstrate the proof-of-concept. The system design requires a material model of the MRE capable of predicting its field-dependent mechanical properties accurately. The electromagnet should be properly designed to activate the MRE in the active regions close to its saturation limit to provide the maximum magnetorheological (MR) effect. Following the modeling and analysis of the electromagnet, the MRE-based cantilever beam should be properly modeled and designed. This includes determining the beam configuration using MRE at the support and determining the dimensions such that it compares well with the cantilever beam and that the beam experiences a sufficient frequency shift. Finally, an appropriate control system should be developed for the proposed design configuration.

A general overview of modeling, analysis and control of the vibration system is provided in Section 1.2. It is required to establish mathematical models to properly capture the physics of the vibratory system. Such mathematical models can fall into different categories requiring different analytical techniques to understand their behavior. These mathematical models include the input-output and state-space models and can be further subcategorized as linear time-invariant (LTI) or linear time-varying (LTV) systems. The behavior of these systems depends on the type of loading considered, such as shock, harmonic, or random loads. The response behavior due to these loads are studied in either the time domain or the frequency domain. Understanding the behavior of the

vibratory systems help in designing a control strategy to mitigate the vibration. Numerous control techniques are available, and their applicability relies on the specific mathematical model employed. These control techniques can be categorized as passive, active, and semi-active control. There exist many different controller laws that have been applied using MRE and some of these are to be explored, such as the proportional-integral-derivative (PID) and on-off controllers.

Section 1.3 discusses, in detail, the dependency of the mechanical properties of MREs to their micro-structural behavior. This discussion includes the static and dynamic behavior of the ferromagnetic particles in the presence of a magnetic field, which has an overall impact on the MREs stiffness and damping. Applications of MRE in semi-active vibration control is discussed in full detail, which will demonstrate the lack of control methods for flexible structures. Section 1.4 introduces the current research study which aims at control of flexible structures through boundary conditioning using MRE. The organization of this dissertation is finally outlined in section 1.5.

1.2 Modelling, Analysis, and Control of Vibratory Systems

The foundation for understanding the response of any physical system lies in the development of appropriate mathematical models that can effectively describe the system's response behavior. Mathematical models are used to capture the vibrational behavior of a system subject to different loading conditions. Generally, any vibrating system can be described by a governing second-order ordinary differential equation (ODE) combining the effects of the inertial, damping, and stiffness forces. The system can further be excited through some external loading, $F(t)$. The differential equation can thus be expressed in general form as:

$$m\ddot{x} + c\dot{x} + kx = F(t) \tag{1-1}$$

In which m, c, and k represent the system mass, damping, and stiffness. A system can respond differently depending on the type of dynamic load, where some common types of loads include shock, step, harmonic, and random loads. The response behavior of a vibratory system can be well understood by evaluating its response in time and frequency domains. Understanding the response of a vibration system will greatly facilitate in determining methods of suppressing the vibration to comfortable and safe limits.

1.2.1 Mathematical Modelling

Different modelling techniques exist to represent the system. Classical control theory considers the differential equation to be of the input-output form, where the output is simply a direct function of the input. The single-input-single-output (SISO) equation is generally formulated in the following general manner:

$$a\ddot{x} + b\dot{x} + c = f(t) \tag{1-2}$$

The input-output equation is useful in transfer function analysis, which is a frequency-based analysis. The Laplace transform is a useful tool in converting a system from the time domain to the frequency domain. By taking the Laplace transform of Eqn. (1-2), the transfer function, $T(s)$, of the system can be derived as:

$$T(s) = \frac{X(s)}{F(s)} = \frac{1}{as^2 + bs + c} \tag{1-3}$$

Transfer function analysis is a useful method in understanding the behavior of the system in the frequency domain. The system's performance characteristics can be understood through analysis of the denominator of the transfer function, which represents the characteristic equation.

Modern control theory is based on state-space modelling and provides deeper insight into the system's controllability and observability [23]. State-space modelling is a time-based approach and is formulated as a set of differential equations, generally formulated as:

$$\begin{aligned} \dot{x} &= Ax + Bu \\ y &= Cx + Du \end{aligned} \tag{1-4}$$

where A is the system matrix, B is the control matrix, C is the output matrix, D is the feed-forward matrix, x is the vector of state-variables, u is the vector of inputs, and y is the vector of outputs [23], [24]. Generally, the feed-forward matrix is only included when using feed-forward control methods; hence, the feed-forward matrix will be considered zero when using feed-back control methods.

Classifying a system as linear time-invariant (LTI) or linear time-varying (LTV) leads to other analytical and control methods. An LTI system considers that the coefficients in the governing differential equation be all constant, as shown in Eqn. (1-4). An LTV system is one that has its coefficients varying with time, and can be generally formulated as:

4

$$\dot{x} = A(t)x + B(t)u$$
$$y = C(t)x + D(t)u \qquad \text{(1-5)}$$

LTI systems are generally understood and can be analyzed using the methods described in the following subsection. LTI systems can be represented by both transfer function and state-space modelling. Due to the nature of LTV systems, they can only be represented by state-space modelling since applying the Laplace transform on such systems may prove difficult or impossible. Hence, analytical and control techniques relevant to transfer functions are inapplicable.

In regards to vibratory systems, the coefficients of the differential equations formulated by either using Eqn. (1-2) or (1-4) largely depend on the system mass, spring, and damping elements. If a system has variable stiffness and damping, such as the case of a field-controlled vibration absorber or isolator, then the system is considered LTV. Hence, semi-active systems inherit the analytical complexities of LTV systems.

1.2.2 Analysis

Understanding the behavior of a vibratory system provides essential information in selecting components with specific stiffness and damping properties, and an appropriate control strategy to attenuate vibration. Analytical methods have been well-established for LTI systems; however, LTV systems require numerical or approximative methods. This section will go over the standard analytical methods such as time-response and frequency-response and will demonstrate the difficulties to apply the same methods to LTV systems.

1.2.2.1 Time-Response

By definition, the time response is the solution to the differential equation described in Eqn. (1-1), where the complete response is composed of a homogeneous solution and a particular solution. For instance, for a single-degree-of-freedom (SDOF) system, this can be described as:

$$x(t) = x_h(t) + x_p(t) \qquad \text{(1-6)}$$

The homogeneous, or free vibration response, is dependent on the characteristic equation and the initial conditions. For any second-order SDOF system, the generalized characteristic equation is defined by its natural frequency, ω_n, and damping ratio, ζ, and is formulated in the frequency domain as:

$$s^2 + 2\zeta\omega_n s + \omega_n^2 = 0 \qquad \text{(1-7)}$$

5

The form of the homogeneous solution is dependent on the damping ratio, and can be classified as either being undamped, underdamped, overdamped, or critically damped. Only the underdamped scenario is of particular interest since this case presents itself with oscillatory motion, which is characteristic of vibration. The free vibration response for the underdamped case can then be described as [25]:

$$x_h(t) = e^{-\zeta \omega_n t} \left[x(0) \cos \omega_d t + \frac{\dot{x}(0) + x(0)\zeta \omega_n}{\omega_d} \sin \omega_d t \right] \tag{1-8}$$

where ω_d is the damped natural frequency, and $x(0)$ and $\dot{x}(0)$ are the initial position and initial velocity, respectively. The particular, or forced, response is dependent on the type of loading used. In general, the particular response is derived using Duhamel's integral, which is a convolution integral between the forcing function and the impulse function. Duhamel's integral for a damped system is written as the following [25]:

$$x_p(t) = \int_0^t \frac{1}{\omega_d} e^{-\zeta \omega_n (t-\tau)} \sin \omega_d (t - \tau) F(\tau) d\tau \tag{1-9}$$

Combining the homogeneous and particular solutions expressed in Eqns. (1-8) and (1-9) into the complete response in Eqn. (1-6) gives the time response dependent on both initial conditions and external forcing as:

$$
\begin{aligned}
x(t) = e^{-\zeta \omega_n t} &\left[x(0) \cos \omega_d t + \frac{\dot{x}(0) + x(0)\zeta \omega_n}{\omega_d} \sin \omega_d t \right] \\
&+ \int_0^t \frac{1}{\omega_d} e^{-\zeta \omega_n (t-\tau)} \sin \omega_d (t - \tau) F(\tau) d\tau
\end{aligned}
\tag{1-10}
$$

The total response can also be derived from state-space modelling, which is generalized for LTI and LTV systems as [23]:

$$x(t) = \mathbf{\Phi}(t, t_0)x(t_0) + \int_{t_0}^t C(t)\mathbf{\Phi}(t, \tau)B(\tau)u(\tau) \, d\tau + D(t)u(t) \tag{1-11}$$

where the state transition matrix, $\mathbf{\Phi}$, is a function of the state coefficient matrix [23]:

$$\mathbf{\Phi}(t, \tau) = e^{(t-\tau)A}$$

The state transition matrix can easily be determined for LTI systems, however, determining the state transition matrix for an LTV system is only possible using numerical or approximative techniques [23]. One simple method of dealing with LTV systems is by discretizing the time domain, such that time-dependent coefficient matrices can be considered constant over the time-step, as shown in Figure 1-1. This particular technique will be used in this research study to understand the time-response of the nonlinear time variant MRE-based semi-active control system.
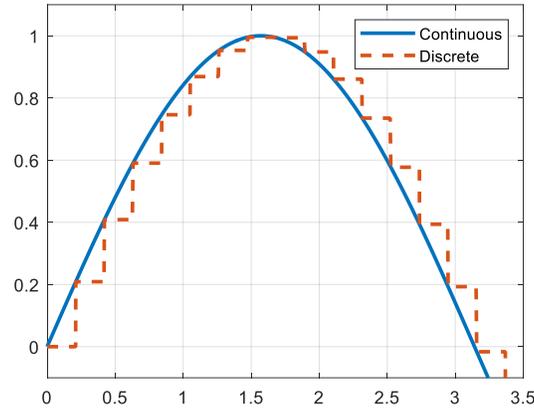
Figure 1-1: Example of the Discretization of a Continuous Function with a Constant Value over the Time Interval

The purpose of the time response is to understand the oscillatory behavior over time when disturbed by some input excitation. Generally, the time response is of interest when applying a shock or step load to the system. Shock loads are of particular interest as these are commonly occurring, for example, in a vehicle driving over a bump or bird strike on an aircraft. Specifically, the time response of an underdamped second-order system to a step input, as shown in Figure 1-2, is of interest as they provide key parameters describing how the vibrational system behaves over time. Performance characteristics have been well-defined for second-order underdamped systems and the performance characteristics of interest are defined as follows [24]:

- Natural frequency, ω_n: The frequency at which the system naturally oscillates without any external load. It is also the frequency at which resonance occurs under a harmonic input. It can be obtained by:

$$\omega_n = \sqrt{\frac{k}{m}} \tag{1-12}$$

7

- Damping ratio, ζ: A non-dimensional parameter comparing the system's damping coefficient to that of the critically damped. A system is considered underdamped if its damping ratio is less than 1. The damping ratio can be described as:

$$\zeta = \frac{c}{2m\omega_n} \qquad (1\text{-}13)$$

- Damped natural frequency, ω_d: Similar to the natural frequency, however, for damped systems. It is defined as:

$$\omega_d = \omega_n\sqrt{1 - \zeta^2} \qquad (1\text{-}14)$$

- Peak response, M_{pt}: The value of the first oscillatory peak attained by the system. It is formally defined as:

$$M_{pt} = 1 + \exp\left(-\frac{\zeta\pi}{\sqrt{1 - \zeta^2}}\right) \qquad (1\text{-}15)$$

- Percent overshoot, $\%OS$: It is defined as the percent difference of the peak response and the target value as:

$$\%OS = 100 \exp\left(-\frac{\zeta\pi}{\sqrt{1 - \zeta^2}}\right) \qquad (1\text{-}16)$$

- Settling time, T_s: The time taken to reach within 2% of the target value at steady-state. It is defined as:

$$T_s = \frac{4}{\zeta\omega_n} \qquad (1\text{-}17)$$

- Steady-state error, e_{ss}: Defined as the steady-state difference between some reference or target signal, $r(t)$, and the output signal, $y(t)$. The steady-state error may also be referred to as tracking error, and is defined as:

$$\lim_{t\to\infty} e_{ss}(t) = r(t) - y(t) \qquad (1\text{-}18)$$

The peak response, percent overshoot and settling time defined above are based on assuming that the final value of the output is unity under step input. The percent overshoot is not applicable for impulse inputs since, in this case, the final target value is zero which results in an undefined percent

overshoot. The peak value is generally an appropriate figure of merit for characterization of the time response under shock loading.

Some controller types tend to increase the order of the characteristic equation while maintaining second-order underdamped behavior, yet the definitions of the above performance characteristics are only applicable for a second-order underdamped system. For such cases, a more general method is used to measure the same performance characteristics, which can be conducted by measuring those performance characteristics from the time response signal directly. Case in point is the classical PID controller, which will be discussed in the next section, which attempts to control the performance characteristics while changing the order and nature of the characteristic equation.
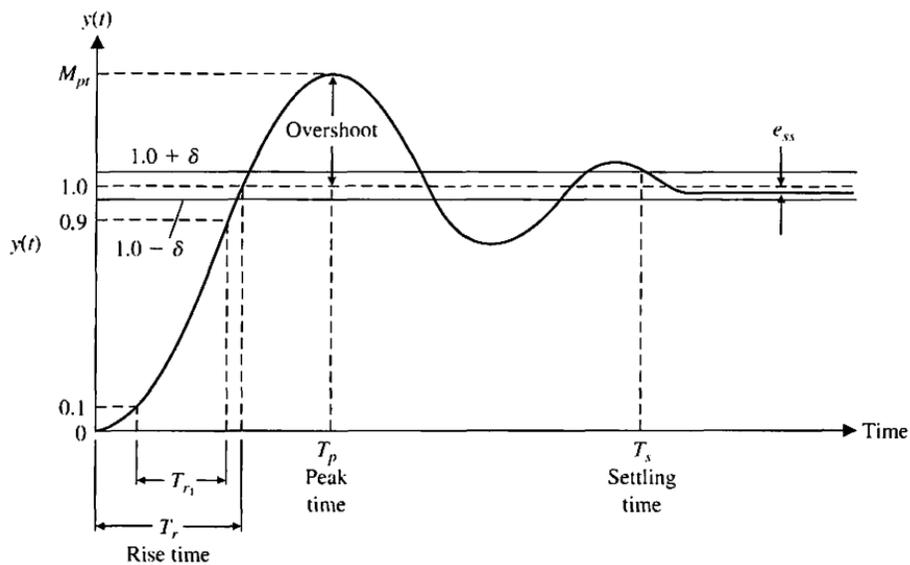
Figure 1-2: Second-Order Underdamped System Transient Response and Performance Characteristics to a Unit Step Input [24]

The performance characteristics of the time response can be obtained alternatively through frequency-response methods by simply analyzing the characteristic equation, which is the denominator of the transfer function. The roots of the characteristic equation are called poles, which strongly influence the behavior of the system. These poles have the general form of [24]:

$$s = -\zeta\omega_n \pm j\omega_d \tag{1-19}$$

which shows that they are dependent on the performance characteristics. Furthermore, the general form shows that the real component has a direct impact on the settling time. The pole location is

also useful in judging the stability of any system since it is required that poles remain in the left-hand side of the complex plane such that the overall system is stable. Figure 1-3 shows the transient behavior based on pole placement. Since poles are complex numbers in nature, the real component affects the decay rate of the response, while the complex part affects the frequency of oscillation.
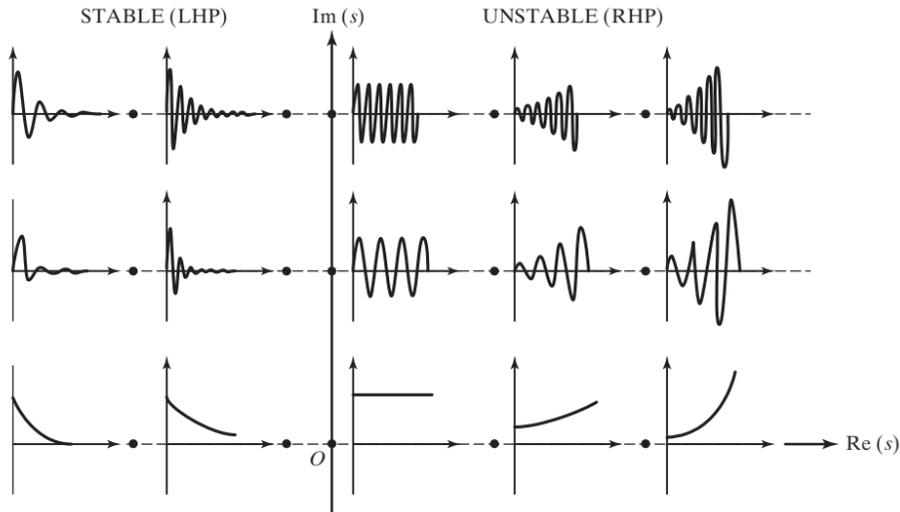
Figure 1-3: Effect of Pole Location on the Transient Behavior of a Dynamic System [25]

For a vibratory system, pole location, first and foremost, is dependent on the selection of the mass, spring, and damper, as this has a direct impact on the characteristic equation. However, systems with tunable springs and dampers have a variable characteristic equation causing the performance characteristics to change over time. Mathematically, a second-order system can only be unstable if there is any sign change in the coefficients. Physically, this means having either a negative mass, stiffness, or damping, which is impossible. Generally, it is impossible for a passive system to be unstable. Active feedback control systems are capable of becoming unstable since application of feedback along with a controller changes the overall transfer function, and consequently, the pole location. However, semi-active control systems do not become unstable since feedback only controls the coefficients of the characteristic equation, thus having a similar stability reasoning as passive systems.

In regards to vibration control, attenuation can be achieved by considering decreasing the settling time and percent overshoot. By decreasing the settling time, this reduces the time the structure experiences oscillatory motion. Structural failure can come in the form of fatigue and decreasing the number of cycles by decreasing the settling time can increase the life of the structure.

10

By decreasing the percent overshoot, the maximum amplitude of vibration during the transient response is also decreased. This has the effect of lowering the maximum stress experienced in the structure, thus preventing possible structural failure. Overall, the lowering of these two performance characteristics can increase the life of a structure in terms of fatigue failure.

1.2.2.2 *Harmonic Response*

Harmonic loading is sinusoidal in nature and can be produced by an unbalanced rotating machine, periodic vortex shedding from a flow on a blunt body, or sinusoidal road terrain. One dangerous phenomenon in vibrational systems is resonance, where the system continually increases its amplitude of oscillation over time thus vibrating in an unstable manner. This phenomenon will always lead to mechanical failure of the system and should be avoided.

The harmonic response is a method to predict the amplitude of vibration and provides a functional relationship between the amplitude of vibration and the applied frequency. The harmonic response can determine whether the oscillations are amplified or attenuated, as shown in Figure 1-4(a). Damping prevents the system from having unstable oscillations when operating near the system's natural frequency; however, damping also causes a phase shift between the input load and the state output, as shown in Figure 1-4(b).

The harmonic response for a harmonic force input can be mathematically described as:

$$x_p(t) = X e^{i\omega t} \tag{1-20}$$

$$F(t) = F e^{i\omega t} \tag{1-21}$$

By replacing Eqns. (1-20) and (1-21) into Eqn. (1-1), the receptance transfer function, $H(\omega)$, defined as the ratio of output displacement magnitude, X, to the input force magnitude, F, can be obtained as:

$$H(\omega) = \frac{X}{F} = \frac{1}{k - m\omega^2 + ic\omega} \tag{1-22}$$

Eqn. (1-22) can further be non-dimensionalized by considering the damping and frequency ratios. The frequency ratio, r_n, is defined as the operating frequency normalized by the natural frequency, which is formulated as:

$$r_n = \frac{\omega}{\omega_n} \tag{1-23}$$

11

Factoring k from the denominator of Eqn. (1-22) and rearranging leads to the non-dimensional transfer function, which is formulated as:

$$\frac{kX}{F} = \frac{1}{1 - r_n^2 + i2\zeta r_n} \tag{1-24}$$

Eqn. (1-24) provides a non-dimensional description of the behavior of the system as a function of the frequency ratio and damping factor. It can also be described as the ratio of the forced transferred, $F_T = kX$, to the force applied, or the ratio of the amplitude of vibration to the static deflection, $\delta_{st} = F/k$. For undamped systems, where $\zeta = 0$, resonance will occur where the amplitude of vibration approaches infinity as r_n approaches 1.
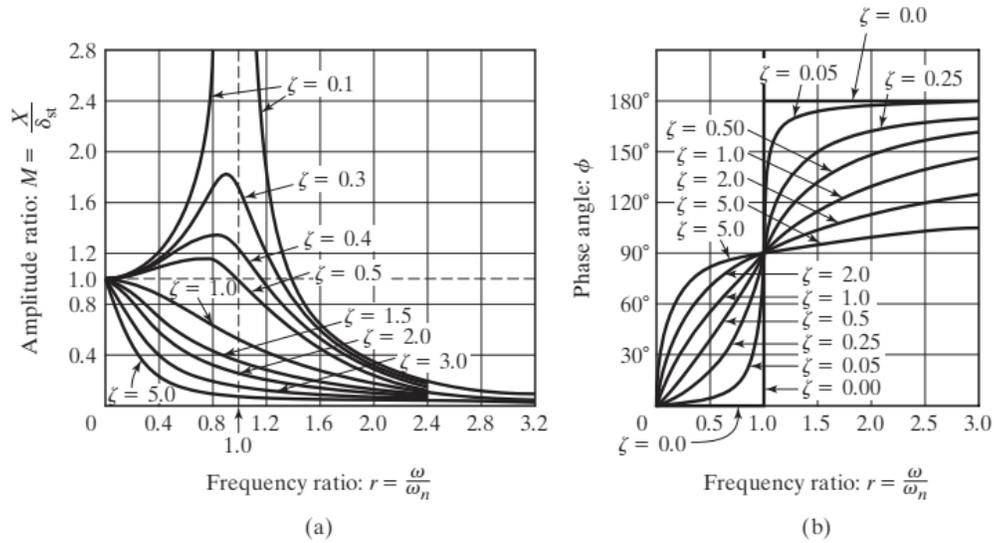
Figure 1-4: Non-dimensional Amplitude Ratio (a) and Phase (b) Frequency Response

Because LTV MRE-based systems have tunable stiffness and damping, they are able to change their natural frequency and damping when being influenced by an external magnetic field. One interesting result of an LTV system having tunable stiffness and damping is that the natural frequency can be shifted away from the input excitation frequency, thus escaping resonance. For LTI systems, frequency response analysis is useful in tuning passive vibration absorbers and isolators assuming that the operating frequency is known. However, predicting a specific operating frequency may be difficult, thus the tuning can be done to attenuate vibration over a predicted narrow bandwidth of frequencies. Tuning is achieved by selecting the right stiffness and damping to attenuate vibration. On the other hand, LTV systems can be designed to actively tune the springs and dampers. Decreasing the amplitude, as discussed previously, will increase the structural life by

decreasing stress levels. Therefore, MRE-based semi-active systems can provide a cheap and simple method of attenuating vibration over an unpredicted broadband of input frequencies.

1.2.2.3 Spectral Analysis and Random Loads

Random loads are another common type of loading, and unlike shock and harmonic loads, random loads are non-deterministic in nature. Random loads can be experienced on a vehicle travelling on rough terrain, on a building subject to seismic activity, or on an airplane wing due to turbulent flows. Because they are non-deterministic, time-based statistical methods are utilized in understanding the effects of random loads. Further understanding can also be done by observing the frequency-based power spectral density (PSD), $S(\omega)$, which is defined as a power distribution across a spectrum of frequencies. Random loads can be represented by their PSD, as shown in Figure 1-5(a). One common type of random load is that of white noise, which in an ideal case has a PSD showing constant power over all frequencies, as shown in Figure 1-5(b).
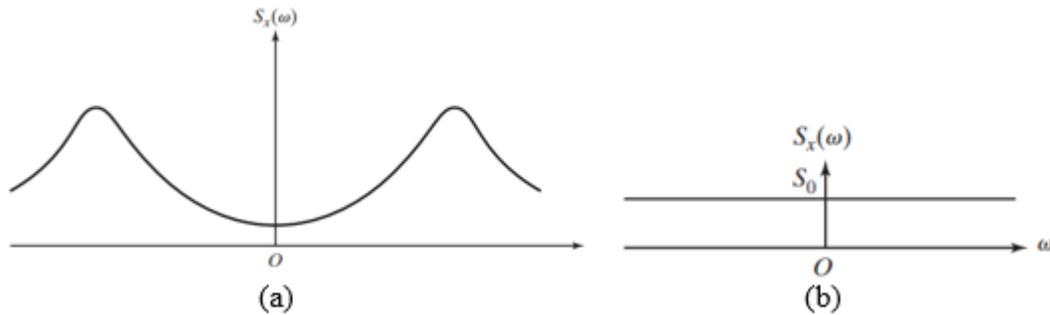
Figure 1-5: Power Spectral Density of a General Random Load (a) and White Noise (b) [25]

The response of the system under random loads requires the transfer function defined in Eqn. (1-22). The PSD of the response is related to the PSD of the load through the square of the magnitude of the transfer function as [26]:

$$S_y(\omega) = |H(\omega)|^2 S_x(\omega) \tag{1-25}$$

Application of Eqn. (1-25) is only possible if the transfer function can be derived. LTI systems can easily provide the required transfer function; however, the transfer function for an LTV system can be difficult or even impossible to obtain. Therefore, analytical methods to determine the spectral response, $S_y(\omega)$, may not be applied for LTV systems. Alternatively, the fast Fourier transform

13

(FFT) can be used to determine the PSD by sampling the time response signal and converting to the frequency domain.

From a statistical point of view, the variance of a random process is defined as:

$$\sigma^2 = E[X^2] - (E[X])^2 \tag{1-26}$$

If the random load has a mean of approximately zero, then the mean can be neglected. Therefore, the variance of a response is equivalent to the mean square value and thus can be formulated using the PSD of the response as:

$$\sigma_y^2 = E[X_y^2] = \int_{-\infty}^{\infty} S_y(\omega)\, d\omega \tag{1-27}$$

Therefore, for a zero-mean random process, the standard deviation, or root-mean-square (RMS) value is a parameter of interest for vibration response due to random loads.

1.2.3 Control Strategies

Vibrations caused by dynamic loads have been controlled in various ways. Passive control is used in vibration isolation techniques, where generally passive rubber pads are placed between the vibrating foundation and the payload. The rubber pads would dampen the motion transmitted from the foundation to the payload. Passive control techniques do not require an additional system to control vibration, but they require a prior knowledge of the loading scenario in order to properly determine the stiffness and damping of the isolator such that the vibration of the payload is attenuated to acceptable levels at a given frequency. Essentially, knowledge of the frequency response will help in tuning of the isolator by designing the pads such that the natural frequency lies outside the expected excitation frequency bandwidth.

Another form of vibration control is through active and semi-active control systems, which use external inputs to suppress vibration. Such types of controllers are preferable over the passive system since they can suppress vibrations due to unexpected loads occurring over a wide range of frequencies. Active control uses external loads from actuators to mitigate the vibration. The active control strategy provides significant performance gain compared with passive systems, however at the expense of complex control hardware and high energy consumption for large systems. On the other hand, semi-active control systems provide adaptability nearly similar to that of the fully active system by real-time tuning of the system's mechanical properties (ex. damping and stiffness).

Semi-active control systems may not have the same control authority of fully active control systems, however they have less complex control hardware and provide fail-safe features during control malfunctions [27]. Moreover, smart semi-active systems can be controlled by electric or magnetic fields, which consume less energy compared to fully active systems.

The dynamics of passive, active, and semi-active systems differ because of how the input control is applied. For the passive single-degree-of-freedom system under base excitation, as shown in Figure 1-6(a), there is no control input; thus, the governing dynamic equation of motion can be derived as:

$$m_{payload}\ddot{x} + c(\dot{x} - \dot{y}) + k(x - y) = 0 \tag{1-28}$$

For an active system with the control input, $u(t)$, applied to the payload through actuators, as shown in Figure 1-6(b), the governing equation of motion can be represented as:

$$m_{payload}\ddot{x} + c(\dot{x} - \dot{y}) + k(x - y) = u(t) \tag{1-29}$$

In semi-active control systems, mechanical properties of the system are altered using variable spring and/or damping elements, as shown in Figure 1-6(c). The stiffness and damping properties are altered by the input, $u(t)$, which can be the magnetic flux density or current in the case of smart MREs. Thus, the governing dynamic equation can be written in the following form:

$$m_{payload}\ddot{x} + c[u(t)](\dot{x} - \dot{y}) + k[u(t)](x - y) = 0 \tag{1-30}$$
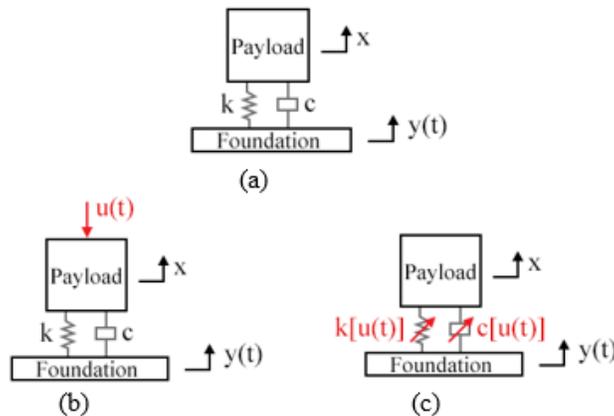
Figure 1-6: System Modelling of a Passive (a), Active (b), and Semi-Active Systems (c) with Base Excitation

In active and semi-active systems, different control strategies can be used to control the output response. Different control laws exist to design the controller. One type of classification for

controller design is of the online and offline types. Online control refers to the controller output being computed during operation, whereas offline control computes the controller output outside of operation. Online control is preferred as the controller can perform corrections for unpredicted disturbances in real time; however, it can be computationally heavy and may not be feasible [28]. On the other hand, offline control methods perform these heavy computations outside of operation but requires prior knowledge of the loading case and disturbance to provide adequate control. In other words, offline control can only be designed for deterministic and predictable loads.

The online control type is the more commonly used between the two and is used in both classical and modern control systems. Online control is achieved through feedback, which uses a comparison between the payload's state and a reference state. Classical control methods generally use transfer function analysis methods in designing a controller. As shown in Figure 1-7, the transfer function block diagram using feedback control defines an error signal, $e(t)$, which is the difference between a reference signal, $r(t)$, and the payload's output signal, $y(t)$. This error signal is then sent to a controller, which then controls the input to force the system to reach the desired target value. The proportional-integral-derivative (PID) control is a widely used classical controller, where the tuning parameters K_P, K_I, and K_D are adjusted such that the system's output meets some performance criteria [24]. The control law applied for PID is of the general form:

$$u(t) = K_P + \frac{K_I}{s} + K_D s \qquad (1\text{-}31)$$

A major disadvantage to PID control is that the tuning parameters must be determined by trial-and-error.
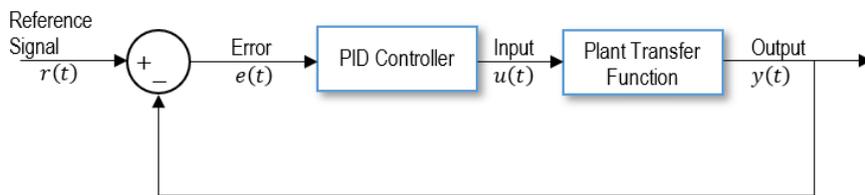
Figure 1-7: Transfer Function Representation with PID Control

State-feedback control provides a better control law that can be determined analytically when compared to its classical PID counterpart. State-feedback controller design requires that the system be modelled using the state-space approach, as seen in Figure 1-8, where the control law is defined as:

$$u = r(t) - Kx \tag{1-32}$$

The state-feedback control uses pole placement to determine a control vector K such that the characteristic equation of the controlled system matches that of the desired performance [23].
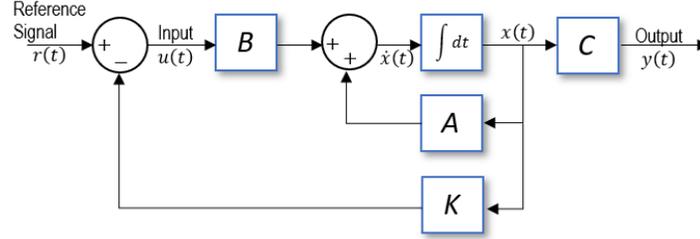
Figure 1-8: State-Space Representation with State-Feedback Control

Alternatively, K can be determined using optimal control theory. An online type of optimal controller is the linear quadratic regulator (LQR), where the dynamics of the system is transformed into an optimization problem [29]. The LQR controller considers the feedback loop and solves the Riccati equation to determine the K vector [29]. The LQR controller depends on weights placed on the system's state energy and input energy and determines an optimal vector for K [29]. Another type of optimal controller optimizes the settling time, and is called the bang-bang, or on-off, control. The on-off controller behaves as a switch, switching between an off and on state depending on some logic derived through the optimization process. The offline optimal control version requires solving Pontryagin's minimum principle, which can be used to solve more complex cost functions [29]. Alternatively, other optimization techniques, such as nonlinear programming (NLP), can be performed to find an optimal control law.

Semi-active systems use a unique type of control algorithm called variable structure control (VSC), which includes skyhook [30], groundhook [31], balance [32], and other variant logics [27]. These types of controls have been mainly used in the automotive industry for semi-active suspension systems. VSC requires a logic in order to activate the variable mechanical properties of the system. The balance logic is designed to reduce chassis acceleration by applying the logic given in Eqn. (1-33), where the damping force is dependent on the relative displacement, x, and relative velocity, $\dot{x}$, across the suspension [27].

$$F_d = \begin{cases} k_s |x| \operatorname{sgn} \dot{x} & x\dot{x} \leq 0 \\ 0 & x\dot{x} > 0 \end{cases} \tag{1-33}$$

The skyhook control assumes the damper being hooked to the sky at some fixed point [27]. The damping force, in this case, depends on the absolute velocity of the chassis, $\dot{x}_1$, and the relative velocity, $\dot{x}$, and is formulated as follows [27]:

$$F_d = \begin{cases} c_{sky}\dot{x}_1 & \dot{x}\dot{x}_1 > 0 \\ 0 & \dot{x}\dot{x}_1 \leq 0 \end{cases} \tag{1-34}$$

Lastly, the groundhook control was developed to reduce dynamic tyre force and is mainly used for heavy vehicles in reducing road damage [31]. The groundhook logic is similar to that of skyhook where the damper is hooked to some fixed point on the ground [27]. The logic for groundhook is dependant on the wheel velocity, $\dot{x}$, and the relative velocity, $\dot{x}_2$, and is defined as follows [27]:

$$F_d = \begin{cases} c_{gnd}\dot{x}_2 & -\dot{x}\dot{x}_2 > 0 \\ 0 & -\dot{x}\dot{x}_2 \leq 0 \end{cases} \tag{1-35}$$

As seen in Eqns. (1-33), (1-34) and (1-35), VSC algorithms behave similar to on-off control, where the damping properties switch from an active to inactive state depending on specific conditions for activation. Hence, VSC methods can be considered special case of on-off controllers dedicated to controlling semi-active systems.

1.3   General Characteristics of Magnetorheological Materials

Smart materials have been used in semi-active control systems because of their capability in changing their mechanical properties. Magnetorheological (MR) materials are unique smart materials that are capable of changing their mechanical properties in the presence of an applied magnetic field. This phenomenon is called the MR effect. The MR effect is attributed to the micron-sized ferromagnetic particles dispersed in the carrier substance of MR materials. The type of MR material depends on the carrier substance used, such as magnetorheological fluids (MRFs), magnetorheological elastomers (MREs) and magnetorheological polymer gels (MRPGs). The ferromagnetic particles, under the influence of a magnetic field, can change the damping, and sometimes stiffness, depending on the smart material used. Studies have been conducted on different MR materials showing the dependency of the MR effect on material factors such as particle size, carrier substance, percent volume of magnetic particles as well as loading factors such as amplitude and frequency of excitations.

1.3.1 Magnetorheological Fluids (MRFs)

One widely used MR material is the magnetorheological fluid, which is typically used in semi-active damping devices such as MR dampers. MRFs are composed of ferromagnetic particles dispersed in a carrier fluid with different additives. These ferromagnetic particles become aligned in the presence of a magnetic field, thus increasing the apparent viscosity and yield strength of the MRF [33]. Lemaire [34] performed a study on the effect of the particle size on the overall behavior of the MRF and concluded that the size of the particles has a significant impact on the MR effect. The use of different additives was studied by Zhang [35] to understand their impact on shear stress and settling properties and concluded that the mass fraction of the particles has the largest impact on shear stress.

MRFs are widely used in the development of semi-active dampers and have been extensively studied in the field of semi-active suspension systems [36]–[48]. The application of MRFs in an adaptive clutch system was first proposed by Rabinow [46]. Since then, the use of MRFs have been extended to various applications. Most studies have implemented VSC methods to control the MRF [30], [32], [49]. Segla and Orecny [47] designed a modified balance control scheme, such as an anti-jerk balance control logic, to eliminate acceleration jumps. Poussot-Vassal et al. [45] modified the skyhook controller via optimization to include user "comfort, road holding, and suspension deflection" as objectives by redefining the damping force definition. Alternate to VSC methods, Lee and Choi [50] applied PID control on the MRF damper of a full-car suspension system. Zapateiro et al. [51] implemented a neural network control with back-stepping onto semi-active suspension systems.

Although being widely used in semi-active damping systems, MRFs have several disadvantages. Similar to viscous dampers, MRF-based dampers are also subject to fluid containment issues and leakage, leading to environmental issues. A unique disadvantage attributed to MRFs is sedimentation stability, where the "magnetic particles and carrier liquid would be separated" if left for long periods of time [35].

1.3.2 Magnetorheological Elastomers (MREs)

Magnetorheological elastomers are analogous to magnetorheological fluids except that the ferromagnetic particles are embedded in a nonmagnetic viscoelastic polymeric material. Use of a viscoelastic material rather than a fluid as the matrix carrier empowers MREs to change both their

stiffness and damping simultaneously under the application of an external magnetic field. The viscoelastic properties of MREs change in the presence of a magnetic field due to the alignment of ferromagnetic particles toward the direction of the applied magnetic field [52]. Hence, MREs have the additional capability of changing their stiffness beside damping unlike MRFs, which can only provide variable damping. Furthermore, MREs do not have the leakage and sedimentation issues generally encountered in MRFs. Because of the controllability of the stiffness and damping in MREs, they can effectively used for the development of MRE-based adaptive vibration absorbers and isolators capable of altering their natural frequency.

1.3.2.1 Types of MREs

MREs are smart multifunctional materials with controllable field-dependent mechanical properties such as stiffness and damping. They are composed of ferromagnetic particles embedded in a polymer matrix. Soft magnetic particles, such as carbonyl iron particles (CIPs), are used due to their "high magnetic saturation and high magnetic permeability" [53].

Aside from being dependent on the magnetic field, the mechanical properties of the MRE depend on the fabrication process. MREs are fabricated by mixing CIPs with liquid rubber, which is then cured. If the curing process occurs in the presence of a magnetic field, then the magnetic particles will remain aligned in the cured polymer thus causing the MRE to have anisotropic properties [52]. Isotropic MRE is fabricated by curing without the presence of a magnetic field, causing the arrangement of the particles to be random [52].

The polymer matrix used for MRE allows the smart material to have both elastic and damping properties due to their viscoelastic nature. Silicon and natural rubbers are widely used for the fabrication of MREs [52]. In the frequency domain, the stiffness and damping properties are generally described through a complex shear modulus, where the real component is called the storage modulus, G', and the imaginary component is called the loss modulus, G''.

$$G_{MRE} = G' + jG'' \tag{1-36}$$

Figure 1-9 shows a general stress and strain response behavior of viscoelastic materials subject to an oscillatory input. Phase shift between the stress and strain response generally suggests the damping properties in polymeric materials. For purely elastic material, the strain follows the stress directly without any phase shift [54]. The elastic energy stored in the viscoelastic material is

generally represented by the storage modulus while the energy dissipated is defined by the loss modulus [54].
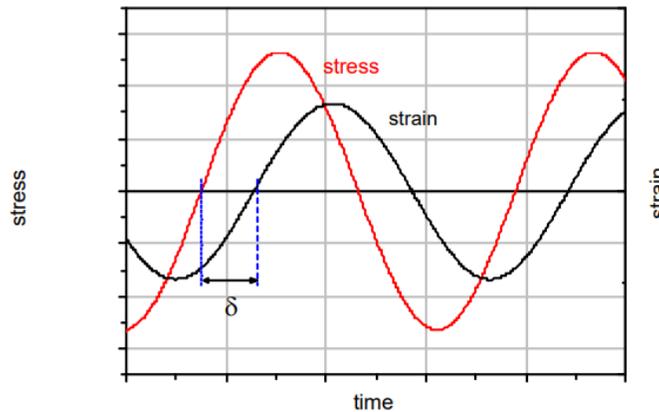
Figure 1-9: Stress and Strain Signals for Viscoelastic Materials with Complex Shear Modulus [54]

1.3.2.2 *Microstructural Behavior due to the Applied Magnetic Field*

The mechanical properties are strongly dependent on the magnetic field and this phenomenon is called the magnetorheological (MR) effect. The magnitude of the MR effect is dependent on the microstructural behavior of the smart material. Figure 1-10 shows the behavior of the ferromagnetic particles when subject to an external magnetic field. Under the influence of an external magnetic field, the ferromagnetic particles organize themselves in the direction of the magnetic field, as shown in Figure 1-10(b). These particles tend to attract one another due to induced dipoles from the magnetic field. Overall, this causes a change in the viscoelastic properties of the polymeric medium in MREs, thus increasing the stiffness and damping as the particles align and form a chain [55].
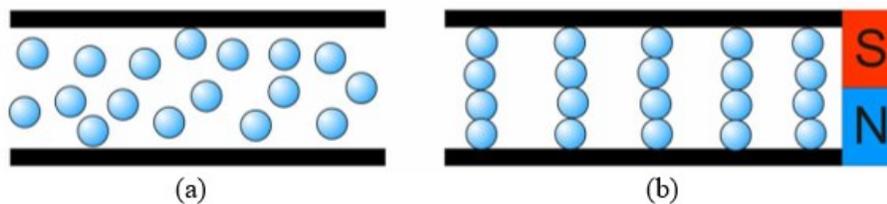
Figure 1-10: Ferromagnetic Particle Arrangement in MR Material Before (a) and After (b) the Application of an External Magnetic Field [55]

In essence, the mechanical properties are largely influenced by the magnetic interactions between the ferromagnetic particles, and between particles and elastomeric medium. Factors that

affect the interaction between particles are the spacing and size of the particles. The MR effect is relatively increased for larger micron-sized particles because the magnetic interaction energy between particles is also increased [56]. Also, increased volume fraction of the ferromagnetic particles in the polymer matrix causes a reduction in spacing between the particles, thus increasing the magnetic interactions.

1.3.2.3 *Dependency on Excitation Frequency*

Mechanical properties of MREs also depend on the applied excitation frequency. Since vibration is a time-dependent problem, then time would be required for the particles to interact and align hence the dependency on the frequency of vibration. As the particles separate due to deformation, they will realign due to the magnetic field. At low input frequencies, the changes in separation are slow thus the realignment is almost instantaneous [55]. However, for high input frequencies, the changes in separation occur rapidly such that the particles do not have sufficient time to realign. The dependency on frequency of vibration is mainly seen as an increase in both storage and loss modulus similar to typical rubbery material [57].

Norouzi et al. [58] conducted an experimental study demonstrating the dependency of the MR effect on frequency and strain amplitude. It was concluded that a rapid increase in the storage and loss moduli occurs as the frequency increases up to 1 Hz, and then slowly increases beyond 1 Hz as shown in Figure 1-11. It is noted that this study was limited to a low range of excitation frequencies.
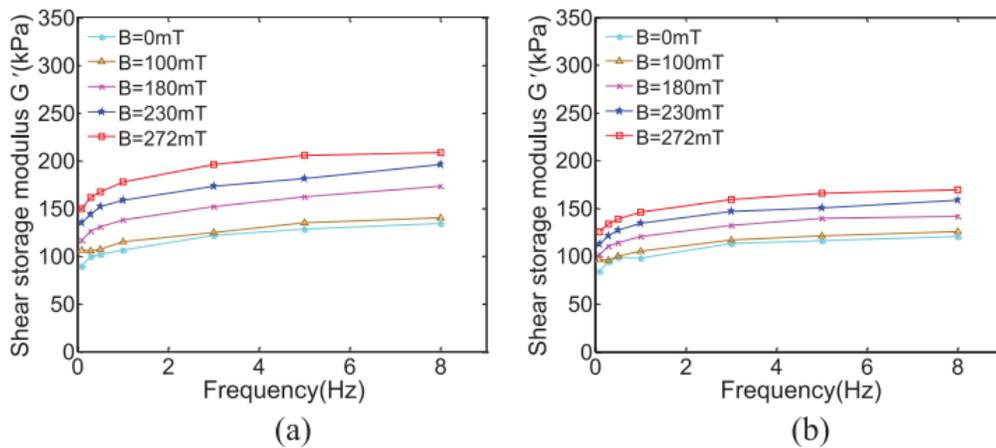
Figure 1-11: Dependency of Storage Modulus on Input Frequency at a Fixed Shear Strain of 4% (a) and 16% (b) [58]

1.3.2.4 Dependency on Strain Amplitude

The dependency of the mechanical behaviors of MRE on amplitude is related to the Payne effect, which is caused by the interaction between the polymer matrix and the ferromagnetic particles [53]. At higher shear strains, the separation between particles increase significantly and tend to disrupt the magnetic interaction [53]. Under small shear strains, the particle network undergoes slight disruption; however, large shear strains cause a disruption such that "the MRE structure becomes softer" [53]. This phenomenon is called strain softening, which ultimately explains the nonlinearity effect of the MRE under dynamic loading, leading to hysteretic damping.

In the research conducted by Norouzi [58], the storage modulus was shown to decrease as the strain amplitude increases, which is attributed to the Payne effect. Figure 1-12 shows the decreasing trend of the MR effect by increasing strain amplitudes at different magnetic flux densities suggesting the MR effect loses its effectivity. Generally similar to filled rubbers, MREs experience linear viscoelastic behavior under strain amplitude lower than 0.1% in which storage modulus is independent of strain amplitude. However, by increasing strain amplitude beyond 0.1% MREs experience nonlinear viscoelastic behavior in which the storage modulus becomes dependent on the strain amplitude.
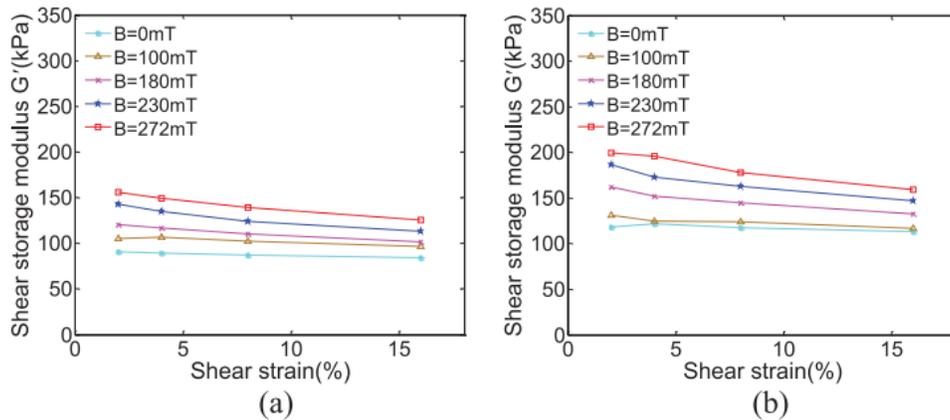
Figure 1-12: Dependency of Storage Modulus on Strain Amplitude at a Fixed Excitation Frequency of 0.1 Hz (a) and 3 Hz (b) [58]

1.3.3 Applications of MRE in Semi-Active Control

1.3.3.1 Semi-Active Suspension Systems

MREs have been effectively used in many semi-active adaptive control systems to control vibration [48]. Application of these semi-active adaptive control systems are generally in the form

of adaptive tunable vibration absorbers (ATVAs) and isolators [2]–[12]. The majority of studies have focused on semi-active suspension systems using VSC methods [27]. Asides from VSC methods, other control methods were explored, such as adaptive neural network (ANN), proportional-integral-derivative (PID), and linear quadratic regular (LQR) control [48].

In the transport industry, MRE-based adaptive control systems have been implemented in different types of suspension systems. Jin et al. [9] developed an MRE-based skyhook control in the suspension system of high-speed trains to attenuate the harsh vibrations attained at high speed. Liu et al. [10] employed ANN control strategy using MRE to develop a semi-active suspension as an alternative to the on-off algorithm due to the limitation of the on-off controller to only two states. Nguyen, Komatsuzaki, and Truong [11] identified that the ANN control may overcome the nonlinearity effects of using MRE. Yu et al. [59] applied ANN control using the ant colony algorithm to tackle the hysteretic behavior of the MRE. Vibration isolation between the vehicle chassis and the engine was explored by Hoang et al. [3] by using an MRE-based adaptive tuned vibration absorber (ATVA) on the powertrain of a vehicle. Qian [12] introduced a fuzzy-based control method to control the mechanical properties of the MRE in the engine-mount suspension system. Choi et al. [6] explored the use of an MRE-based ATVA on the seat suspension of a propeller aircraft. Asides from the transport industry, vibration suppression on a cryogenic cooler was studied by Kim et al. [4] using the MRE-based ATVA.

1.3.3.2 *Semi-Active Control in Structures*

MRE-based control is also implementable in seismic isolation to improve the health of building structures. Most semi-active seismic control have been MRF-based; however, MRE-based control has now been explored because of its additional stiffness controllability. Tariq et al. [60] studied the use of an LQR control in seismic isolation of a multi-degree-of-freedom (MDOF) system and multistory building. Nishimura et al. [61] investigated the use of wave absorption control to reduce vibration in MDOF systems using MRE. Guo [62] proposed a vibration isolation fuzzy fractional-order PID controller to better suppress vibrations compared to the classical PID control. Nguyen et al. [63] explored the use of fuzzy control in order to overcome issues associated with the PID, LQR, and other conventional controllers. Yang et al. [64] studied the use of MRE-tuned mass dampers (TMD) on suppressing vibrations due to wind fluctuations. Jeong [5] demonstrated the effectiveness of MRE-based ATVA on vibration suppression of plates.

1.3.3.3   MRE Sandwich Structures

MREs have been effectively used in the control of flexible structures such as continuous beams. Recent studies consider implementing MRE into the beam structure called MRE sandwich beam, where MRE is placed between two separate aluminum layers. Generally, the material of the outer layer sandwiching the MRE must not interfere with the magnetic field such that the MR effect is not disrupted. Selvaraj and Ramamoorthy [17] studied the effects of using carbon nanotubes (CNT) to reinforce the MRE layer and concluded that the use of CNT increased the storage modulus and loss factor. Ramesh et al. [15] conducted a vibration analysis, using laminated composite beams as the elastic layer. Wei et al. [18] performed a study showing that the MRE sandwich beam is capable of increasing its fundamental frequency and lower its amplitude of vibration in the presence of a homogeneous magnetic field. Furthermore, Hu et al. [19] demonstrated the behavior of the MRE sandwich beam under non-homogeneous magnetic field to activate portions of the MRE layer. The research performed by Hu et al. [19] becomes of interest since the MRE layer in the sandwich structure can be activated in sections compared to full activation of the entire MRE. Long et al. [14] modelled the transverse motion of the beam under non-homogeneous magnetic fields using the fine Mead-Markus model. Poojary [20] addressed the relationship between the change in frequency with changing non-homogeneous magnetic field and concluded that the natural frequency decreases by increasing magnetic field strength and magnetic field placement towards the free end of a cantilever beam. A multidisciplinary design optimization study was conducted by Khanouki [13] to increase the frequency shift of a sandwich beam structure using electromagnets on each end. Szmidt et al. [65] explored the vibration control of a double-beam structure by embedding MRE within the double-beam but at the free end only.

Ni, Ying, and Chen [66] extended the research to different composite structures using MRE as the core, such as composite floor and composite wall, to suppress micro-vibrations. Rasooli [2] applied the semi-active tunable vibration absorber to a five-layered beam with alternating layers of MRE and thin elastic plates. Soleymani [21] studied the aeroelastic stability of a piezo-MRE, which uses piezoelectric face layers, and showed that the use of MRE can help with resolving flutter effects. A study was also conducted by Bornassi [22] in using MRE as the core layer in turbomachine blades in reducing bending and torsional modes of flutter.

While studying the effects of vibration control on MRF sandwich beams, Rajamohan et al. [67] made the conclusion that such systems would require a larger-sized electromagnet due to the size of the overall system. This can be a major drawback to using MR-based sandwich beams since the electromagnet would need to be mounted on the beam in order to activate the MR layer. Mounting an electromagnet to the beam would add additional weight, which will affect the dynamics of the beam. Such a design may not be practical depending on the application. For example, an aircraft wing which is cantilevered to the fuselage cannot have an electromagnet along the wing as this will change the aerodynamic shape. Another possible example would be in electronics packaging where electronic components may be mounted on a beam, where these components are prone to damage under vibrational loads. In some cases, having a magnetic field in proximity to some electronic components can have negative effects such as memory erasure in data storage or magnetic interference on a magnetometer, thus rendering the use of sandwich beam MRE structures undesirable. On the other hand, limiting the weight of the electromagnet consequently limits the magnetic field strength, which ultimately limits the field-dependent viscoelastic properties of the MRE.

1.4   Current Study

In this study, a novel approach has been proposed to control the vibration of continuous, flexible beam structures through boundary conditioning using MRE-based systems at support locations. This proof-of-concept will be demonstrated for a cantilevered beam in which MRE is positioned at the cantilever end. The design requires that the MRE be activated and controlled through a grounded electromagnet using different control laws, such as PID and on-off control. The beam is to be analyzed under different loading conditions to validate the capability of MRE to control flexible structures through the boundary condition.

An advantage of vibration control via boundary condition is that the size of the electromagnet is not constrained by its weight since it is not mounted directly on the flexible beam, similar to previous studies on smart MRE-based sandwich beams. Such a design can be retroactively fitted to existing beams without having to change the beam structure. In the case of electronics packaging, this would be a preferred method of control since sufficient distance can be made between the electromagnet and the electronic components.

26

1.5   Thesis Organization

The main purpose of this dissertation is to discuss vibration control via boundary condition of a cantilever beam using MRE. The relevant literature review, background information, and motivation for this novel control approach have been extensively discussed in this chapter. This chapter also discussed the need for an alternate approach in controlling flexible structures that were not previously explored.

The development of the control strategy first needs an understanding of the MRE and its material model, which is covered in Chapter 2. As discussed previously, the functionality of MRE depends on the magnetic interactions of the ferromagnetic particles under applied magnetic field. A mathematical model for the MRE has been previously developed through experimentation, which will be used in this current research study. Limitations of the mathematical model are discussed, including limits on operating frequency and strain amplitudes.

The next step is to design an electromagnet that is capable of generating a magnetic flux density of high magnitude. The material selection and analytical and numerical magnetic analysis are described in Chapter 3. The overall goal of the electromagnet is to produce the required magnetic flux density to activate MREs and to provide large frequency shifts within the vibrating system. The strength of the magnetic field produced by the electromagnet is estimated using both analytical magnetic circuit and finite element methods in order to determine a functional relationship between the input current to the electromagnet and the induced magnetic flux density in MREs. This relationship is key as it will have a direct impact on the mechanical properties of the overall system through the MRE.

The focal point of this research study lies in chapter 4, where control of the beam through boundary conditioning is formally modelled. Different modelling strategies using MRE at the boundary condition are to be explored to determine the best approach. The Rayleigh-Ritz method has been used to obtain the dynamic behavior and vibration characteristics of the beam with MRE support. The beam geometries are determined by optimization to achieve the goal of having a large frequency shift. The continuous beam with MRE support is then converted to a single-degree-of-freedom (SDOF) system, assuming that the beam is largely influenced by its fundamental frequency. The final SDOF system is then analyzed to understand the impact of using MRE-based boundary condition control.

Chapter 5 describes the development of the control laws. The passive model is to be used as a reference benchmark to demonstrate the effectiveness of the control methods. Firstly, an optimal control law is developed using the nonlinear programming technique in which the optimal control law is to minimize either the settling time, state energy, or input energy. The development of the PID and on-off controller are also discussed. MATLAB Simulink is used to run the simulations and the block diagram models are outlined in this chapter.

Chapter 6 evaluates the performance of different control laws under different loading conditions, such as shock, harmonic, and random vibration loads. A comparative study of the time response to shock loads and harmonic response to harmonic excitation is conducted. For random vibrational loads, statistical methods and spectral analysis are conducted for understanding the behavior of the response under white noise loading.

This dissertation concludes with chapter 7, discussing on the main findings of the present research study. Finally, a number of prospective areas have been pinpointed for future research studies.

Chapter 2: MRE Characterization and Modelling

2.1   Overview

Understanding the mechanical behavior of MREs is of essence for implementation into semi-active control systems. MREs belong to a class of smart materials that can change their mechanical properties under the influence of a magnetic field. Because of the viscoelastic behavior of the polymer used, MREs are capable of changing both stiffness and damping properties, making them desirable for broad-band vibration control applications. Development of material models to predict the field-depended viscoelastic properties of MREs are of paramount importance for the development of an MRE-based system model.

The MRE used in this research study consists of a silicon rubber matrix integrated with 25% volume fraction of carbonyl iron particles. The experimental results describing the variation of storage and loss moduli of the MRE versus excitation frequency and amplitude as well as magnetic flux density are previously conducted and briefly described in Section 2.2 [10].

The main goal of this chapter is to determine a mathematical model relating the storage and loss moduli to the magnetic field strength. In section 2.3, the results from the experiment are discussed in brief to explain the developed mathematical model, which describes the response behavior of MREs in the presence of the magnetic field and the physical limitations of the model. These limitations include the allowable operating frequency range and assumed strain amplitude.

2.2   Experimental Setup for the Characterization of MRE

In order to properly implement MRE into any system, it is necessary to develop the appropriate material models which can accurately predict the mechanical properties with respect to the applied magnetic field. The MRE considered in this analysis has a 25% volume fraction of carbonyl iron particles in a silicon rubber matrix, which has been previously characterized using an advanced magneto-rheometer [10]. The experimental setup, shown in Figure 2-1, consists of a rotary rheometer to characterize the MRE under shear. The MRE is placed between two rotary parallel plates such that the MRE is under torsional shear when an oscillatory torque is applied. A control system is used to apply the magnetic flux density between a range of 0 to 1 T using a feedback system, where a hall probe measures the magnetic flux density and sends the signal back such that the system maintains a constant magnetic flux density [10]. The viscoelastic properties of the MRE

29

including storage and loss moduli were subsequently obtained under varying magnetic flux density, excitation frequency, and shear strain amplitude.
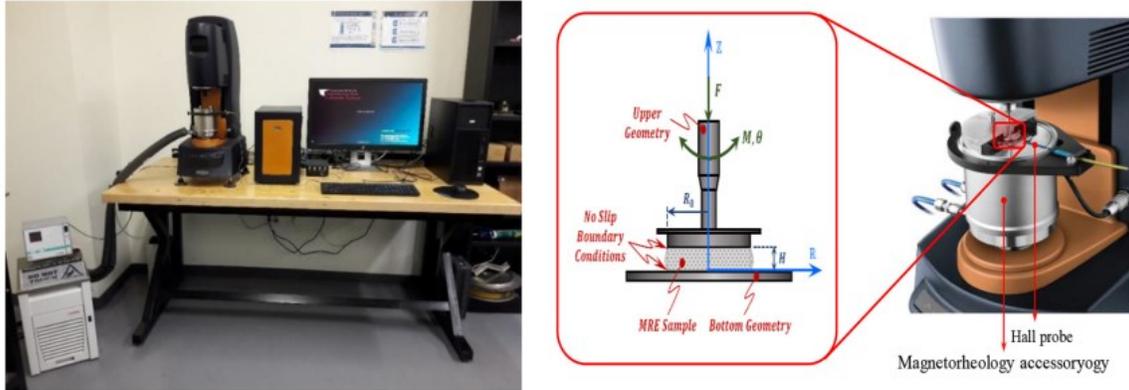
Figure 2-1: MRE Testing System and Schematic Diagram [10]

2.3   Mathematical Model and Limitations of MRE

Results for variation of storage and loss moduli versus frequency (for a given strain amplitude of 15%) and strain amplitude (for a given frequency of 2 Hz) under different magnetic flux densities are shown in Figure 2-2 and Figure 2-3, respectively [10]. Results show that both storage and loss moduli increase slightly with frequency regardless of the applied magnetic flux density. Thus, the dependency of the storage modulus on the excitation frequency is considered negligible for frequencies under 10 Hz. On the other hand, the storage and loss moduli decrease substantially as the strain amplitude increases particularly under high magnetic flux densities. Reduction of storage modulus by increasing strain amplitude is mainly due to the strain softening effect as also observed in filled rubber due to the Payne effect. In this study, it is assumed that MREs operate in linear viscoelastic region for strain amplitudes up to 15%. Thus, in the design of MRE support for the beam, attempt has been made to limit strain amplitude in MRE to under 15%.

The storage and loss moduli were further investigated at a frequency of 2 Hz and a shear strain amplitude of 15% in order to obtain their behavior under varying magnetic flux density [10]. The experimental results were subsequently curve-fitted with a 3rd-order polynomial for the magnetic flux density ranging from 0 to 1 T to derive explicit relations for the storage and loss moduli with respect to magnetic flux density as [10]:

$$G' = -234.3\,B^3 + 396.7\,B^2 + 10.94\,B + 63.04\;kPa$$
$$G'' = -103.2\,B^3 + 151.1\,B^2 + 7.79\,B + 13.27\;kPa$$

(2-1)

Figure 2-4 shows the variation of storage and loss moduli with respect to frequency. Results show that both moduli approach an asymptote at 1 T due to magnetic saturation, where any further increase in magnetic flux density will cause negligible changes in both moduli [10]. Results clearly show that storage modulus increases from nearly 60 kPa to almost 240 kPa by increasing the magnetic flux density from 0 to 1 T. This represents an MR effect (ratio of storage modulus under maximum magnetic flux density to that in the absence of magnetic field) of nearly 4.
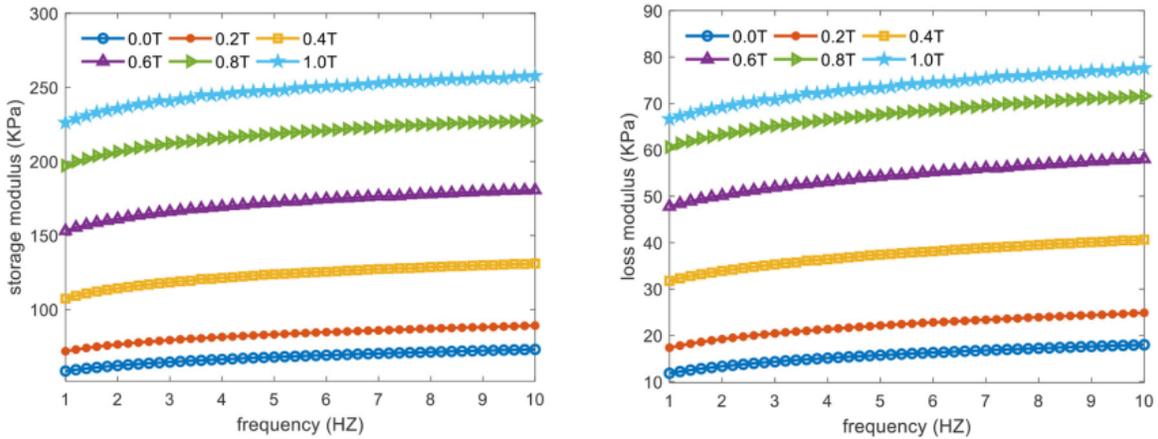
Figure 2-2: Storage and Loss Moduli under Varying Excitation Frequency [10]
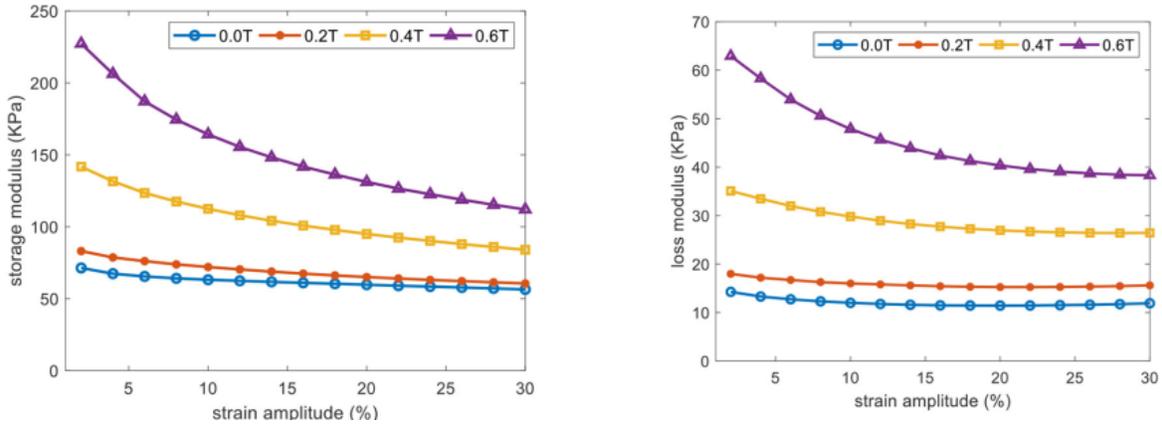
Figure 2-3: Storage and Loss Moduli under Varying Strain Amplitude [10]
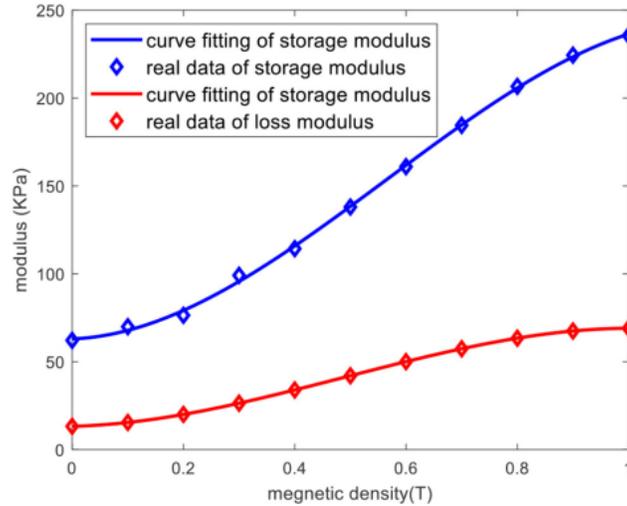
Figure 2-4: Comparison of Experimental Data and Curve Fitting Representation of Storage and Loss Moduli vs. Magnetic Flux Densities at 2 Hz and 15% Shear Strain [10]

2.4 Summary

MRE is a smart material capable of changing its mechanical properties under the influence of an external magnetic field. Viscoelastic properties of MREs are generally dependent on the volume fraction of CIPs embedded within the polymer matrix. The MRE used in this research study is a 25% volume fraction of CIPs in a silicon rubber matrix. Experimental results conducted by the research group show insignificant variation of moduli with respect to frequency up to 10 Hz. Explicit relations have been formulated for storage and loss moduli with respect to the applied magnetic flux density up to 1 T at a frequency of 2 Hz and strain amplitude of 15%. Results clearly show significant increase in storage modulus from nearly 60 kPa at 0 T to almost 240 kPa at 1 T representing an MR effect of nearly 4. The material model in Eqn. (2-1) will be used later to design an adaptive cantilever beam with MRE support.

Chapter 3: Design of Electromagnet to Activate MRE

3.1 Overview

The next step in designing an MRE-based adaptive structure is to design an electromagnet such that the input current to the electromagnet can effectively provide the required magnetic flux density in MRE active regions. A design goal is to select the materials and dimensions of the electromagnet such as to achieve a maximum magnetic flux density in the MRE location. As discussed in section 1.3.3.3, the weight of the electromagnet does not become a design constraint as the electromagnet is not directly mounted on the structure as opposed to those in MRE sandwich structures.

Prior to designing the electromagnet, basic understanding of electromagnetism with regards to electromagnets and the properties of magnetic materials are presented in section 3.2. The magnetic properties, such as the relationship between the magnetic flux density, B, and the magnetic field intensity, H, are to be discussed as they have a direct impact on the magnetic analysis.

Section 3.3 presents the materials used in the design of the electromagnet and their associated properties. The electromagnet layout and associated dimensions are generalized such that the electromagnet design can achieve maximum magnetic flux density at the maximum operating current according to the parameterized dimensions.

An analytical one-dimensional magnetic circuit model of the electromagnet has been initially formulated to evaluate the induced magnetic flux density in the MRE active region for the given applied current. Generally, the magnetic flux density within the electromagnet changes within the volume; however, the analytical magnetic circuit model only considers the instantaneous change in magnetic field intensity across the length of the material. This 1-D method is preferable due to its computational efficiency. The magnetic circuit model and its analytical solution are outlined in section 3.4.

A more accurate approach is to perform the magnetic circuit analysis using the finite element method. An open-source software called Finite Element Magnetics Method (FEMM) is used to conduct a two-dimensional (2-D) magnetostatic finite element analysis of the circuit, demonstrating the variation of magnetic flux density within the volume. The pre- and post-processing setup of the FE model are outlined in section 3.5.

Section 3.6 conducts a comparison between the analytical magnetic circuit and finite element methods. The main result of this chapter is to obtain a function relationship between the input current and magnetic flux density to control the mechanical properties of the MRE.

3.2 Electromagnetism and Properties of Magnetic Materials

In general, the magnetic field is described using Maxwell's equations; however, exact solutions are quite complex and challenging. Simplification of the Maxwell's equation under the assumption that time-varying terms can be neglected leads to Ampere's law and Gauss's law, which are formally stated as [68]:

$$\oint_C H \, dl = \int_S J \, dA \qquad (3\text{-}1)$$

$$\int_S B \, dA = 0 \qquad (3\text{-}2)$$

Ampere's law gives a relationship between the magnetic field intensity, H, and the current density, J [68]. Gauss's law formally states the non-existence of magnetic monopoles, and results in magnetic flux not being able to enter or leave a closed surface [68]. The magnetic flux density is analogous to the current density, in which the magnetic flux density is defined as the magnetic flux, ϕ, per unit area. The magnetic flux density is formally defined as:

$$B = \frac{\phi}{A} \qquad (3\text{-}3)$$

The electromagnet must use materials that will help promote the strength of the magnetic field. The magnetic field is generally characterized by the magnetic flux density and magnetic field strength. The magnetic permeability, μ, is the driving material property that affects the strength of the magnetic field within the material and is described as the material's magnetic conductivity. The magnetic flux density and the magnetic field strength in the region well below saturation limit are linearly related as [69]:

$$B = \mu H \qquad (3\text{-}4)$$

In most magnetic materials, as the magnetic field strength increases toward the saturation limit, the above relationship becomes nonlinear. Usually the *B-H* curve of magnetic materials can be effectively used to analytically formulate the nonlinear relationship between the induced magnetic flux density in the material and the applied magnetic field strength.

Permanent magnets are useful in increasing the magnetic flux density within the overall electromagnet as they are able to store magnetic energy such that there remains a residual magnetic flux density under zero current[69]. This residual magnetic flux density is called the remanence, B_r. In order to bring the magnetic flux density to zero, then the magnetic field intensity must be equal to the coercivity, H_c, as shown in Figure 3-1 [69]. An unmagnetized permanent magnet starts with a *B-H* curve following the initial unmagnetized *B-H* curve as shown in Figure 3-1. Further removal and reapplication of an external magnetic field leads to a hysteretic behavior, which represents the final magnetized *B-H* relationship for permanent magnets. In general, the hysteresis curve can be obtained by shifting the unmagnetized curve by the remanence.
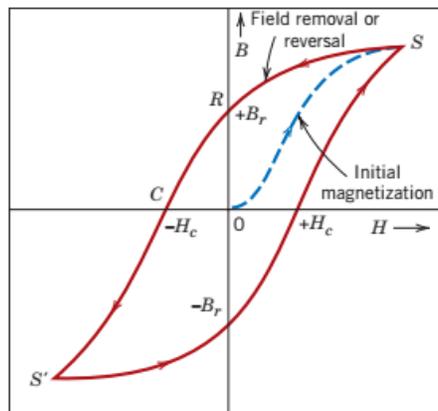
Figure 3-1: General B-H Hysteresis Curve for Permanent Magnets [69]

3.3   Electromagnet Design

In MRE-based devices, the stiffness and damping properties of MREs are controlled by the magnetic flux density generated by either a permanent magnet or an electromagnet. Vibration control using MRE is achieved by using electromagnets in which the input current is effectively used to control the magnetic flux density in the active region where the MREs are located. The electromagnet must be designed to provide sufficient magnetic flux density to alter the complex shear modulus of the MRE and consequently the system dynamics.

In the proposed methodology, MREs are effectively used to alter the beam's natural frequencies through boundary conditioning. Compared to previous designs using sandwich structures with MRE as the core layer and mounted electromagnet, the proposed method integrates the electromagnet at the support location of the beam, as shown in Figure 3-2. Therefore, there is

no size constraint as the electromagnet is integrated externally at the support rather than mounted directly on the flexible beam.
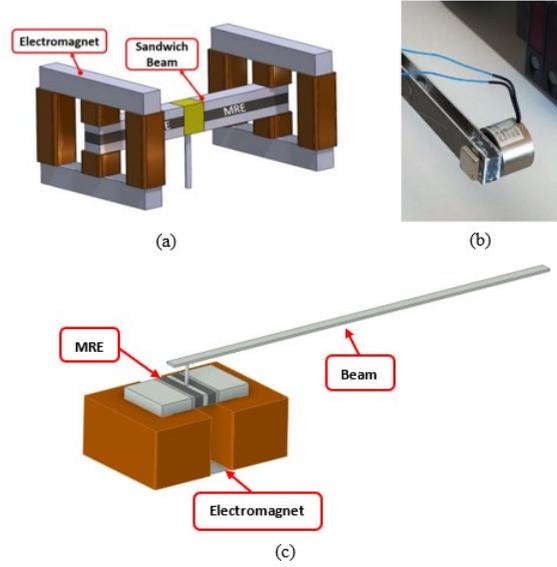
Figure 3-2: Examples of Mounted Electromagnet Design (a) & (b) [13], [65] and Proposed Grounded Electromagnet Design (c).

The proposed electromagnet has a C-shape core made of 1008 steel with a density of 7861 kg/m^3. Low-carbon steels, such as 1008 steel, are preferable for the electromagnet core as they can be easily magnetized and demagnetized. The *B-H* curve for the 1008 steel is shown in Figure 3-3 and is used to obtain the relation between *H* and *B* using a 5th-order polynomial. The polynomial coefficients are identified using the least square minimization technique and are provided in Table 3-1 [70].

$$H_{steel} = R_{s0}B^5 + R_{s1}B^4 + R_{s2}B^3 + R_{s3}B^2 + R_{s4}B + R_{s5} \qquad (3\text{-}5)$$

Table 3-1: Curve-Fitting Coefficients for B-H Relationship of 1008 Steel [70]

Coefficient	B ≤ 1.5 T	B > 1.5 T
R_{s0}	0.00	−1419.52
R_{s1}	1.82	13551.37
R_{s2}	−3.63	−50744.31
R_{s3}	1.782	93520.50
R_{s4}	0.387	−5032.46
R_{s5}	0	30566.42

36
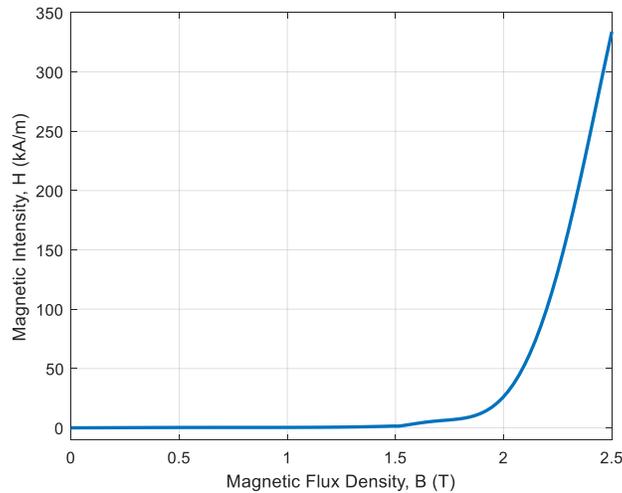
Figure 3-3: B-H Curve for 1008 Steel [70]

The electromagnet core is coiled using 17 AWG wire, which has a diameter of $D = 1.15$ mm. To avoid overheating of the wires, the ampacity of the 17 AWG wire is about 2.9 A to operate within safe limits [71]. For a density of 8886 kg/m^3, the 17 AWG copper wire with diameter of 1.15 mm will have a mass of nearly 9.23 kg for the length of 1 km [72].

Permanent magnets are also included into the electromagnet design to be able to both increase and decrease the stiffness of the MRE with respect to the initial configuration with an input current of 0 A. N52 neodymium permanent magnets, having a density of 7500 kg/m^3 [73], are included in the electromagnet design to help increase the magnetic flux density when the current direction to the electromagnet is positive and decrease when the current is negative. The N52 permanent magnet has a magnetic remanence of 1.464 T and a coercivity of 956 kA/m [74]. Having a high coercivity is a particular property of interest in neodymium magnets, which leads to the N52 magnet being one of the strongest permanent magnets. In general, permanent magnets are defined by their demagnetization curve. The initial magnetization *B-H* curve for the N52 magnet is provided by FEMM; however, the provided curve must be offset by the remanence to obtain the demagnetization curve, which is shown in Figure 3-4.
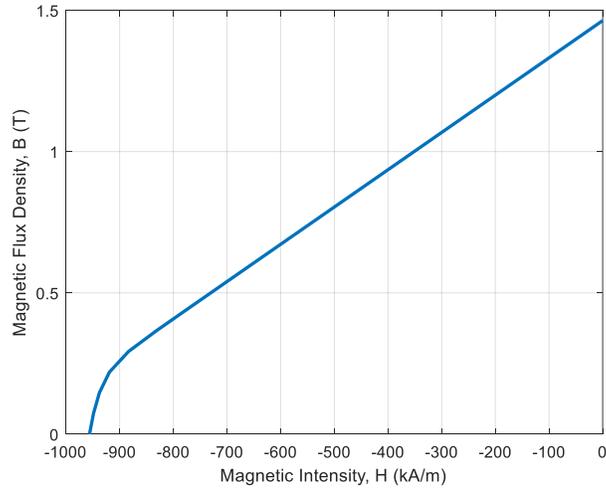
Figure 3-4: Demagnetization Curve for N52 Permanent Magnet

Two pads of MRE, having a density of 3500 kg/m^3 [13], are contained between the two permanent magnets. The MRE pads sandwich a layer of 1008 steel, which will act as the support of the beam. The magnetic properties of MRF are used since the magnetic properties of MRE are not readily available [13]. The MRE considered has a density of approximately 3500 kg/m^3. The *B-H* relationship for the MRF, shown in Figure 3-5, follows a second-order polynomial of the form [13], [75]:

$$H_{MRE} = 289\,B^2 + 34\,B \tag{3-6}$$
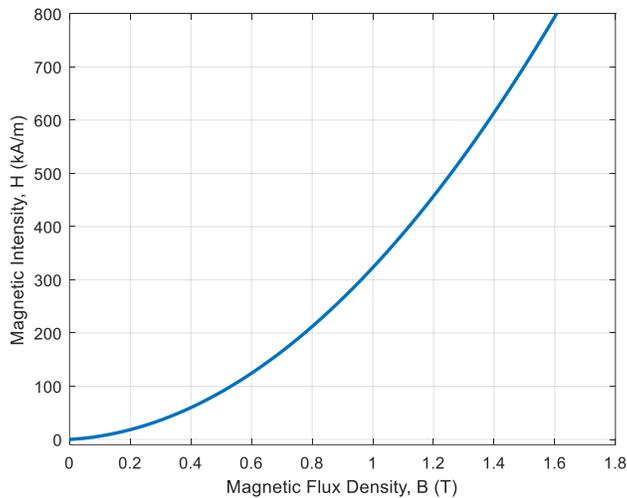
Figure 3-5: B-H Curve for MRF-132DG [13], [75]

Figure 3-6 shows the layout of the proposed electromagnet design including the relevant materials and geometrical dimensions along with a section view of the solenoid. It is noted that extending beyond the permanent magnet will result in the copper windings interfering with the MRE's deflection. The number of windings is approximately determined by dividing the area covered by the wires by the cross-sectional area of the wire and can be obtained as:

$$N_w = \frac{b(c + k)}{D^2} \qquad (3\text{-}7)$$

The total length of the wire is approximated by measuring the perimeter formed by a line centered in the coiled region, which is represented by the red dashed line in section A-A of Figure 3-6. Therefore, the length can be approximated by:

$$L_w = N_w[2w + 2t + 2(c + k)] \qquad (3\text{-}8)$$

The geometrical parameters of the electromagnet shown in Figure 3-6 have been found using the analytical magnetic circuit analysis (discussed in Section 3.4) and trial and error to generate a maximum flux density of nearly 1 T in the MRE active regions at an applied current of 3 A and are provided in Table 3-2. For the identified dimensions, the weight of the electromagnet is found to be approximately 5.5 kg, where the bulk of the weight is from the windings. A summary of the component weights is found in Table 3-3.

Table 3-2: Electromagnet Dimensions

Dimension	Value
Thickness, t	10 mm
1008 Steel Uncoiled Length, c	20 mm
1008 Steel Coiled Length, b	50 mm
Electromagnet Width, w	50 mm
N52 Magnet Thickness, k	3 mm
MRE Thickness, r	8 mm
1008 Steel between MRE, g	5 mm
Wire Diameter, D	1.15 mm
Number of Turns, N_w	870 turns
Wire Length, L_w	144.4 m
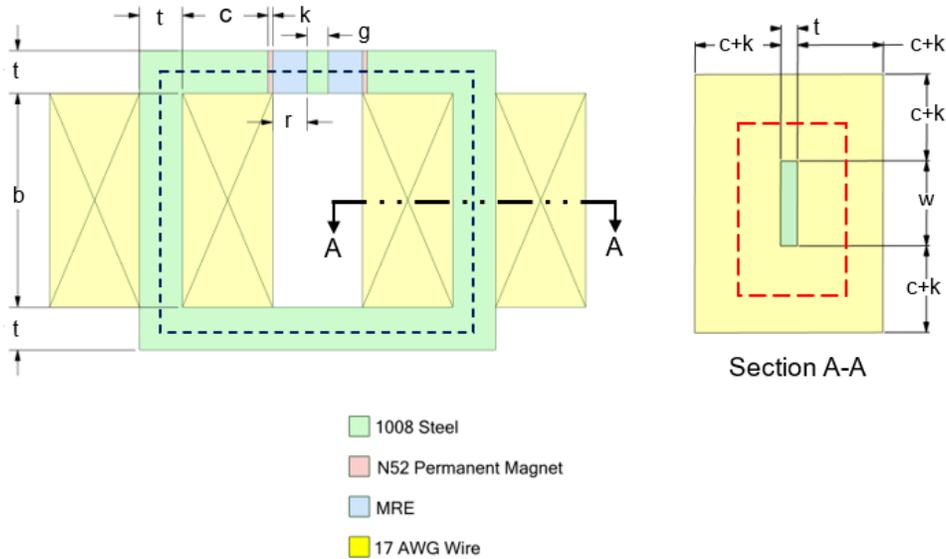
Figure 3-6: Electromagnet Layout with Parametric Dimensions

Table 3-3: Summary of Mass of the Electromagnet Components

Component	Density (kg/m³)	Volume (m³)	Mass (kg)
1008 Steel	7861	1.26E-4	0.990
N52 Permanent Magnet	7500	3.00E-6	0.022
MRE	3500	8.00E-6	0.028
17 AWG Wire	8886	5.83E-4	5.180

3.4   Analytical Magnetic Circuit Model

The analytical magnetic circuit model is a one-dimensional model used to conduct magnetic circuit analysis. The magnetic circuit is basically a magnetic analogue of the electric circuit. This type of analysis simply considers the instantaneous change in magnetic field strength across a component, similar to electric circuits where instantaneous voltage changes across components are only considered. Because the magnetic circuit is an analogue to the electric circuit, methodologies of solving electric circuits can be applied [68]. Hence, analogues of Kirchhoff's laws and Ohm's law are applicable in solving magnetic circuits.

Similar to electric circuits, magnetic circuits are composed of components that either increase or decrease the magnetic field strength. The source of magnetic field intensity, as described in Eqn. (3-1), is from magnetomotive forces (MMFs) developed in current-carrying windings called

solenoids. The magnitude of the MMF, $\mathcal{F}$, is dependent on the input current and the number of windings, and is formulated as:

$$\mathcal{F} = \int_S J \, dA = N_w I \tag{3-9}$$

in which N_w is the total number coil turns in the electromagnet and I is the applied current.

From Eqn. (3-1), the changes in magnetic field strength within the closed loop of the magnetic circuit can be discretized by considering the instantaneous change in magnetic field strength across each ith circuit link representing each material. The changes in magnetic field strength can be formulated as:

$$\oint_C H \, dl = \sum H_i l_i \tag{3-10}$$

For magnetic circuits, Ampere's law is simplified by considering Eqns. (3-9) and (3-10), resulting in the following expression:

$$\mathcal{F} = \sum H_i l_i \tag{3-11}$$

where H_i is the magnetic field intensity for i^{th} circuit links (or elements) and l_i is the effective length of this link. If considering magnetic materials well under their saturation limit, then combining Eqns. (3-3), (3-4), and (3-11) gives:

$$\mathcal{F} = \phi \sum \frac{l_i}{\mu_i A_i} \tag{3-12}$$

Loss in the magnetic field strength is due to the reluctance, $\mathcal{R}$, of different links used in the circuit, which can be calculated as:

$$\mathcal{R}_i = \frac{l_i}{\mu_i A_i} \tag{3-13}$$

where A_i is the effective cross-sectional area at the midpoint of the ith link, and μ_i is the magnetic permeability of the ith link. Using the reluctance, then Eqn. (3-12) becomes:

$$\mathcal{F} = \phi \sum \mathcal{R}_i \tag{3-14}$$

Eqn. (3-14) is the analogue to Ohm's law in magnetic circuits which is often called Hopkinson's law. One caveat to Hopkinson's law is that it is only valid within the linear range of

the magnetic material's *B-H* curve. In this analysis, it is desired to saturate the MRE in order to maximize the stiffness of the MRE due to the MR effect. Therefore, nonlinear behaviour needs to be addressed and thus Hopkinson's law is unapplicable. Alternatively, Eqn. (3-11) can be used to address the nonlinearity by determining the magnetic field strength directly from the individual *B-H* curves.

The magnetic circuit of the proposed electromagnet design uses two sets of copper windings and N52 magnets as MMFs. The MRE, 1008 steel, and N52 magnets introduce reluctance to the circuit. The magnetomotive force drop on each circuit link associated with MRE, permanent magnets and C-shape core are defined as follows:

$$(Hl)_{MRE} = 2H_{MRE}r \tag{3-15}$$

$$(Hl)_{N52} = 2H_{N52}k \tag{3-16}$$

$$(Hl)_{core} = H_{core}(l_{top} + l_{side} + l_{bottom}) \tag{3-17}$$

The analytical magnetic circuit is a one-dimensional analysis in which the length of each section in Eqns. (3-15) to (3-17) are measured at the mean line of the volume, as represented by the black dashed line in Figure 3-6. The lengths of each section of 1008 steel are:

$$l_{top} = 2c + t + g \tag{3-18}$$

$$l_{side} = 2(b + t) \tag{3-19}$$

$$l_{bottom} = 2(c + r + k) + g + t \tag{3-20}$$

Figure 3-7 represents the simplified magnetic circuit representation of the proposed electromagnet with the MMF of each winding and the reluctance of each material. Again, rather than using reluctance, the material's *B-H* curve will be used directly to determine the drop in MMF, Hl.
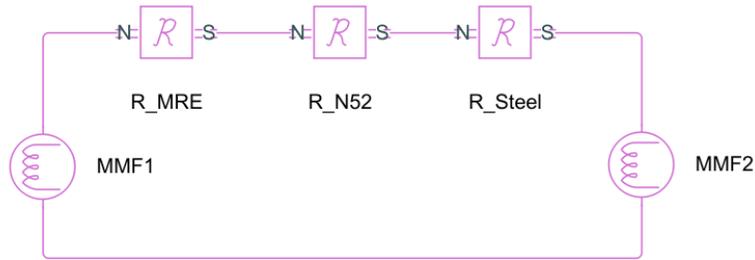
Figure 3-7: Magnetic Circuit Representation of the Proposed Electromagnet

Now considering Eqns. (3-15) to (3-20) and Eqn. (3-11), this gives:

$$N_w I = 2H_{MRE}r + 2H_{N52}k + H_{core}\left(l_{top} + l_{side} + l_{bottom}\right) \qquad (3\text{-}21)$$

It should be noted that the magnetic flux density needs to be determined numerically such that the above equation is satisfied since material magnetic nonlinearity is considered. The analysis is simplified by considering a constant cross-sectional area across each section of the electromagnet, thus leading to a constant magnetic flux density at each section. The root-finding bisection method is used to solve Eqn. (3-21) numerically by determining B that will satisfy Eqn. (3-21). Eqn. (3-21) is to be solved under different input currents to develop a model between the input current and the induced magnetic flux density within the MRE.

3.5   Magneto-Static Analysis using Finite Element Method

Although the one-dimensional magnetic circuit method discussed in the previous section is an efficient approach and simple to implement, it does not account for the variations of the magnetic field inside the volume. In this section the finite element model of the proposed electromagnet is developed in Finite Element Method Magnetics (FEMM), which is an open-source finite element solver, to conduct magnetostatic analysis numerically. FEMM is a two-dimensional solver, which assumes that no variations of magnetic field exist across the depth.

3.5.1   Pre-Processing

FEMM uses the Lua extension language, which enables FEMM to be executed using scripts. Furthermore, MATLAB is capable of using Lua commands, which allows for further pre- and post-processing capabilities due to additional functions available in MATLAB. Use of Lua commands aid in parameterizing the finite element model, especially the dimensions. Having the dimensions parameterized allows to effectively set up new simulations of the same shape, especially when the aim is to determine a geometry that can provide maximum magnetic flux density in the MRE active region under a maximum current of 3 A. The model's geometry is automated with reference to the parameterized geometry as defined in Figure 3-6. Additionally, a boundary is defined around the electromagnet in order to have a finite region for the surrounding air.

The simulation uses the default setup parameters as defined by FEMM shown in Figure 3-8. One significant model setup parameter is the solver precision, which is set to 1E−008. This provides a convergence criterion for the numerical simulation and thus gives good confidence that

the numerical solution is close to the real solution. By default, the solver is of the steady-state type and can assume that the numerical solution is one where the electromagnet has fully saturated under the given input current. The mesh is automatically created using the smart mesh option. For the geometry defined in Table 3-2, the created mesh consists of 10065 nodes and 19768 elements. The mesh surrounding the electromagnet is displayed in Figure 3-9.
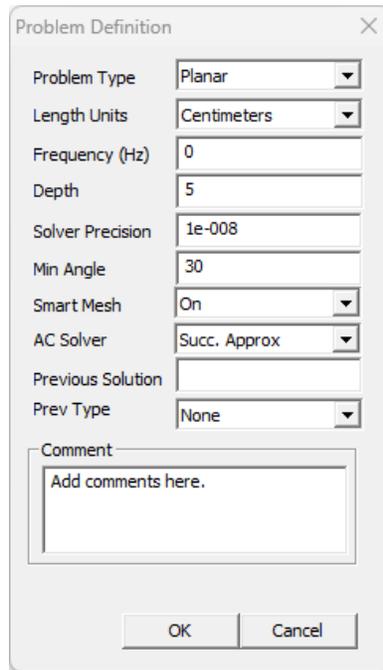
Figure 3-8: Problem Definition for FEMM
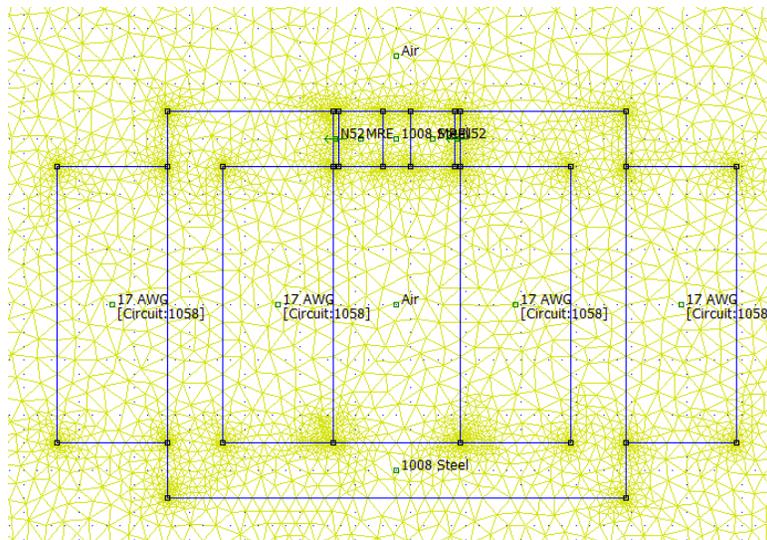
Figure 3-9: Electromagnet FEMM Layout with Surrounding Mesh

The electromagnet properties are defined in three different categories as per FEMM. The first category is the material properties. All material properties are defined as per section 3.3 and are updated in the Lua script. The second category is the boundary properties. There are two types of boundary conditions:

1. Dirichlet condition assumes that the boundary is magnetically conductive, meaning that the magnetic field is zero at infinity [76].
2. Neumann condition assumes that the boundary is magnetically insulated [76].

The Dirichlet condition is applied in this simulation and is manually defined using the "prescribed A" BC-type. The boundary property is defined as shown in Figure 3-10. All boundary settings are default parameters as per FEMM. The last category is for the circuit properties, which requires the circuit current that passes through the windings. The input current is parameterized in the Lua script such that the simulation can be performed for different currents ranging from −3 A to 3 A.
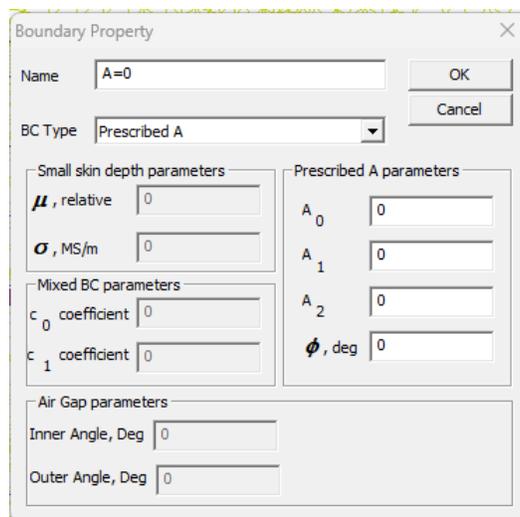
Figure 3-10: Boundary Property Dialog Box and Settings

3.5.2 Post-Processing

Figure 3-11, Figure 3-12, and Figure 3-13 show the distribution of the magnetic flux density at an input current of −3, 0, and 3 A, respectively. Results show that the designed electromagnet is capable of generating magnetic flux density of around 1 T in MRE active region at a maximum current of 3 A. Moreover, examination of the results reveal that that the magnetic flux density distribution in the steel core becomes more uniform as the applied current increases reaching to nearly 1.72 T under a maximum current of 3 A, which is still under its saturation limit. Under zero

current, the generated magnetic flux density is due to only permanent magnets reaching a maximum of about 0.8 T approximately throughout the electromagnet. It is noted that the maximum magnetic flux density at −3 A is approximately 0.8 T which occurs at the bottom of the electromagnet.
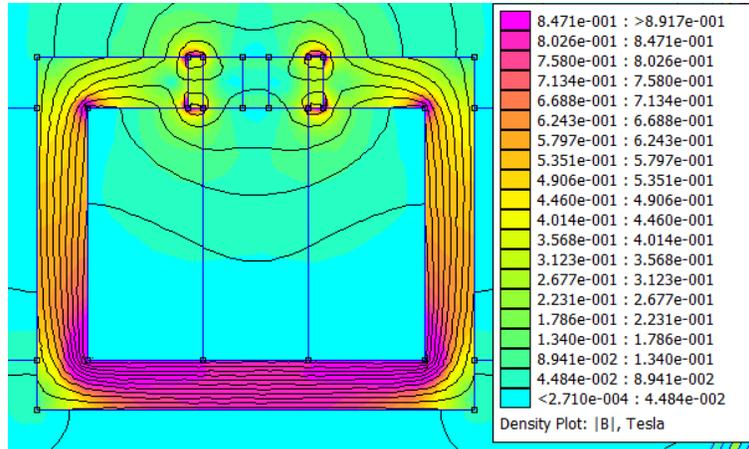
Figure 3-11: FEMM Results for Input Current of −3 A
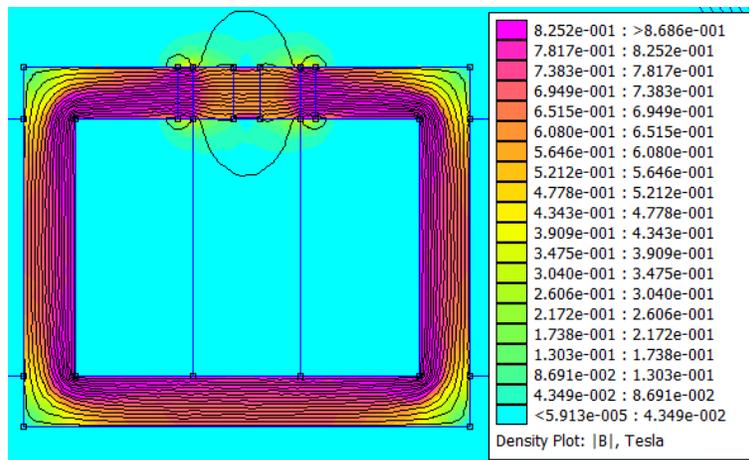
Figure 3-12: FEMM Results for Input Current of 0 A
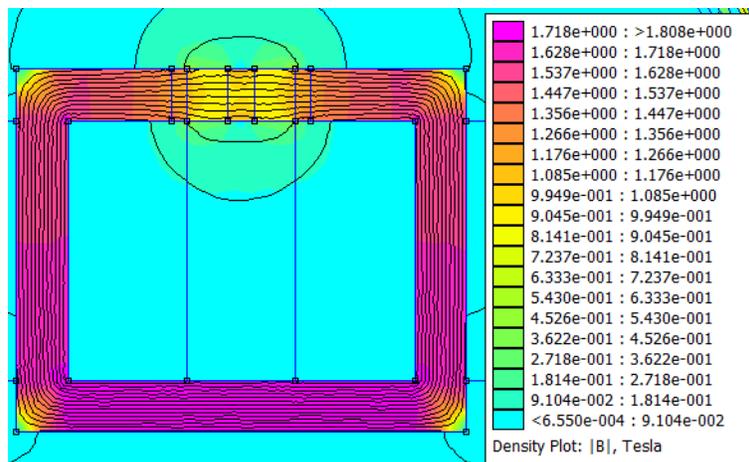
Figure 3-13: FEMM Results for Input Current of 3 A

46

3.6 Comparison of FEMM and Analytical Magnetic Circuit Results

The analytical magnetic circuit analysis can be efficiently used to estimate the magnetic flux density within the MRE region compared with the computationally expensive FE model. However, one should compare the analytical magnetic circuit analysis with the high-fidelity accurate FE model to confirm its accuracy. Here, results obtained from the formulated 1-D magnetic circuit model have been compared in Table 3-4 with those obtained using the 2-D magnetostatic FE model to validate its accuracy. Results from the magnetic circuit model are found to be generally higher than those obtained from the finite element model and differences are substantial at lower applied currents. One possible reason may be that the analytical magnetic circuit model does not take into consideration the effect the permanent magnet has on the electromagnet coils. The proximity of the permanent magnet to the electromagnet coils may cause an electromotive force (EMF) on the current in the solenoid, which may account for the lower magnetic flux densities in the FEMM results. Furthermore, the orientation of the magnetic field due to the permanent magnet is 90 degrees to that produced by the solenoids, which may also have adverse effects on the overall magnetic field. Therefore, results from finite element are preferred over those from magnetic circuit analysis.

Table 3-4: Summary of Magnetic Flux Density using FEMM and Analytical Magnetic Circuit Model

Input Current (A)	FEMM	Analytical Model	Percent Error
−3	0.012	0.201	1575.00
−2	0.300	0.437	45.67
−1	0.501	0.611	21.96
0	0.665	0.762	14.59
1	0.806	0.899	11.54
2	0.913	1.022	11.94
3	0.983	1.136	15.56

A functional relationship between the input current and the magnetic flux density is required for controlling the mechanical properties of the MRE. The relationship is to be obtained using the results from FEMM due to its numerical accuracy. The functional relationship is determined through least-squares optimization where the curve fitting function takes on the form of a polynomial. The selection of the order of the polynomial depends on the desired root-mean-square

error (RMSE). Figure 3-14 shows the relationship between the RMSE and the order of the polynomials. Results show that the 4th-order polynomial provides a very good fit with RMSE below 0.1. The resulting 4th-order curve-fitting polynomial takes the following form:

$$B(I) = -0.00079\ I^4 + 0.0015\ I^3 - 0.012\ I^2 + 0.15\ I + 0.67 \tag{3-22}$$

Comparison of the predictive polynomial relation in Eqn. (3-22) with FEMM results is shown in Figure 3-15.
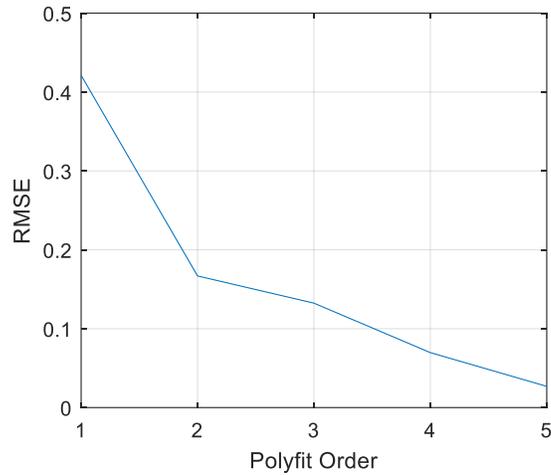
Figure 3-14: RMSE vs Polynomial Order for Curve Fitting of Magnetic Flux Density vs. Input Current for the Designed Electromagnet
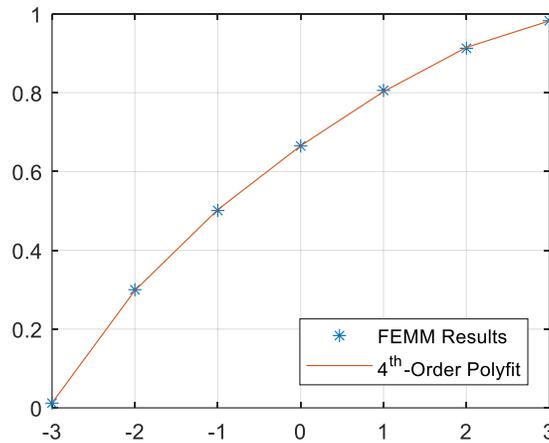
Figure 3-15: Comparison of the FEMM Results with the Curve Fitted 4th-Order Polynomial of the Magnetic Flux Density vs. Input Current Curve

3.7 Summary

In this study an electromagnetic system is designed to provide the required magnetic flux density in the MRE region. Under the designed geometry and material selection, the magnetic flux density can reach to nearly 1 T in the MRE region for an input current of 3 A. Furthermore, the designed electromagnet is capable of going from 0 to 1 T for the full range of current from −3 to 3 A. This gives the MRE full access to its range in both storage and loss modulus, thus ensuring that the overall system can experience a large frequency shift.

The electromagnet was designed using both the magnetic circuit and finite element methods. Because of accuracy issues native to 1-D methods, the FEMM results are preferred for curve-fitting. The analytical magnetic circuit model could not capture the effects the permanent magnet may have on the electromagnet coils, which may likely account for the large discrepancies between the FEMM and magnetic circuit results. Finally, a polynomial model has been developed to predict the variation of the generated magnetic flux density in MRE region versus applied current ranging from −3 A to +3 A input current. The model agrees very well with results obtained using FEMM and can be effectively used to efficiently evaluate the generated magnetic flux density in MRE at any applied current and thus evaluate field dependent storage moduli of MREs.

Chapter 4: Mathematical Modelling of the Beam with MRE Support

4.1 Overview

Now that the electromagnet has been designed, the next step is to determine a model where the electromagnet and MRE can be implemented into the boundary condition. The goal is to design an adaptive beam such that there is a significant shift in the fundamental frequency over the range of input currents, while respecting the limitations of the MRE regarding maximum shear strain amplitude and maximum operating frequency.

In section 4.2, alternative models to the cantilever beam are explored by considering static and dynamic similarity. Static similarity is verified by comparing the geometric and natural boundary conditions between the proposed beam and cantilever beam. Geometric boundary conditions are those with respect to physical constraints, such as conditions on displacement and slope. Natural boundary conditions consider the loads that result from the constraints, such as a fixed support inducing both shear and moment. Dynamic similarity considers that the systems vibrate in a similar manner and is validated by comparing the fundamental frequencies of the proposed beam and the cantilever beam.

Generally, analysis of continuous beams under transverse motion requires solving a partial differential equation by separation of variables. This method is only applicable for beams with common types of boundary conditions. Since the proposed designs are not of a common type like the cantilever and simply-supported beams, then analytical methods for continuous systems to determine the fundamental frequency cannot be performed. In Section 4.3, both analytical and approximate methods are outlined. The Rayleigh-Ritz method, which is an approximate method, has been formulated to evaluate the fundamental frequency and associated mode shape of these alternative models. The Rayleigh-Ritz method is used to gain a better understanding of the dynamic similarity between the proposed models and the cantilever case.

The geometry of the proposed adaptive beam is to be determined using design optimization technique considering the MRE limitations outlined in section 2.3. The optimization problem is defined in detail in section 4.4. As the natural frequency is dependent on the beam geometry, then it is necessary to select the geometry such that dynamic similarity is achieved as much as possible at 1 T and can provide a sufficient frequency shift.

In preparation for the control analysis, the continuous beam has been modeled as an equivalent single-degree-of-freedom (SDOF) model, where the methodology is outlined in section 4.5. The equivalent SDOF model is derived by conducting an energy comparison between the continuous and proposed SDOF models. The SDOF model facilitates the implementation of different control laws to be discussed in Chapter 5.

Finally, section 4.6 discusses the behavior of the developed SDOF system. The time response and harmonic response of the proposed SDOF system is analyzed under different input magnetic flux densities. Understanding the response of the SDOF system will help in controller design.

4.2 Approximate Cantilever Beam Model

In this study, control via boundary conditioning using MRE technology will be investigated on a cantilever continuous beam. Control at the boundary condition is only possible if the rigidity of the support is variable, which is possible by implementation of an MRE-based system. Beams can be considered statically similar if they have the same geometric and natural boundary conditions. The geometric boundary conditions of a cantilever beam must have zero deflection and zero slope at the supported end. The natural boundary conditions are such that the shear and bending moments are non-zero at the fixed end. Two different modelling approaches are considered, which are able to provide both static and dynamic similarity to some extent.

The first approach replaces the fixed end with a pin support and a torsional spring as shown in Figure 4-1(a). The equivalent beam will satisfy the zero-deflection condition by using a pin support. The zero-slope condition can be satisfied using a torsional spring with a high stiffness, which will allow both geometric and natural boundary conditions to be satisfied.

The second approach is to use an intermediate linear spring support at $x = x_s$. This is otherwise known as an overhanging beam, as shown in Figure 4-1(b), if the linear spring was infinitely rigid. As it can be realized from Figure 4-2, the shear and bending moment diagrams of the overhanging beam past the intermediate support are similar to that of a cantilever beam. Therefore, the overhang section of the beam can be considered cantilevered. This approach satisfies the natural boundary conditions starting from the overhang section; however, it does not fully satisfy the geometric boundary conditions. If the intermediate support has infinite stiffness, then there would be zero deflection at the overhang support, but the slope would be non-zero at the same location. Although

this is true, similitude in boundary conditions is not totally enforced since the boundary itself is now subject to control.
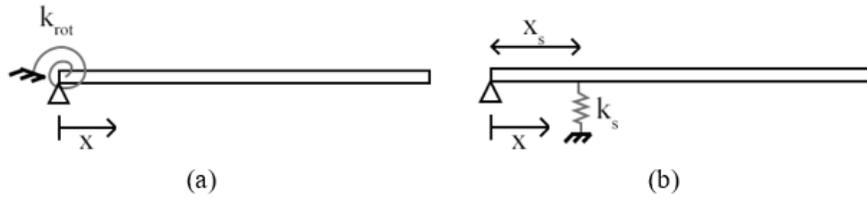
Figure 4-1: Alternative Beams using Torsional Spring (a) and Intermediate Overhang Support (b)
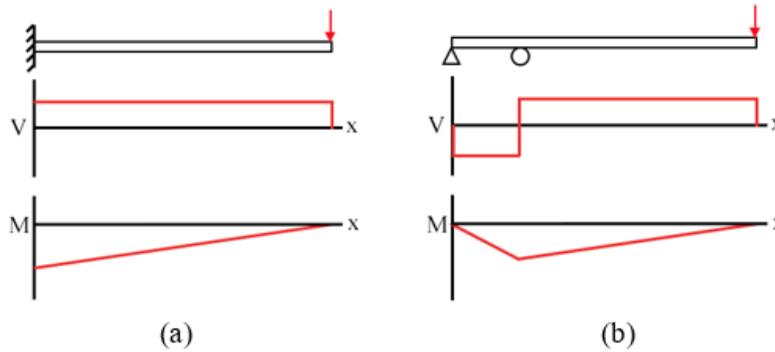
Figure 4-2: Shear and Bending Moment of Cantilever (a) and Overhanging Beam (b)

4.3 Modelling the Continuous Beam using Rayleigh-Ritz

4.3.1 Exact Solution for the Natural Frequency of a Cantilever Beam

The dynamics of the continuous beam is understood by considering the general free vibration equation of motion for the transverse deflection of a beam defined by [77]:

$$\frac{\partial^2}{\partial x^2}\left(EI\frac{\partial^2 w}{\partial x^2}\right) + \rho A\frac{\partial^2 w}{\partial t^2} = 0 \tag{4-1}$$

where $w(x,t)$ is the time-dependent displacement function of the beam. The above partial differential equation can be solved for different boundary conditions applied at the endpoints of the beam. For a cantilever beam, the boundary conditions are [77]:

$$w(0,t) = 0$$

$$\frac{\partial w}{\partial x}(0,t) = 0 \tag{4-2}$$

52

Solution requires separation of variables by defining $w(x,t) = X(x)T(t)$ and substituting into to Eqn. (4-1), giving the following set of ordinary differential equations [77]:

$$\frac{d^4X(x)}{dx^4} - \beta^4X(x) = 0 \tag{4-3}$$

$$\frac{d^2T(t)}{dt^2} + \omega^2T(t) = 0 \tag{4-4}$$

From the above equations, the generalized natural frequencies of the continuous beams under different boundary conditions are defined by [25]:

$$\omega_i = (\beta_i l)^2 \sqrt{\frac{EI}{\rho A l^4}} \tag{4-5}$$

where $\beta_i l$ is the ith non-dimensional natural frequency of the beam and depends on the boundary conditions. For the cantilever beam, the first non-dimensional natural frequency is 1.875104 [25]. Only the first fundamental frequency is considered as it is assumed that the response of the system is mainly dominated by the first vibration mode.

4.3.2 General Formulation of the Rayleigh-Ritz Method

The analytical solution to Eqn. (4-1) as described above is not possible for the alternate models because of the flexible support. Alternatively, the Rayleigh-Ritz method, which is an approximate method, can be effectively used to evaluate the natural frequencies of continuous systems, especially the first few lower modes [77]. The Rayleigh-Ritz method assumes a mode shape, $X(x)$, which is a linear combination of admissible basis functions, $\phi_i(x)$. The mode shape must satisfy the geometric boundary conditions and can be generalized as:

$$X(x) = \sum_{i=1}^{n} c_i \phi_i(x) \tag{4-6}$$

where c_i are the coefficients associated to each admissible basis function. The natural frequencies of the continuous system are determined by the Rayleigh's quotient, which is dependent on the maximum strain energy, π_{max}, and kinetic energy, T_{max}^*. Rayleigh's quotient also happens to be related to the harmonic frequency of the system, and is formulated as [77]:

$$R = \frac{\pi_{max}}{T^*_{max}} = \omega^2 \tag{4-7}$$

The unknown coefficients, c_i, of the mode shape function are determined such that the Rayleigh's quotient is minimized. The minimization is applied to Rayleigh's quotient for each coefficient, and is stated as follows:

$$\frac{\partial R}{\partial c_i} = 0 \tag{4-8}$$

The accuracy of the Rayleigh-Ritz method in determining the natural frequencies depends on the number of admissible functions used. The estimated frequency will always overestimate the actual frequency but as the number of admissible functions increases, the estimated frequency will approach the exact solution [77].

There are many possibilities when determining a set of admissible functions. Firstly, they must estimate the mode shapes of the system. Secondly, they must satisfy the geometric boundary conditions. The simplest solution is to use a set of polynomials; however, the coefficients of the polynomials need to be determined. Two conditions can be applied to determine the coefficients. The first condition is that the polynomials be orthogonal, which causes the polynomials to be linearly independent to one another [78]. Two functions (f_1 and f_2) are said to be orthogonal if their inner product is zero, meaning that [79]:

$$\langle f_1, f_2 \rangle = \int_a^b f_1(x)f_2(x)\,dx = 0 \tag{4-9}$$

For a set of orthogonal polynomials, p_i, then [79]:

$$\langle p_m, p_n \rangle = \int_a^b p_m(x)p_n(x)\,dx = 0, m \neq n \tag{4-10}$$

The second condition is that the polynomials be normalized, meaning that the inner product of two polynomials have unit length [78]. For any two functions (f_1 and f_2), normalization is such that:

$$\langle f_1, f_2 \rangle = \int_a^b f_1(x)f_2(x)\,dx = 1 \tag{4-11}$$

These conditions lead to orthonormal polynomials, ϕ_i, which can formally be defined by [78]:

$$\langle \phi_m, \phi_n \rangle = \int_a^b \phi_m(x)\phi_n(x)\,dx = \delta_{mn} \tag{4-12}$$

where δ_{mn} is the Kronecker delta function, which is generally represented as:

$$\delta_{ij} = \begin{cases} 0 & i \neq j \\ 1 & i = j \end{cases} \tag{4-13}$$

The set of orthonormal polynomials are generated by using the Gram-Schmidt recursive relation [78], [79]. First consider that the variable in question is a non-dimensional distance along the beam length defined as:

$$\xi = \frac{x}{L} \tag{4-14}$$

Using this non-dimensional length, then the bounds of integration for Eqn. (4-12) is from 0 to 1. The recursion process is first generally initialized by stating the first n^{th}-order polynomial form of the set as:

$$p_0 = \xi^n \tag{4-15}$$

The recursion then produces the remaining polynomials in the set by [79]:

$$p_i = \xi^{n+i} - \sum_{j=0}^{i-1} \frac{\langle \xi^{n+i}, p_j \rangle}{\langle p_j, p_j \rangle} p_j \tag{4-16}$$

The orthogonal set can be transformed into an orthonormal set by dividing each function by its norm, that is [79]:

$$\phi_i = \frac{p_i}{\sqrt{\langle p_i, p_i \rangle}} \tag{4-17}$$

Once the beam's mode shape function is defined by the admissible functions, it can then be used to derive the associated beam energies. The potential energy must include both the stiffness of the beam and the stiffness of the spring support. The beam potential energy is defined by its flexural strength and the potential energy due to the additional spring, which depends on the type of spring considered. The kinetic and potential energies are defined as follows with specifics regarding the formulation of the potential energy of the different springs used.

$$T^*_{max} = \frac{1}{2}\int_0^L \rho A X^2 \, dx \tag{4-18}$$

$$\pi_{max} = \pi_{beam} + \pi_{spring} \tag{4-19}$$

$$\pi_{beam} = \frac{1}{2}\int_0^L EI\left[\frac{dX}{dx}\right]^2 dx \tag{4-20}$$

$$\pi_{spring} = \begin{cases} \dfrac{1}{2}k_r\left[\dfrac{dX(0)}{dx}\right]^2 & for\ torsional\ spring\ at\ x = 0 \\[3mm] \dfrac{1}{2}k_s[X(x_s)]^2 & for\ intermediate\ spring\ at\ x = x_s \end{cases} \tag{4-21}$$

The energy equations can then be written in terms of the admissible functions by substituting Eqn. (4-6) into Eqns. (4-18) to (4-21), which leads to the following sets of matrix formulations [77]:

$$T^*_{max} = \frac{1}{2}\vec{c}^T[m]\vec{c} \tag{4-22}$$

$$\pi_{beam} = \frac{1}{2}\vec{c}^T[k]\vec{c} \tag{4-23}$$

where the elements in the mass, $[m]$, and stiffness, $[k]$, matrices are defined as follows:

$$m_{ij} = \int_0^L \rho A \phi_i \phi_j \, dx \tag{4-24}$$

$$k_{ij} = \int_0^L EI \frac{d^2\phi_i}{dx^2}\frac{d^2\phi_j}{dx^2} dx$$
$$+ \begin{cases} k_r \dfrac{d\phi_i(0)}{dx}\dfrac{d\phi_j(0)}{dx} & for\ torsional\ spring\ at\ x = 0 \\[2mm] k_s\phi_i(x_s)\phi_j(x_s) & for\ intermediate\ spring\ at\ x = x_s \end{cases} \tag{4-25}$$

Finally, the fundamental frequencies are determined by inserting Eqns. (4-22) to (4-25) into Eqn. (4-7), which leads to an eigenvalue problem that can be stated as follows:

$$[k] = \omega^2[m] \tag{4-26}$$

Solution to the above eigenvalue problem results in the natural frequencies and mode shapes, or eigenvalues and eigenvectors. The number of natural frequencies and mode shapes determined is

equal to the number of admissible functions considered. Theoretically, a continuous system has infinite numbers of modes and technically the number of admissible functions can also be infinite. In practice, however, the response of the system is mainly dominated by the first few modes especially the fundamental mode.

Considering that the mode shape can be arbitrary, then it would be useful to normalize the mode shape. It turns out that the coefficients in Eqn. (4-6) are the coefficients of the associated mode shape. Let us consider the normalized eigenvector, $\tilde{C}$, obtained from the general eigenvector, C, through some normalization factor n_c:

$$\tilde{C} = n_c C \tag{4-27}$$

where the general eigenvector and normalized eigenvector are of the form:

$$C = \begin{Bmatrix} c_1 \\ c_2 \\ \vdots \\ c_n \end{Bmatrix}, \tilde{C} = \begin{Bmatrix} \tilde{c}_1 \\ \tilde{c}_2 \\ \vdots \\ \tilde{c}_n \end{Bmatrix} \tag{4-28}$$

The eigenvector is normalized such that the associated mode shape in Eqn. (4-6) satisfies $X(x = L) = 1$. The normalization factor is determined by inserting the coefficients of Eqn. (4-27) into Eqn. (4-6) with respect to the previously mentioned condition, resulting in:

$$X(x = L) = 1 = \sum_{i=1}^{n} \tilde{c}_i \phi_i(x = L) = n_c \sum_{i=1}^{n} c_i \phi_i(x = L) \tag{4-29}$$

Solving the above equation gives the normalization factor to be:

$$n_c = \frac{1}{\sum_{i=1}^{n} c_i \phi_i(x = L)} \tag{4-30}$$

4.3.3 Validation of Rayleigh-Ritz using the Cantilever Beam

The Rayleigh-Ritz method is tested for the cantilever beam to validate the method and to verify convergence. For the cantilever beam, the resulting mode shapes should satisfy both geometric constraints. Under these conditions, the non-normalized admissible function used in initializing the Gram-Schmidt recursive function should be of the form $p_1 = \xi^2$. The first five orthonormal admissible functions generated by the Gram-Schmidt recursive algorithm is shown in Table 4-1.

Table 4-1: *Admissible Functions for the Rayleigh-Ritz Method for the Cantilever Model*

i	Admissible Functions, ϕ_i
1	$2.24\xi^2$
2	$15.88\xi^3 - 13.23\xi^2$
3	$84\xi^4 - 126\xi^3 + 45\xi^2$
4	$397.99\xi^5 - 835.79\xi^4 + 557.19\xi^3 - 116.08\xi^2$
5	$1784.7\xi^6 - 4759.3\xi^5 + 4543\xi^4 - 1817.2\xi^3 + 252.39\xi^2$

With the admissible functions defined, the cantilever beam's potential energy can be defined solely as a function of its flexural strength, π_{beam}. Under these conditions, the methodology for Rayleigh-Ritz, as outlined in the previous section, is applied to determine the natural frequencies and associated mode shapes. The first five mode shapes are shown in Figure 4-3.
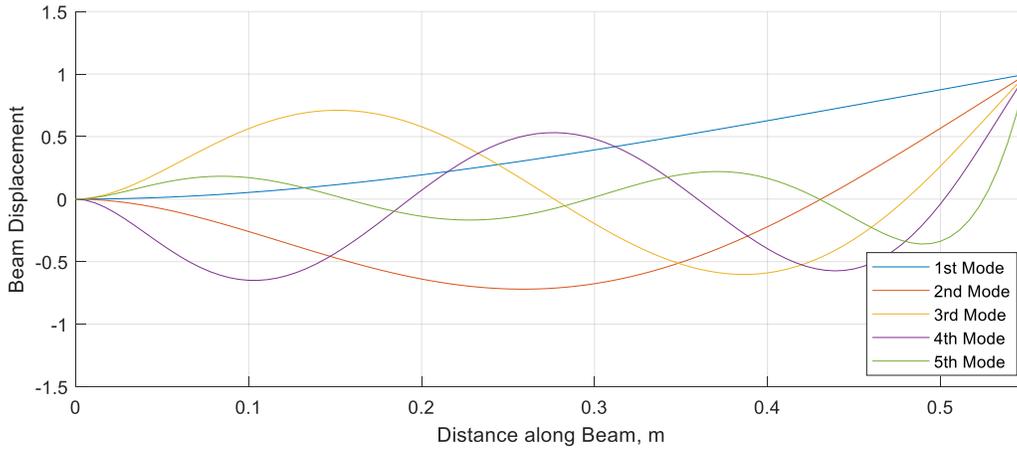
Figure 4-3: *First Five Mode Shapes of the Cantilever Beam Generated by the Rayleigh-Ritz Method*

A convergence study is conducted to validate the effectiveness of the Rayleigh-Ritz method. The Rayleigh-Ritz method is tested against the number of admissible functions used in order to determine an appropriate number of admissible functions such that the fundamental frequency converges. Figure 4-4 shows the convergence trend of the first five modes and confirms that the Rayleigh-Ritz can provide accurate solutions when using more admissible functions, but also confirms that this approximative method is only accurate for lower modes. The fourth and fifth mode shows poor convergence when using more admissible functions as the approximative solution drops below the analytical solution after having converged for lower number of admissible functions. Results also show that for the cantilever beam, Rayleigh-Ritz method can provide exact solution for the fundamental model using only two admissible functions.

58
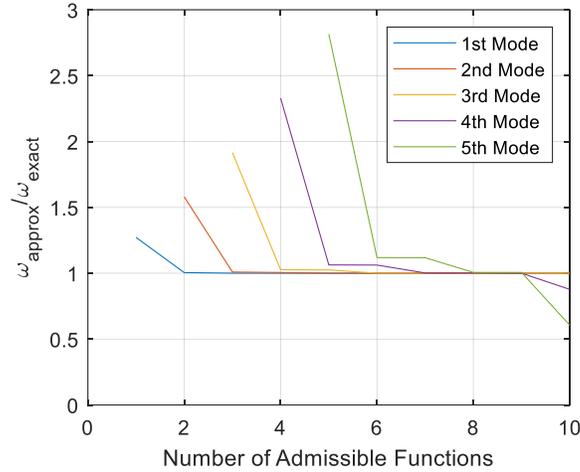
Figure 4-4: Convergence of the First Five Modes using Rayleigh-Ritz on a Cantilever Beam

4.3.4 Application of the Rayleigh-Ritz Method on the Alternative Beam Models

The Rayleigh-Ritz method is also applied onto both alternative models since analytical methods may not be possible in determining the natural frequencies. The dynamics of the alternative beam models discussed in section 4.2 are compared to that of the cantilever beam. The comparison is done by considering the ratio of fundamental frequencies between the alternative model, ω_{equiv}, and the cantilever model, ω_{rigid} as:

$$r = \frac{\omega_{equiv}}{\omega_{rigid}} \tag{4-31}$$

Eqn. (4-31) explains how far the dynamics of the alternative model has deviated from that of the cantilever model. In order for the dynamics to be as similar as possible, then the ratio of fundamental frequencies should approach unity.

The Rayleigh-Ritz method is initiated by first selecting appropriate admissible functions; however, selection of the admissible functions must be less constrained such that the springs provide the displacement resistance to satisfy the geometric boundary conditions [80]. Therefore, the Gram-Schmidt recursive algorithm is initialized with a non-normalized polynomial of the form $p_1 = \xi$. More details on the admissible functions and mode shape for the alternative models are given in section 4.4.

Convergence study of the Rayleigh-Ritz method on the alternative beams is shown in Figure 4-5 (b)-(c), which shows that the model having a torsional spring converges with a minimum of

three admissible functions while the model with an intermediate support requires a minimum of three admissible functions for good convergence; however, there appears to be a slight change in frequency when using more admissible functions. To ensure reasonable convergence of the Rayleigh-Ritz for all models, five admissible functions will be used such that there should be negligible changes in frequency for higher number of admissible functions.
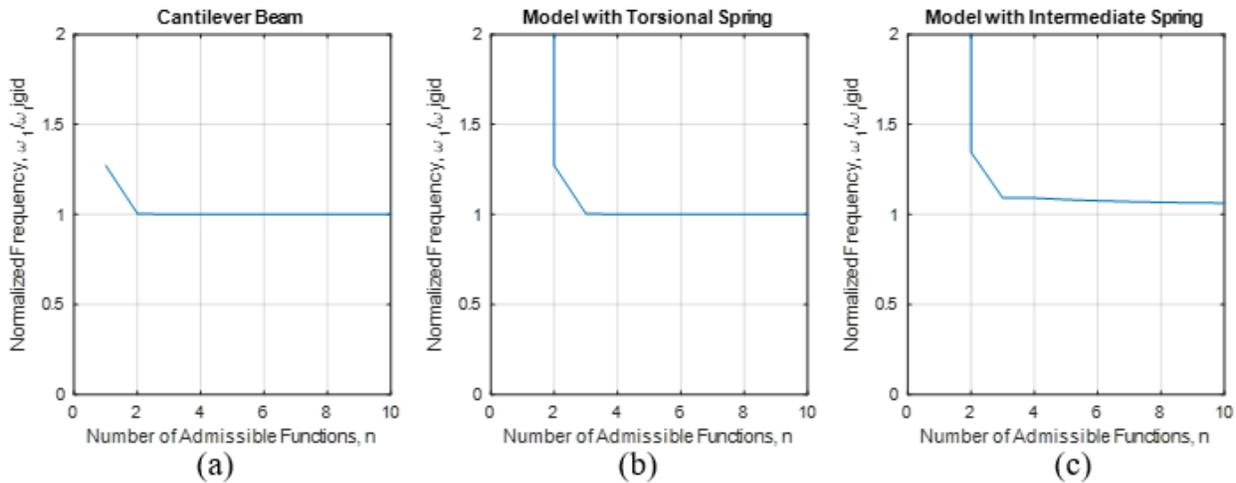
Figure 4-5: Convergence of Fundamental Frequency Ratio vs. Number of Admissible Functions using Rayleigh Ritz for (a) Cantilever Beam, (b) Torsional Spring Model, and (c) Overhang Support Model

The first five mode shapes of the equivalent model using a torsional spring at the pinned end and the equivalent model using an overhang support are shown in Figure 4-6 and Figure 4-7, respectively. The fundamental mode is comparably similar to that of the cantilever case since the angular deflection at the pinned end appears to be negligible. At higher modes, the condition of having no angular deflection at the pinned end is violated, mainly because the higher modes have high numerical error against their respective actual solution. This, again, relates to the fact that the Rayleigh-Ritz method is most accurate and suitable for lower modes.

60
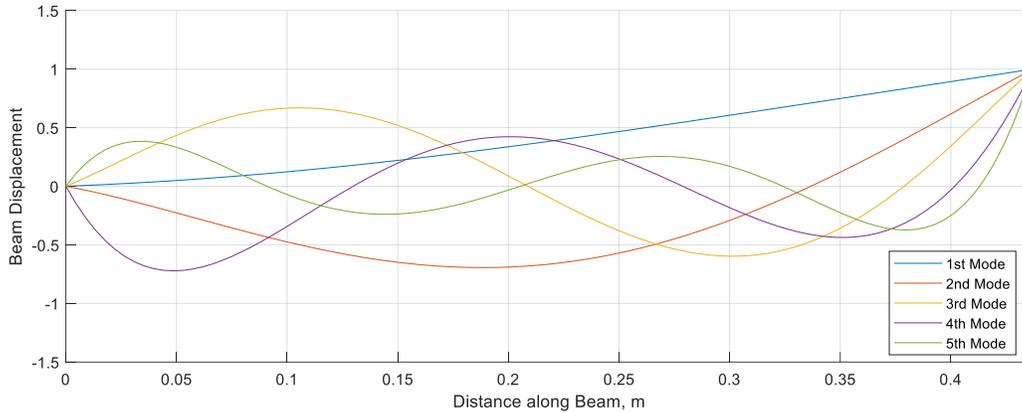
Figure 4-6: First Five Mode Shapes Generated by Rayleigh-Ritz of the Equivalent Beam with Torsional Support at Pinned End
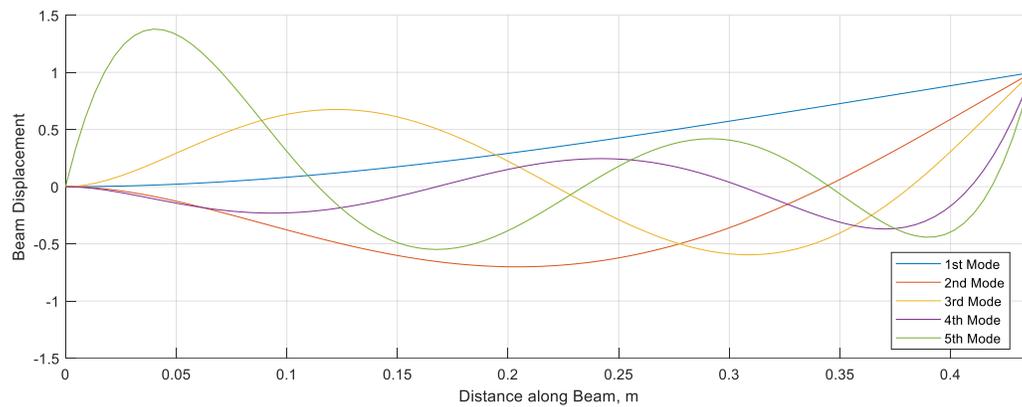
Figure 4-7: First Give Mode Shapes Generated by Rayleigh-Ritz of the Equivalent Beam with Overhang Support

Now that a convergence condition has been applied on the number of admissible functions, the Rayleigh-Ritz can be effectively used to accurately evaluate the natural frequency and associated mode shape of the alternative beam models. The fundamental frequency is then determined across stiffnesses ranging from 10^{-3} to 10^{6} with units respective to the type of spring used, either being torsional or linear. Results for the fundamental frequency of the alternative beams normalized with respect to that of the rigid cantilever beam are shown in Figure 4-8. Results in Figure 4-8(a) suggest that the fundamental frequency of the beam using a torsional spring at the support location approaches that of the cantilever model as the stiffness of the torsional spring increases. This is because the increased stiffness of the torsional spring hinders the rotational motion at the support, thus causing the slope at the support to approach zero. The beam with the intermediate spring has, however, slightly higher frequencies as shown in Figure 4-8(b). This is

61

partially to the fact that less length is considered cantilevered. Furthermore, the mismatch in fundamental frequency between the model using the intermediate spring and the cantilever beam may also be attributed to the slope condition being unsatisfied at the overhang support even at very high stiffness for the linear spring.

One additional outcome of interest is that each curve has three distinct ranges, denoted by sections I, II, and III, as displayed in Figure 4-8. The low range of stiffnesses (section I) shows a low gradient of frequency against stiffness, which means that there are small changes in natural frequency as the spring is stiffened. The mid range (section II) shows a steep gradient between natural frequency and stiffness, which is desired as this will provide a high amount of change in frequency for small changes in stiffness. The high range (section III) shows a similar trend as the low range but eventually shows saturation in the fundamental frequency. This is to say the size of the frequency shift is dependent on the range of stiffness considered, but also the beam geometry, which will be discussed in the next section. Overall, it is desirable to design the beam such that the frequency vs. stiffness behavior falls in section II to encourage large frequency shifts for small changes in stiffness.
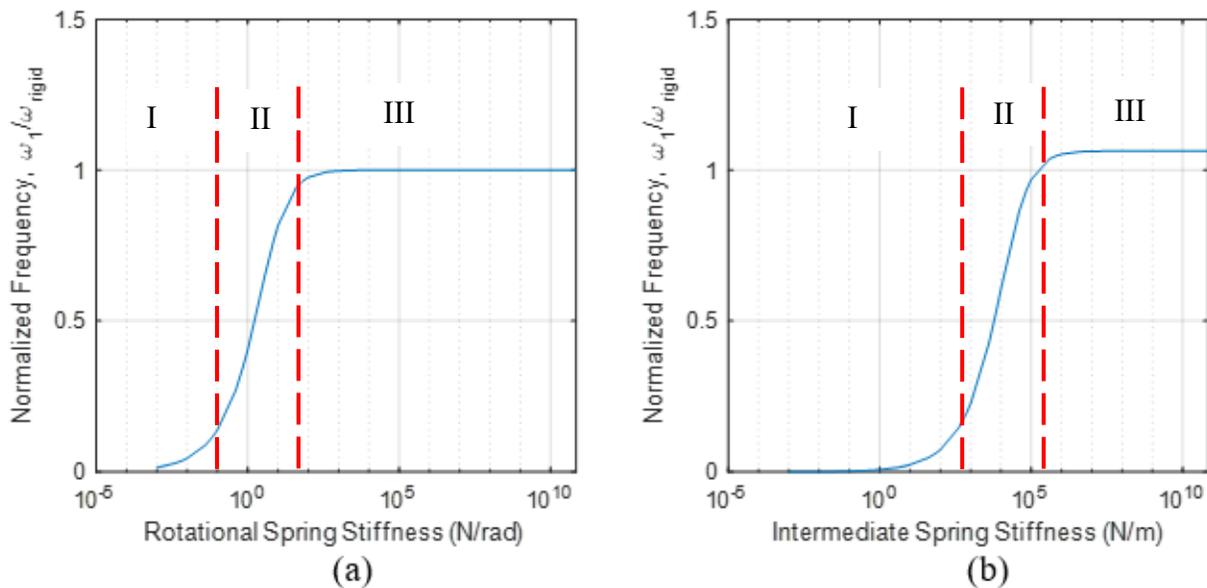
Figure 4-8: Normalized Fundamental Frequency vs. the Stiffness of a (a) Torsional Spring and (b) Overhang Linear Spring

4.4 Approximate Adaptive Beam Model and Geometry Selection

Two different modelling approaches have been discussed, which include the use of a torsional spring at the pinned location or a linear spring at the overhang location. The model selection depends on the feasibility of a future experimental setup. For the case of using a torsional spring, the MRE would need to be made subject to torsion at the support, which would be very challenging to implement for future experimental study. Thus, the model having the intermediate spring is selected since the MRE can be placed in such a way that it is in direct shear as shown in Figure 4-9. Two MRE pads placed in a parallel configuration are used as per the electromagnet design and to increase the stiffness at the support. The equivalent total complex stiffness due to the MRE in shear can be defined as:

$$k_{MRE} = \frac{2G^* A_{MRE}}{t_{MRE}} \tag{4-32}$$
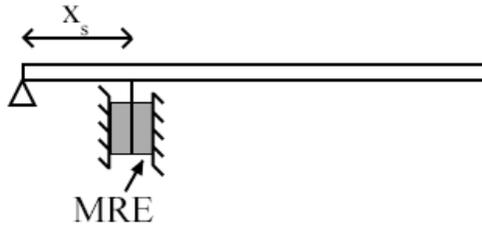
Figure 4-9: Approximate Beam Model using MRE in Shear at the Overhang Support Location

where t_{MRE} is the thickness of each MRE pad, $G^* = G' + jG''$ is the total complex shear modulus having both storage and loss moduli, and A_{MRE} is the shear area on the MRE.

The dynamics of the beam is also strongly dependent on the beam geometry. The beam dimensions are selected through a multi-objective constrained optimization problem. The cost function consists of a combination of two objective functions using weighting factors. The first objective function is to make the fundamental frequency of the equivalent model close to that of the cantilever model at the maximum magnetic flux density of 1 T. This can be done by ensuring that the ratio at 1 T, $r_{1\,T}$, defined by Eqn. (4-31) be maximized. The physical meaning behind this condition is that the beam can be considered closely cantilevered when the MRE is at its maximum stiffness. The second objective function is to have a maximum shift in fundamental frequency during a change in magnetic flux density from 0 to 1 T. By using Eqn. (4-31), the non-dimensional frequency shift can be defined as:

$$\Delta r = r_{1\,T} - r_{0\,T} \tag{4-33}$$

This ensures the vibration control capability using MRE for a wide range of frequencies.

It is assumed that MREs operate in the linear viscoelastic regime to prevent strain softening effect due to large amplitude deformation. As was discussed in section 2.3, the MRE considered in this research study approximately experiences linear viscoelastic behavior under a shear strain below 15%. This 15% shear strain is then accounted between the static and dynamic behavior of the beam. Generally, any system under vibratory motion oscillates about a static equilibrium point, which is generally dependent on the weight of the system. In this case, the static equilibrium point is enforced assuming a maximum shear strain of 5%, as shown in Figure 4-10. The remaining 10% shear strain is considered to be due oscillatory motion about the static equilibrium point.
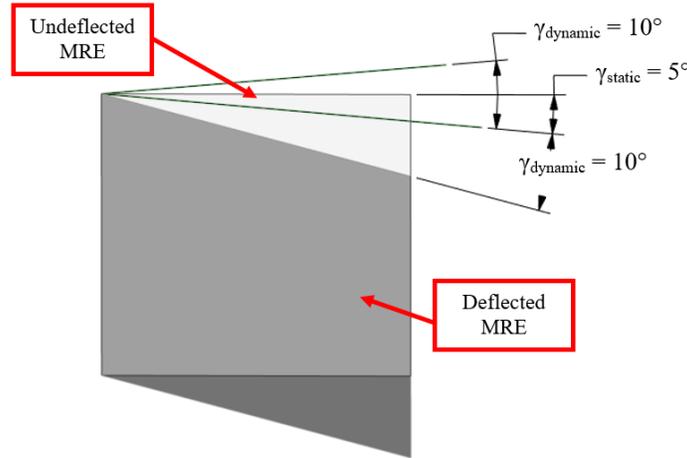
Figure 4-10: Static and Dynamic Shear Strain Representations on Deflected MRE

Figure 4-11 illustrates the free-body diagram under static loading, which will provide a relationship between the weight of the beam and the static deflection of the MRE. This functional relationship will provide a constraint in the optimization problem. The total strain is to be considered in the later chapters when the beam undergoes dynamic loading.
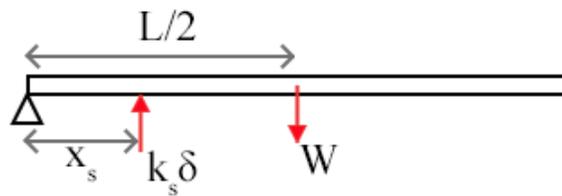
Figure 4-11: Free-Body Diagram of Proposed Beam Model under Static Loading

The design variables are the beam dimensions including the beam length, L, with a rectangular cross-section having width, b, and height, h. The placement of the MRE support is considered as a design variable and is defined in the form of a non-dimensional location along the beam, p, as:

$$p = \frac{x_s}{L} \tag{4-34}$$

At static equilibrium, a moment balance about the support yields:

$$(\rho g b h L)\frac{L}{2} = x_s k_s \delta \tag{4-35}$$

The static shear strain, γ, and the deflection at the support, δ, depend on the thickness of the MRE through the following expression:

$$\gamma = \frac{\delta}{t_{MRE}} \tag{4-36}$$

Since the system is under static conditions, then the stiffness due to the MRE is only dependent on the storage modulus. Furthermore, to ensure that the 5% static strain is respected, then equilibrium should be maintained when the MRE is under a magnetic flux density of 0 T since this represents the minimum stiffness. Hence,

$$k_s = 2\frac{G'_{0\,T}A_{MRE}}{t_{MRE}} \tag{4-37}$$

Substituting Eqns. (4-34), (4-36) and (4-37) into Eqn. (4-35) yields:

$$\rho g b h L = 4 p G'_{0\,T} A_{MRE} \gamma \tag{4-38}$$

Now to assure that the shear strain in the MRE under static loading is less than the allowable static strain, γ_{static}, of 5%, then the following condition should be met:

$$\rho g b h L \leq 4 p G'_{0\,T} A_{MRE} \gamma_{static} \tag{4-39}$$

Additional side constraints are applied on the geometry to prevent unrealistic dimensions and numerical inability during optimization iteration. From the dynamic conditions on the MRE discussed in section 2.3, the fundamental frequency under a magnetic flux density of 1 T should remain under 10 Hz. Finally, the constrained optimization problem can be formally formulated as:

$$\underset{b,h,L,p}{\textbf{Maximize}} \quad J = Cr_{1\,T} + (1 - C)(r_{1\,T} - r_{0\,T})$$

$$\textbf{Subject to} \quad \rho g b h L \leq 4 p G'_{0\,T} A_{MRE} \gamma_{static}$$
$$b \geq h$$
$$1\,mm \leq L \leq 500\,mm \tag{4-40}$$
$$10\,mm \leq b \leq 500\,mm$$
$$2\,mm \leq h \leq 500\,mm$$
$$f_{1\,T} \leq 10\,Hz$$

The MATLAB optimization toolbox was used to solve the optimization problem using the combination of the genetic algorithm (GA) and sequential programming algorithm (SQP). GA is initially used to find a near-region of the global optimum solution; this is then followed by sequential quadratic programming (SQP) to find the accurate global optimum in the vicinity defined by GA. The beam material is chosen to be aluminum to prevent interference with the applied magnetic field due to its very low magnetic permeability of 1.26E−6 H/m compared with steel [81]. An additional reason to the selection of aluminum is that it is mainly used for lightweight applications, where the density of aluminum is 2700 kg/m^3. The geometry of the MRE was determined in Chapter 3, and has width of 10 mm, length of 50 mm, and thickness of 8 mm. The storage modulus at 0 T, as per Eqn. (2-1), is 63.040 kPa.

The optimization was tested for different weights on the cost function. The area of the beam appeared to be unaffected by the weighting factor, but the beam length and non-dimensional support location varied according to the applied weighting factor. The results of the optimization problem under different weighting factors are provided in Table 4-2. The beam dimensions selected in the subsequent analysis is based on the weighting factor of 0.2 as this provides the highest shift (nearly 44%) in the natural frequency. This can also be shown in Figure 4-12, where the geometry selected produces frequency ratios in the region with the highest gradient of the frequency ratio vs. stiffness curve, which signifies that there will be a large frequency shift. Using Eqn. (4-37), the stiffness of the MRE section under a magnetic flux density of 0 and 1 T is 7880 N/m and 29584 N/m, respectively. Furthermore, for the results of the optimization problem having a weighting factor of 0.2, the constraint given by Eqn. (4-39) and those constraints representing the lower bound on beam width and height are active.

Table 4-2: Summary of Geometry Results for Different Cost Weights

	Cost Weight		
	0.2	**0.5**	**0.8**
Beam Length, l (mm)	437	531	777
Beam Width, b (mm)	10	10	10
Beam Thickness, h (mm)	2	2	2
Support location, p (%L)	3.7	4.5	6.5
Cantilever Fund. Freq. (Hz)	9.29	6.40	3.06
Fund. Freq. at 0 T (Hz)	4.99	4.56	2.85
Fund. Freq. at 1 T (Hz)	7.19	5.67	3.00
Frequency ratio at 0 T	0.537	0.773	0.913
Frequency ratio at 1 T	0.774	0.886	0.959
% Increase in Frequency	44.11	24.24	5.06
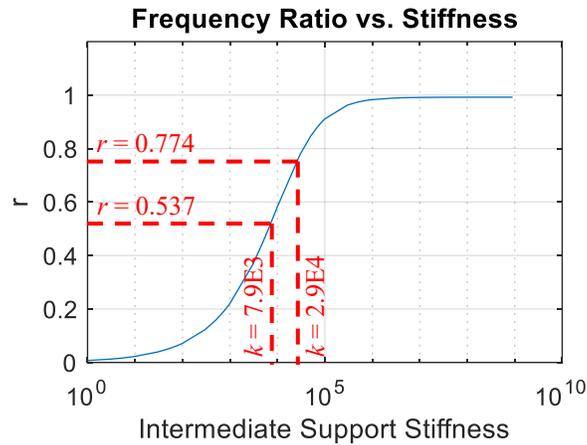
Figure 4-12: Mapping of Frequency Ratio at 0 and 1 T onto Stiffness vs. Frequency Ratio Curve

Solution to the eigenvalue problem in Eqn. (4-26) also gives the associated fundamental mode shape, which has the form of a 5th-order polynomial due to the linear combination of the five admissible functions used. The admissible functions along with their normalized eigenvector coefficients for the first mode under a magnetic flux density of 1 T are provided in Table 4-3. The mode shapes at both 0 and 1 T are shown in Figure 4-13. As discussed in section 4.3.4, the admissible functions are selected on the basis of reducing the constraint on the geometric boundary conditions allowing for angular deflection at the pinned support ($x = 0$), as can be seen in Figure 4-13. Furthermore, the effects of the linear spring can be seen on the mode shape, where the beam

has a slight bend due to the moment induced by the linear spring at the support location. Under a magnetic flux density of 1 T, it appears that the beam tip deflects more when compared to the MRE location (3.7% of the beam length from pinned support). This increase in deflection is due to the increase in stiffness, resulting in a larger bending moment on the beam at the support location.

The mode shape also serves the purpose of understanding the relationship between the beam tip and MRE deflection. For an 8 mm thick MRE pad with an allowable dynamic shear strain of 10%, this leads to an allowable dynamic deflection at the MRE location to be 2.14 mm. Because the MRE is located at 3.7% the length of the beam, then the corresponding deflection at the MRE location is about 2.5% that of the tip. This results in an allowable dynamic deflection of the beam tip to be about 85 mm to ensure that the MRE does not experience strain softening due to large shear amplitude.

Table 4-3: Normalized Eigenvector for the 1st Mode at 1 T and Admissible Functions

Index	$\widetilde{C}_i$	Admissible Function, ϕ_i
1	2.315	1.73ξ
2	0.811	$8.94\xi^2 - 6.71\xi$
3	0.380	$39.69\xi^3 - 52.92\xi^2 + 15.88\xi$
4	0.183	$168.00\xi^4 - 315.00\xi^3 + 180.00\xi^2 - 30.00\xi$
5	0.033	$696.49x\xi^5 - 1671.60\xi^4 + 1393.00\xi^3 - 494.33\xi^2 + 49.75\xi$
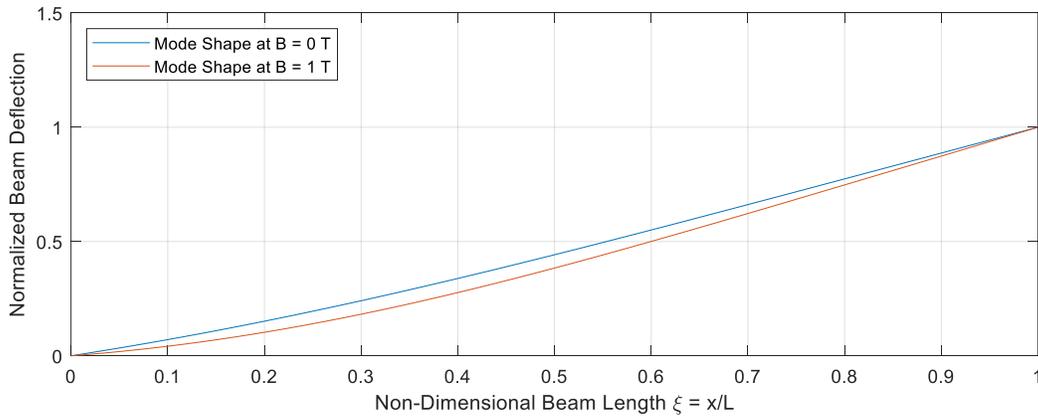
Figure 4-13: Mode Shape of Approximate Beam Model at 0 T and 1 T

4.5   Equivalent Single-Degree-of-Freedom (SDOF) System

Assuming that the dynamics of the continuous beam with MRE support is mainly dominated by its fundamental mode, then an equivalent SDOF model can be formulated to model the dynamic

behaviour of the beam. Therefore, the newly designed continuous model with an intermediate linear MRE spring is subsequently converted to a single-degree-of-freedom (SDOF) model. The developed SDOF model will greatly facilitate the development of control strategies to be discussed in the next chapter.

One general method of finding equivalent systems is by performing an energy comparison to determine an equivalent mass, spring, and damper. The equivalent SDOF model, as shown in Figure 4-14, is obtained by equating the kinetic and potential energies of the equivalent SDOF system to those of the continuous beam [82], [83]. By considering the displacement of the beam tip, $q(t)$, the dynamic beam displacement, $w(x,t)$, can be expressed in separate time and space domains as:

$$w(x,t) = X(x)q(t) \tag{4-41}$$

where $X(x)$ is the mode shape and $q(t)$ is the time-dependent generalized motion of the beam tip. The kinetic and potential energy of the SDOF and continuous system are equated and stated as follows:

$$\frac{1}{2}k_{eq}q^2 = \frac{1}{2}\int_0^L EI\left[\frac{dw}{dx}\right]^2 dx + \frac{1}{2}k_s[w(x_s)]^2 \tag{4-42}$$

$$\frac{1}{2}m_{eq}\dot{q}^2 = \frac{1}{2}\int_0^L \rho A w^2 \, dx \tag{4-43}$$

Substituting Eqn. (4-41) into Eqns. (4-42) and (4-43), the equivalent stiffness and mass can be obtained as:

$$k_{eq} = \int_0^L EI\left[\frac{dX}{dx}\right]^2 dx + k_s[X(x_s)]^2 \tag{4-44}$$

$$m_{eq} = \int_0^L \rho A X^2 \, dx \tag{4-45}$$

Substituting k_s from Eqn. (4-37) into Eqn. (4-44), yields a complex equivalent stiffness in the form of:

$$k_{eq} = k^* = k' + jk'' \qquad (4\text{-}46)$$
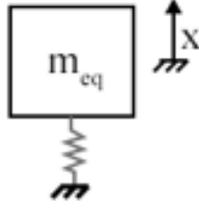
Figure 4-14: Equivalent Single-Degree-of-Freedom System k^*

Now having defined the equivalent mass and stiffness, the governing equation of the SDOF system shown in Figure 4-14 can be formulated as:

$$m_{eq}\ddot{x} + k^*x = f(t) \qquad (4\text{-}47)$$

Considering that the equivalent stiffness is in the complex form due to the MRE viscoelastic nature, then Eqn. (4-47) can be rewritten as:

$$m_{eq}\ddot{x} + (k' + jk'')x = f(t) \qquad (4\text{-}48)$$

Noting that the loss modulus describes the dissipation of energy in the complex stiffness, then the loss modulus can be replaced by an equivalent viscous damping. Therefore, the governing differential equation for the equivalent SDOF system can be described as:

$$m_{eq}\ddot{x} + c_{eq}\dot{x} + k'x = f(t) \qquad (4\text{-}49)$$

For structures having complex stiffness, the equivalent damping depends on both the loss component of stiffness and the operating frequency. For a harmonic input, the equivalent damping depends on the input frequency. For any other input, the beam should naturally vibrate at its fundamental frequency. The relationship between c_{eq} and the loss modulus can be thus stated as:

$$c_{eq} = \begin{cases} \dfrac{k''}{\omega} & \text{Forced Harmonic Input} \\ \dfrac{k''}{\omega_n} & \text{Otherwise} \end{cases} \qquad (4\text{-}50)$$

Eqns. (4-44) and (4-45) show that the equivalent mass and equivalent stiffness are dependent on the mode shape, which is also dependent on the stiffness of the MRE. Eqn. (4-50) depends on both the equivalent mass and stiffness through the natural frequency when considering any loading other than harmonic loading. The equivalent damping under harmonic loading is simply the loss

component of stiffness scaled down by the operating frequency. Therefore, the equivalent mass, spring, and damper are dependent on the input current as this drives the stiffness of the MRE. Curve fitting using the least-squares minimization method is used to obtain the functional relationship between each equivalent system parameter to the input current. Selection of the polynomial order is based on the root-mean-square-error (RMSE), which is shown in Figure 4-15. An RMSE of 1E−3 shows a goodness of fit for equivalent mass and equivalent damping, while an RMSE of 5E−2 provides good results for both storage and loss components of stiffness. Figure 4-16 visually shows the goodness of fit for each obtained polynomial by least-squares minimization to the data points obtained from solving directly Eqns. (4-44), (4-45), and (4-50). The field-dependent functional relations for storage and loss components of stiffness, equivalent mass, and equivalent damping with respect to applied current are found to be:

$$k'[I(t)] = -0.0047[I(t)]^5 + 0.0070[I(t)]^4 + 0.0632[I(t)]^3$$
$$- 0.2725[I(t)]^2 + 0.8334[I(t)] + 11.8511 \tag{4-51}$$

$$k''[I(t)] = 0.0141[I(t)]^3 - 0.0489[I(t)]^2 - 0.0446[I(t)] + 1.7226 \tag{4-52}$$

$$m_{eq}[I(t)] = 0.0066 \tag{4-53}$$

$$c_{eq}[I(t)]$$
$$= \begin{cases} \dfrac{k''[I(t)]}{\omega} & \textit{Forced Harmonic Input} \\ 0.0003[I(t)]^3 - 0.0011[I(t)]^2 - 0.0010[I(t)] + 0.0381 & \textit{Otherwise} \end{cases} \tag{4-54}$$

Although variations are present on the equivalent mass across the currents, the changes are relatively small such that the variations can be negligible. Furthermore, the curve fitting for the equivalent mass proposes a zeroth-order polynomial, suggesting that it is safe to assume that the mass remains constant at approximately 6.6 g, which is 28% of the total beam mass of 23.6 g.
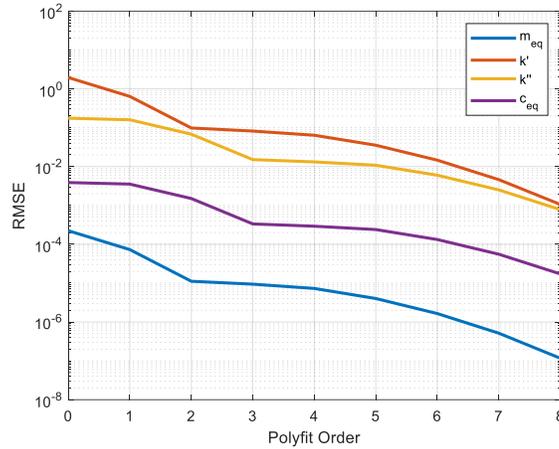
Figure 4-15: RMSE for Different Equivalent Mass, Equivalent Stiffness Storage and Loss Components, and Equivalent Damping Curve Fitting Polynomial Orders
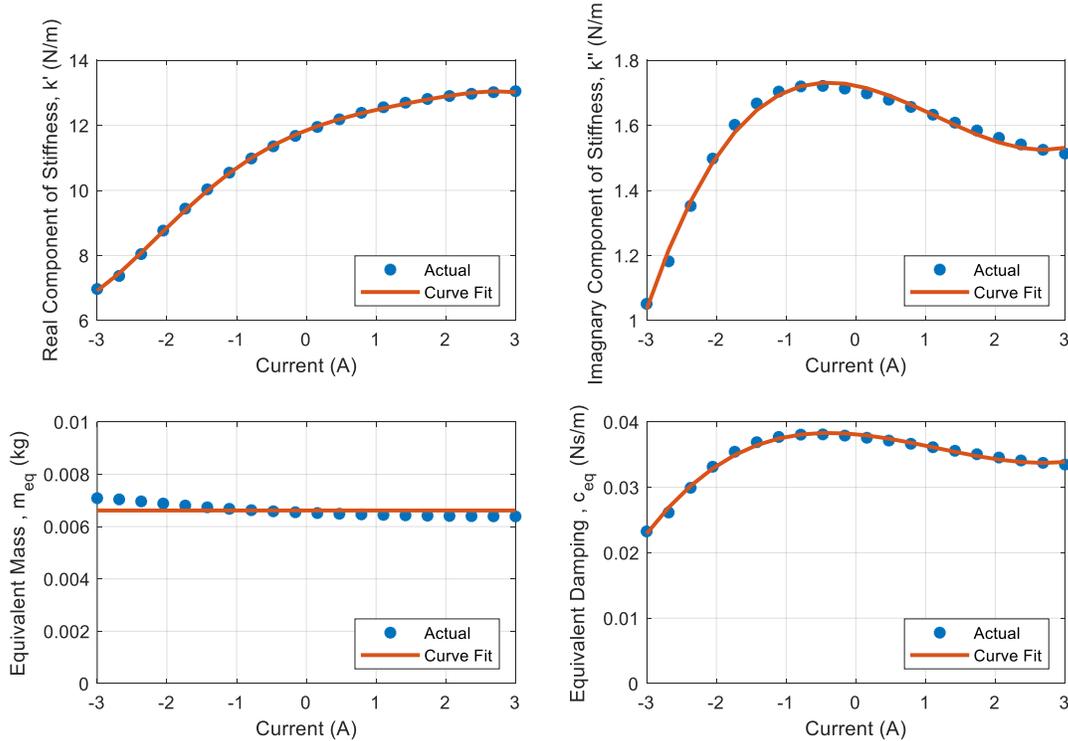
Figure 4-16: Curve Fit for Equivalent Stiffness Storage and Loss Components, Equivalent Mass, and Equivalent Damping

Validation of the equivalency between the continuous and SDOF systems is subsequently accomplished by comparing the fundamental frequencies across the range of input currents. Table 4-4 shows a comparison between the SDOF and continuous model's natural frequencies at various applied current, demonstrating that there is good agreement between the two systems. The small amount of error can be attributed to the deviation of mass to the curve-fitted equivalent mass of 6.6

g at low input current, shown in Figure 4-16. However, the percent error is small enough to be negligible. Hence, the SDOF system is capable of approximating well the dynamics of the fundamental mode of the continuous model.

Table 4-4: Comparison of Fundamental Frequency between Continuous Beam and SDOF Systems

Current (A)	Magnetic Field Density (T)	Fundamental Frequency (Hz)		
		Continuous	SDOF	% Error
−3	0.012	4.99	5.14	3.08
0	0.666	6.44	6.74	−0.50
3	0.982	7.19	7.06	−1.83

4.6 Performance of the Equivalent SDOF System

Prior to designing a controller, it would be beneficial to understand the behavior of the developed equivalent SDOF system. Such understanding requires both a time and frequency response analysis at different input currents. For the time response, the two key parameters identified are the settling time and percent overshoot since they can represent the capability of the system to attenuate vibration at specific currents. The frequency response is of key interest since a frequency shift can result in significant attenuation, especially when operating at resonance.

The proposed equivalent SDOF system has controllable performance characteristics since the coefficients of the characteristic equation of Eqn. (4-49) is dependent on the input current. The equivalent SDOF system is then considered an LTV system because of the variation of the characteristic equation with time. Figure 4-17 shows the path of the LTV system's poles when subject to an input current between −3 and 3 A, where each consecutive pole location is determined by unit increments in the input current. Firstly, this shows that for any input current, the system will always be stable. Secondly, unlike active controllers where implementation of a controller changes the overall pole locations and may cause a system to go unstable, the poles of this semi-active SDOF system will always travel along the path shown in Figure 4-17 and will never cause the system to go unstable. One trend to also note is that the real component of the poles has a minimum for an input current of −1 A. Physically speaking, the settling time is inversely proportional to the magnitude of the real component of the poles. Figure 4-17, therefore, shows that a maximum settling time occurs at −1 A passively.
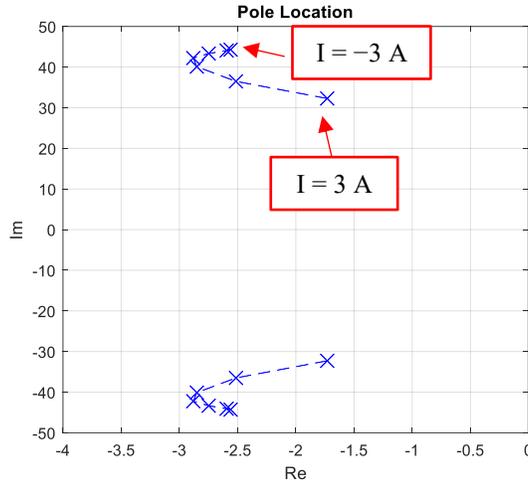
Figure 4-17: Path of Semi-Active System's Pole Location under Different Input Currents

4.6.1 Time Response of the SDOF System

The time response is studied by considering the performance characteristics as defined in section 1.2.2.1. The performance characteristics for the SDOF system is summarized in Table 4-5, showing variance in the settling time and percent overshoot for various input currents. For a passive system, it appears that both settling time and percent overshoot is best under zero current, as they both tend to increase when changing current in either direction.

Table 4-5: Summary of Performance Characteristics for the SDOF System

Current (A)	Magnetic Field Density (T)	Natural Frequency (Hz)	Damping Ratio	Damped Natural Frequency (Hz)	Percent Overshoot (%)	Settling Time (s)
−3	0.012	5.14	0.054	5.14	84.50	2.31
0	0.666	6.74	0.068	6.72	80.71	1.39
3	0.982	7.06	0.058	7.05	83.39	1.56

4.6.2 Frequency Response of the SDOF System

The form of the transfer function in Eqns. (1-22) and (1-24) provided in section 1.2.2.2 differ slightly when considering the differential equation in Eqn. (4-48) due to the complex stiffness. Following the same method as outlined in section 1.2.2.2, the magnitude of the transfer functions in both dimensional and non-dimensional forms for Eqn. (4-48) can be derived as:

74

$$\left|\frac{X}{F}\right| = \frac{1}{\sqrt{\left(k' - m_{eq}\omega^2\right)^2 + (k'')^2}} \qquad (4\text{-}55)$$

$$\left|\frac{k'X}{F}\right| = \frac{1}{\sqrt{(1 - r_n^2)^2 + \left(\frac{k''}{k'}\right)^2}} \qquad (4\text{-}56)$$

Figure 4-18 shows how the harmonic response changes under different applied current. The system shows a sufficient shift in natural frequency under a changing magnetic flux density by varying the currents from −3 to 3 A, as shown in Figure 4-18(a). The non-dimensional harmonic response in Figure 4-18(b) shows the increase in the transmitted force for an increase in input current when resonating at its fundamental frequency, which is due to the stiffening of the boundary condition through the MRE.
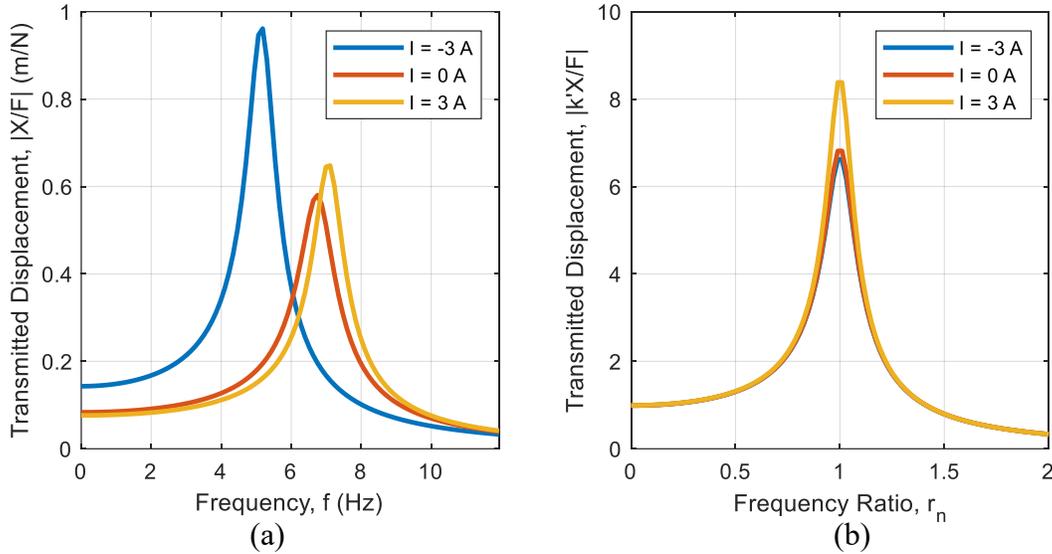
Figure 4-18: Dimensional (a) and Non-Dimensional (b) Harmonic Response

A unique approach can be taken to further understand the behavior of the system under harmonic load since the mechanical properties vary under the influence of a current-controlled magnetic flux density. Considering Eqn. (4-55), the effects of the input current on the frequency response can be investigated for the given input frequency. Thus Eq. (4-55) can be rewritten as:

$$\left|\frac{X}{F}\right| = \frac{1}{\sqrt{\left[k'(I) - m_{eq}\omega^2\right]^2 + [k''(I)]^2}} \qquad (4\text{-}57)$$

Because the system's mechanical properties are variable, then it is possible for the system to escape resonance when the input frequency matches the resonant frequency. Figure 4-19 illustrates the behavior of the admittance (ratio of displacement to input force) under varying current. Each curve shows the response when operating at a specific input frequency equal to the natural frequency at a given input current, as shown in the legend. For instance, it can be realized that for the operating frequency of 5.14 Hz which is equal to the natural frequency of the system under current −3 A, the highest peak is observed at −3 A confirming the resonance and then the response drastically reduces by increasing the current. Thus, at the given operating frequency, the variation of the applied current has the effect of moving the natural frequency away from the operating frequency thus escaping the effect of resonance.
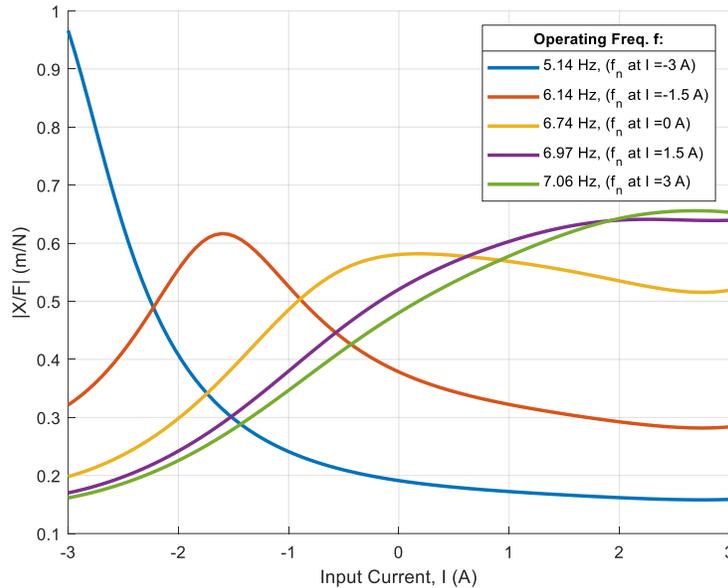
Figure 4-19: Harmonic Response for Fixed Input Frequency under Varying Current

4.7 Summary

An alternative cantilever model to incorporate MRE at the boundary condition has been developed. This was achieved by using the overhanging beam concept with MRE at the overhang support. The overhanging beam design is selected as it allows the MRE to be modelled in direct shear, for which the mechanical properties are readily available. The beam geometry was optimized such that there is a sufficient shift in frequency, resulting in a frequency shift of almost 44%. As a

result of the optimization problem, the harmonic frequencies are below 10 Hz, therefore the dependency of the mechanical properties against input frequency can be assumed negligible.

An equivalent SDOF system was subsequently formulated based on the fundamental mode and was analyzed to understand its time and harmonic response. The percent overshoot and settling time are two performance characteristics that are of interest in the time domain response. For the passive control, the best settling time occurs for an input current of zero. The percent overshoot increases with an increasing input current due to a decreasing damping ratio. The harmonic response shows significant attenuation of displacement at resonance frequency when performing a frequency shift through application of the current.

Chapter 5: Development of Control Strategies

5.1   Overview

In this chapter, different control approaches are explored for effectively dampening vibrations through adaptive boundary conditioning. As discussed in section 1.2.3, control strategies can be conducted through classical methods, such as PID control, and modern methods, such as state-feedback control. Control methods can further be categorized as either being online or offline control. Online control actively adjusts the actuation based on external disturbances and this is done during operation. Offline control requires a design of the actuation outside of operation and requires prior knowledge of the load spectrum. For example, passive control can be a form of offline control since the stiffness and damping are tuned prior to operation such that the vibration is suppressed. On the other hand, PID controller is of the online type as the actuation is regulated through the controller based on the error signal. Overall, the goal of these controllers is to suppress vibration. This is accomplished by demonstrating a decrease in the settling time under free-vibration response and a decrease in amplitude under harmonic or random loading. Different control strategies have been effectively utilized for semi-active vibration control using MRE technology.

The most straightforward control method involves employing the passive approach, where no control input is used. In this research study, the passive system under an input current of 0 A is to be used as a base model for comparative purposes. The modelling approach is described in section 5.2.

An offline optimal control law is designed in section 5.3 using the nonlinear mathematical programming technique. The optimization problem determines the time history of the input actuation, or current, applied to the MRE-based support system to minimize the settling time, input energy, and state energy. The online classical PID control is discussed in section 5.4. PID control generally requires trial-and-error to determine the tuning parameters such that the design performance criteria are met; however, in this study, tuning parameters are identified using nonlinear mathematical programming technique through minimization of the settling time, state energy, and percent overshoot. State-feedback control is a control strategy in which the complete or partial state variables of a system is used to calculate and apply control actions, aiming to regulate the system's behavior and achieve desired performance. Using state-feedback approach,

an on-off control strategy has been formulated in section 5.5. The formulated on-off control is similar to the VSC skyhook logic controller dedicated to semi-active systems.

The control systems are simulated in Simulink within the MATLAB environment. Simulink is capable of solving complex differential equations via block diagram representation. The development of the block diagrams for each control model and the overall setup, including inputs, is discussed in detail in section 5.6.

5.2 The Passive System

The passive system does not require a controller and will be considered as the system with an input current to the electromagnet set to 0 A. It is noted that even when the actuation input current is absent, the magneto-rheological elastomer (MRE) remains engaged solely because of the presence of permanent magnets. Full analysis of the passive system for different input currents was conducted in section 4.6; however, this comparative study considers a zero-input current passive system.

The governing differential equation for the equivalent SDOF system developed in Chapter 4 and formulated in Eq. (4-49) can be rewritten in a more general form as:

$$m_{eq}\ddot{x} + c_{eq}[I(t)]\dot{x} + k'[I(t)]x = f(t) \tag{5-1}$$

Therefore, the passive system in the absence of the applied current can be described as:

$$m_{eq}\ddot{x} + c_{eq}[0]\dot{x} + k'[0]x = f(t) \tag{5-2}$$

Since the mechanical properties are dependent on current, then the undamped natural frequency, damping ratio, and damped natural frequency can also be defined as functions of the current using the following relations:

$$\omega_n[I(t)] = \sqrt{\frac{k[I(t)]}{m_{eq}}} \tag{5-3}$$

$$\zeta[I(t)] = \frac{c_{eq}[I(t)]}{2m_{eq}\omega_n[I(t)]} \tag{5-4}$$

$$\omega_d[I(t)] = \omega_n[I(t)]\sqrt{1 - \{\zeta[I(t)]\}^2} \tag{5-5}$$

The complete response of the passive system under zero input current is then written as the superposition of the transient free response and forced vibration response using Duhamel's integral as [25]:

$$x_{passive}(t) = e^{-\zeta_0 \omega_{n_0} t} \left[x(0) \cos \omega_{d_0} t + \frac{\dot{x}(0) + x(0)\zeta_0 \omega_{n_0}}{\omega_{d_0}} \sin \omega_{d_0} t \right]$$

$$+ \int_0^t \frac{1}{\omega_{d_0}} e^{-\zeta_0 \omega_{n_0}(t-\tau)} \sin \omega_{d_0}(t - \tau) F(\tau) d\tau$$

(5-6)

Note that the subscript of 0 denotes the vibration characteristics at 0 A while $x(0)$ and $\dot{x}(0)$ represent the initial conditions on position and velocity, respectively.

5.3 Development of an Optimal Control Law using NLP

The objective of the optimal control law is to determine the optimal time-history of the actuation input through the nonlinear programming (NLP) mathematical optimization problem. The optimal control of the system can be formally formulated using a multi-objective constrained optimization problem with three weighted objective functions including the settling time, state energy, and input energy as:

$$\begin{aligned}
\underset{I_i}{\textbf{Minimize}} \quad & J = C_1 T_s + C_2 \int_0^T x^2 \, dt + C_3 \int_0^T I^2 \, dt \\
\textbf{Subject to} \quad & m_{eq}\ddot{x} + c_{eq}[I(t)]\, \dot{x} + k'[I(t)]\, x = f(t) \\
& x(0) = x_0, \dot{x}(0) = v_0 \\
& -3 \le I(t) \le 3
\end{aligned}$$

(5-7)

where the first term in the multi-objective objective function, J, is the settling time T_s multiplied by the weight factor C_1 and second and third terms represent the state energy and input energy weighted by factors C_2 and C_3 , respectively. The system is constrained to satisfy the governing equation of motion in Eqn. (5-1) under initial displacement and velocity conditions. Moreover, the actuation current is restricted between −3 A and 3 A as per the electromagnet design. To find the time-history of the actuation current, $I(t)$, that minimizes the above multi-objective optimization problem, the time domain should be discretized. Because the system is inherently an LTV system, approximation methods are required in order to solve the governing differential equation in Eqn. (5-1). If the input current is varied between discrete points, then the response would be

80

difficult to derive analytically since it would require solving the LTV differential equation of the following general form, which can be obtained by inserting Eqns. (4-51)-(4-54) into Eqn. (5-1).

$$m_{eq}\ddot{x} + \left\{\sum_{n=0}^{4} a_n [I(t)]^n\right\}\dot{x} + \left\{\sum_{n=0}^{4} b_n [I(t)]^n\right\}x = 0 \tag{5-8}$$

Solution to the above differential equation is only possible if the input current is constant between discrete points, causing the system to behave as an LTI system for which analytical solutions exist. Therefore, the time response between discrete points can be formulated as the following:

$$x_{i,NLP}(t) = e^{-\zeta_I \omega_{n_I}(t-t_i)}\left[x_i \cos \omega_{d_I}(t-t_i) + \frac{\dot{x}_i + x_i \zeta_I \omega_{n_I}}{\omega_{d_I}} \sin \omega_{d_I}(t-t_i)\right]$$

$$+ \int_0^t \frac{1}{\omega_{d_I}} e^{-\zeta_I \omega_{n_I}(t-\tau)} \sin \omega_{d_I}(t-\tau) F(\tau)d\tau \tag{5-9}$$

Note that the subscript, I, on the vibration characteristic parameters (ω_{d_I}, ω_{n_I}, ζ_I) defines that they are dependent on the applied current. One issue with the time response is finding a solution to Duhamel's integral for different types of input loads. The solution to Duhamel's integral is determined numerically by applying a four-point Gauss quadrature to reduce numerical error. The Gauss quadrature estimates the integral by applying the following general estimating equation [84]:

$$\int_1^1 f(x)\, dx \approx \sum_{i=1}^{4} C_i f(x_i) \tag{5-10}$$

where C_i are weighting coefficients and x_i are the Gauss points. The Gauss quadrature is defined for integrals having bounds of integration from -1 to 1. For a general bounds of integration from a to b, a transformation must first be done by doing the following variable transformation:

$$x = \frac{1}{2}[t(b-a) + a + b]$$

$$dx = \frac{1}{2}(b-a)dt \tag{5-11}$$

The corresponding Gauss points and weighting coefficients provided in Table 5-1 can be used in Eqn. (5-10) to estimate Duhamel's integral for any load type [84].

	Weighting Coefficient C_i	Gauss Points x_i
1	0.3478548	−0.86113631
2	0.6521452	−0.33998104
3	0.6521452	0.33998104
4	0.3478548	0.86113631

The optimization problems have been solved in MATLAB using the hybrid GA-SQP algorithm to find the optimal controller law. Because the time domain has been discretized, the state and input energy objective functions are calculated using the trapezoidal numerical approach in determining the integral. To validate the results from NLP, the optimized input current is used as a feedforward input signal to the Simulink model and compared against the result from Eqn. (5-9), which represents the dynamics in the NLP problem.

5.4   Modelling the PID Control

The PID is a classical controller that is widely used in the field of control. PID controllers are fine-tuned through the utilization of transfer function analysis. This approach hinges on the performance of the system being influenced by its poles. This signifies that the system's time response is contingent upon where the poles are positioned. The PID controller is commonly formulated using the root-locus approach, aiming to achieve favorable performance by strategically positioning the system's poles [24]. However, in semi-active control, design via root locus is not possible since the system is LTV due to the behavior of the field-dependent stiffness and damping.

Within active control systems, the PID controller delivers the necessary directives to the actuator in order to achieve the desired actuation. PID control can be applied to MRE-based semi-active systems with some limitations. Rather than controlling an actuator, the PID controller will control the electromagnet current to modify the stiffness and damping of the system [50]. Furthermore, the electromagnet current must be clipped between −3 A and 3 A as per the electromagnet design.

The ordinary differential equation corresponding to the semi-active system can be transformed into a form resembling that of the active system, by accounting for the alterations in damping and spring forces as the actuation. The MRE stiffness and damping properties of the MRE under applied current, $I(t)$, to the electromagnet can be described as:

$$k'[I(t)] = k'[0] + \Delta k'[I(t)] \tag{5-12}$$

$$c_{eq}[I(t)] = c_{eq}[0] + \Delta c_{eq}[I(t)] \tag{5-13}$$

in which $k'[0]$ and $c_{eq}[0]$ are the stiffness and damping of the MRE under zero current and $\Delta k'[I(t)]$ and $\Delta c_{eq}[I(t)]$ are the changes in the stiffness and damping due to the applied current. Eqns. (5-12) and (5-13) show that the stiffness and damping can be expressed as a nominal term at a current of 0 A and an incremental term dependent on the input current. Replacing the field-dependent equivalent damping and stiffness in Eqns. (5-12) and (5-13) into Eqn. (5-1) for the case of free vibration $(f(t) = 0)$ yields:

$$m_{eq}\ddot{x} + \{c_{eq}[0] + \Delta c_{eq}[I(t)]\}\dot{x} + \{k'[0] + \Delta k'[I(t)]\}x = 0 \tag{5-14}$$

Rearranging the above equation results in an equivalent active control form, expressed as:

$$m_{eq}\ddot{x} + c_{eq}[0]\dot{x} + k'[0]x = u(t) \tag{5-15}$$

where the input actuation is defined as:

$$u(t) = -\left(\Delta c_{eq}[I(t)]\dot{x} + \Delta k'[I(t)]x\right) \tag{5-16}$$

The actuation is now dependent on the generated loads due to the changes in both stiffness and damping as a function of the input current.

The primary drawback of PID control lies in the process of selecting the tuning parameters, which typically involves a trial-and-error approach. To address this limitation, in this study, the tuning parameters for the PID controller are established through optimization, employing a multi-objective cost function. The multi-objective function consists of the settling time, peak value, and state energy, each multiplied by a weighting factor. For enhanced numerical analysis, the settling time and peak value of the PID-controlled system are normalized using the settling time and peak value of the passive system. The optimization problem is constrained to follow the dynamics defined by Eqns. (5-15) and (5-16). Theoretically, the tuning parameters can be any real number but to have more realistic values, the tuning parameters are also constrained such that their magnitudes do not exceed 1E5. For active systems, the tuning parameters are generally positive to prevent the creation of an unstable pole; however, for semi-active systems, negative tuning parameters are possible since they won't cause the system to be unstable since the poles travel a fixed path shown in Figure 4-17. The optimization problem to find the proportional, integral, and

differential tuning parameters (K_P, K_I, K_D) of the PID controller can thus be formally formulated as:

$$\underset{k_P,k_I,k_D}{\textbf{Minimize}} \quad J = C_1 \frac{T_s}{T_{s,passive}} + C_2 \frac{X_{peak}}{X_{peak,passive}} + C_3 \int_0^T x^2 \, dt$$

$$\textbf{Subject to} \quad m_{eq}\ddot{x} + c_{eq}[0]\dot{x} + k'[0]x = -\big(\Delta c_{eq}[I(t)]\dot{x} + \Delta k'[I(t)]x\big)$$

$$x(0) = x_0, \dot{x}(0) = v_0$$
$$-1E5 \leq K_P \leq 1E5$$
$$-1E5 \leq K_I \leq 1E5$$
$$-1E5 \leq K_D \leq 1E5$$
$$-3 \leq I(t) \leq 3$$

$$(5\text{-}17)$$

Solution to the optimization problem will be provided in the next chapter, showing the effects of different weighting factors on the performance characteristics described in section 1.2.2.1.

Prior to solving the optimization problem, the behavior of the tuning parameters is first studied by looking at the combined effects of integral and derivative control, where the tuning parameters are all fixed at 1000. K_P alone simply amplifies the error signal but gets clipped between -3 and 3 due to the limitation on the ampacity of the wire. Figure 5-1(a) shows that the addition of integral control to the proportional control causes a downward shift on the input current while maintaining the phase. Figure 5-1(b) shows that the effects of adding derivative control to the proportional control causes further amplification but also adds phase shift. One significant outcome of PID control is that the integral gain can cause a downward shift on the input current for positive gain and an upward shift for negative gain.
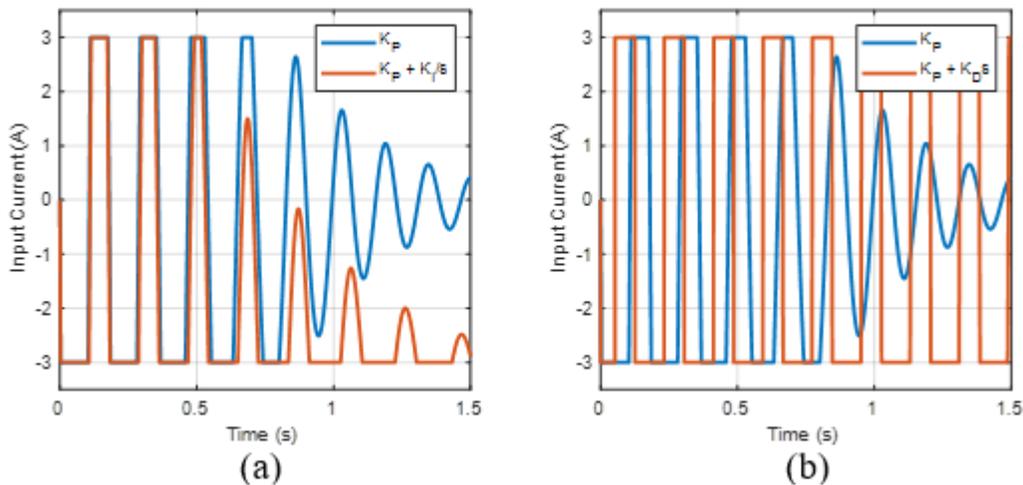
Figure 5-1: Effect of (a) Integral Control and (b) Derivative Control added to Proportional Control

5.5 Modelling the On-Off Control

Modern control theory offers supplementary control laws that effectively address the limitations inherent in classical control theory. A case in point is the state-feedback control, which can yield comparable outcomes to PID control without necessitating the iterative process of trial-and-error for controller parameter identification. Furthermore, modern control theory introduces an alternative category of controllers termed optimal controllers. In this research study, the time-optimal control law known as the on-off controller has been formulated for the equivalent SDOF system featuring MRE. To understand the on-off controller, the input actuation force defined in Eqn. (5-15) must be defined with some logic function, $g(t)$, which represents the on and off conditions of the current. The input function can then be formulated as:

$$u(t) = -\left\{\Delta c_{eq}[g(t)]\dot{x} + \Delta k'[g(t)]x\right\} \tag{5-18}$$

Gu et al. [8] proposed an on-off controller, which activates the MRE during deviations from the equilibrium point and takes the form:

$$g(t) = \begin{cases} 1 & x\dot{x} > 0 \\ 0 & x\dot{x} \leq 0 \end{cases} \tag{5-19}$$

The control law for $g(t)$ follows a similar logic to that of the skyhook controller, where the MRE is activated as the system moves away from its equilibrium position. The electromagnet design in this study, however, considers the off state as having a current of -3 A and the on state as having a current of 3 A. Therefore, the control law for $g(t)$ in this study is defined as:

$$g(t) = \begin{cases} 3 & x\dot{x} > 0 \\ -3 & x\dot{x} \leq 0 \end{cases} \tag{5-20}$$

This control law demonstrates that the system's stiffness and damping reach their peak when the system deviates from equilibrium, resulting in heightened resistance to movement. Conversely, as the system approaches equilibrium, stiffness and damping are minimized, expediting the system's convergence to the equilibrium point by reducing resistance to motion.

5.6 Simulink Model Layout

The Simulink model developed in this research study simulates four different systems driven by an input selector, as seen in Figure 5-2. The different systems modelled in Simulink are the passive, PID-controlled, on-off-controlled, and NLP-controlled systems. The displacements and

current-controlled inputs for each system, and external force is sent to the MATLAB workspace for post-processing.
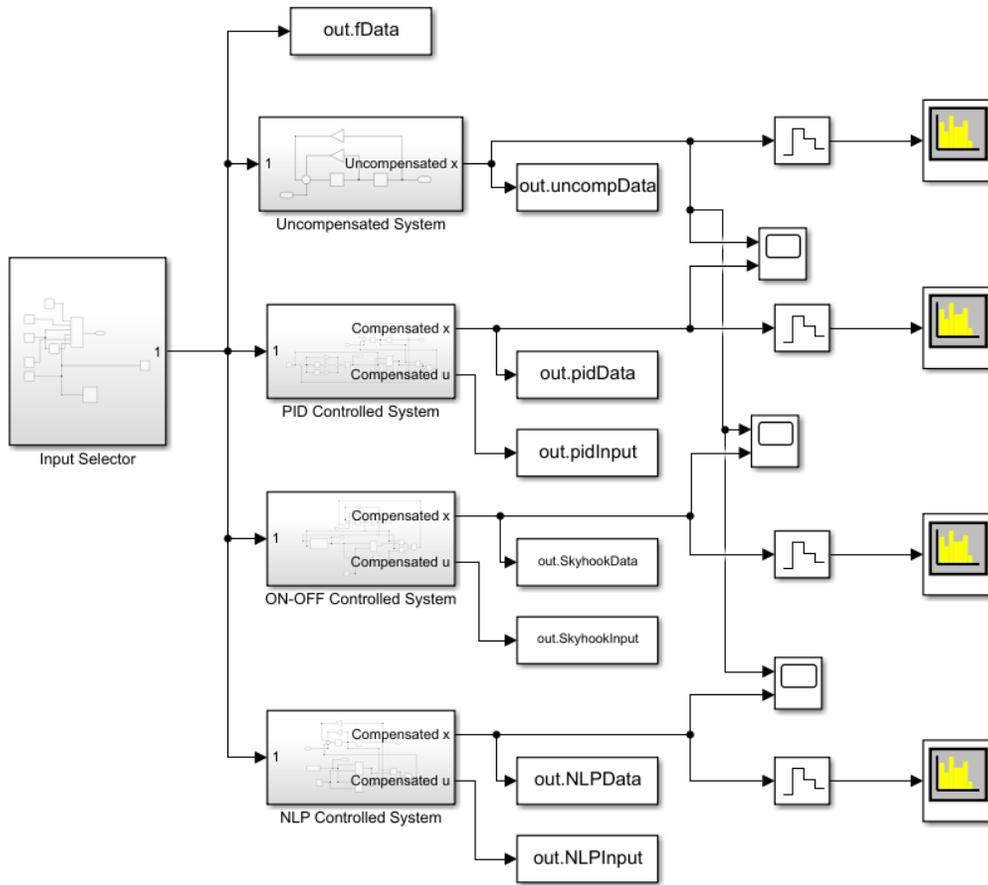
Figure 5-2: Simulink Model Overview

As shown in Figure 5-3, the input selector allows for five different loading scenarios, which are either no load, step load, impulse load, harmonic load, or random load. The no load case is used mainly for systems under free vibration with initial conditions. Simulink does not have an impulse input block, therefore it is created using a step function passed through a derivative block since the impulse, by definition, is the derivative of a step function. Although not all input types are used in this research study, they remain in the model for other possible applications and future analyses.
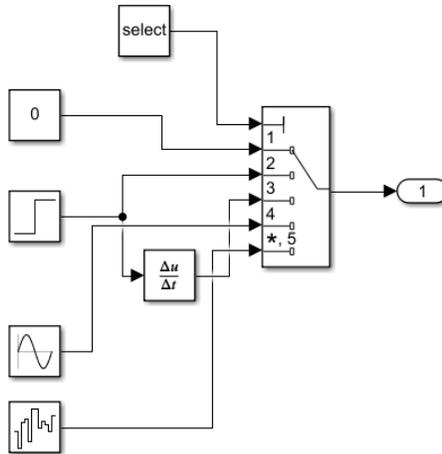
Figure 5-3: Simulink Model for Input Selector

The Simulink passive system, represented in Figure 5-4, is simply a representation of Eqn. (5-2) in block diagram form, having gain blocks $c0$ and $k0$ representing the equivalent damping and stiffness at an input current of 0 A, respectively. The block diagram of the passive system serves as the foundational framework for constructing the block diagrams of the PID, on-off, and NLP control systems.
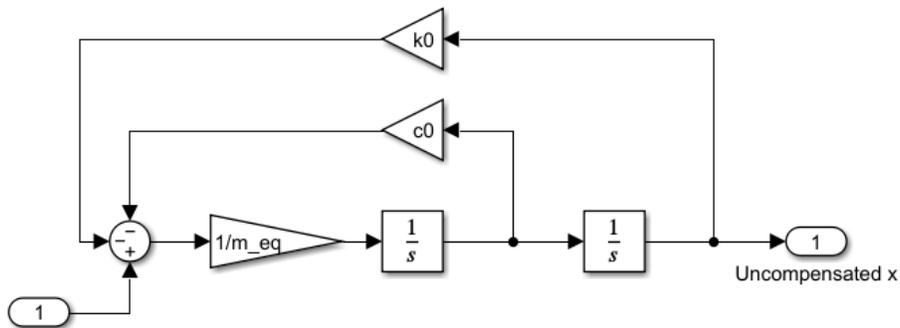
Figure 5-4: Simulink Model for the Passive System

In the PID model, as illustrated in Figure 5-5, it is essential to determine an error signal. This error signal is obtained by measuring the difference between a reference value and a signal acquired from the displacement. For the free vibration, this reference value is set to zero since the system decays to zero displacement. The error signal is then passed to the PID controller, which outputs the current through a saturation block. The purpose of the saturation block is to clip the input current signal between −3 A and 3 A. The clipped input signal is passed to two separate polynomial blocks, which determines the shift in damping and stiffness according to Eqns. (4-51) and (4-54).

The actuation is then included into the system by multiplying the damping with the velocity and the stiffness with the displacement, which are added together to form the actuation according to Eqn. (5-16).
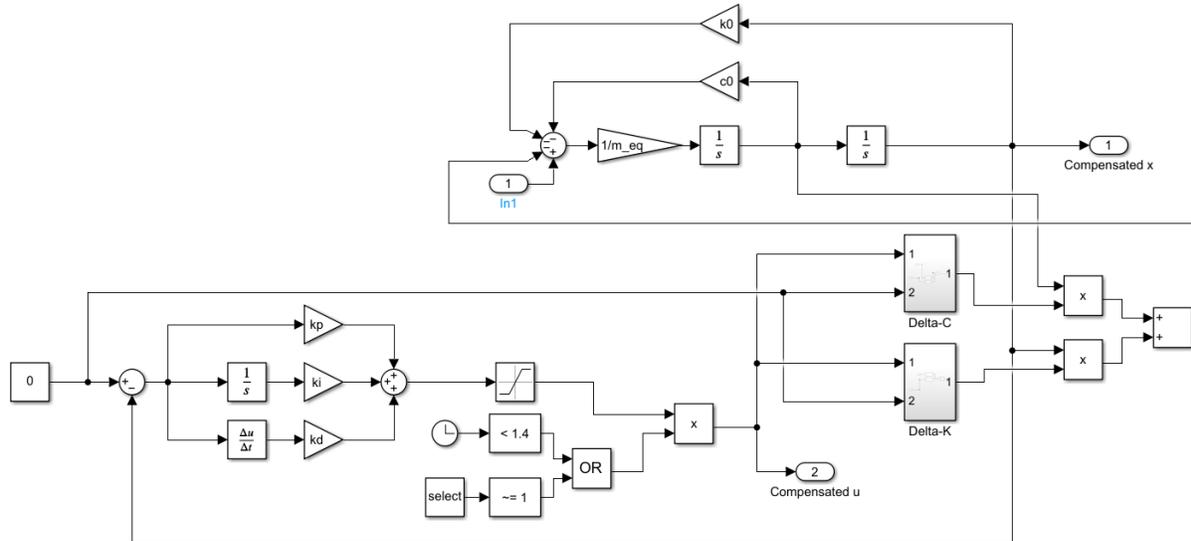
Figure 5-5: Simulink Model for PID-Controlled System

The on-off control, as shown in Figure 5-6, requires the position and velocity to be analyzed in order to satisfy the logic described by Eqn. (5-20). The position and velocity are passed through a function block representing the logic, where the output is the logic output as per Eqn. (5-20). Similar to the PID system, the output of the logic block is the input current, which is then returned as an actuation to the overall system.
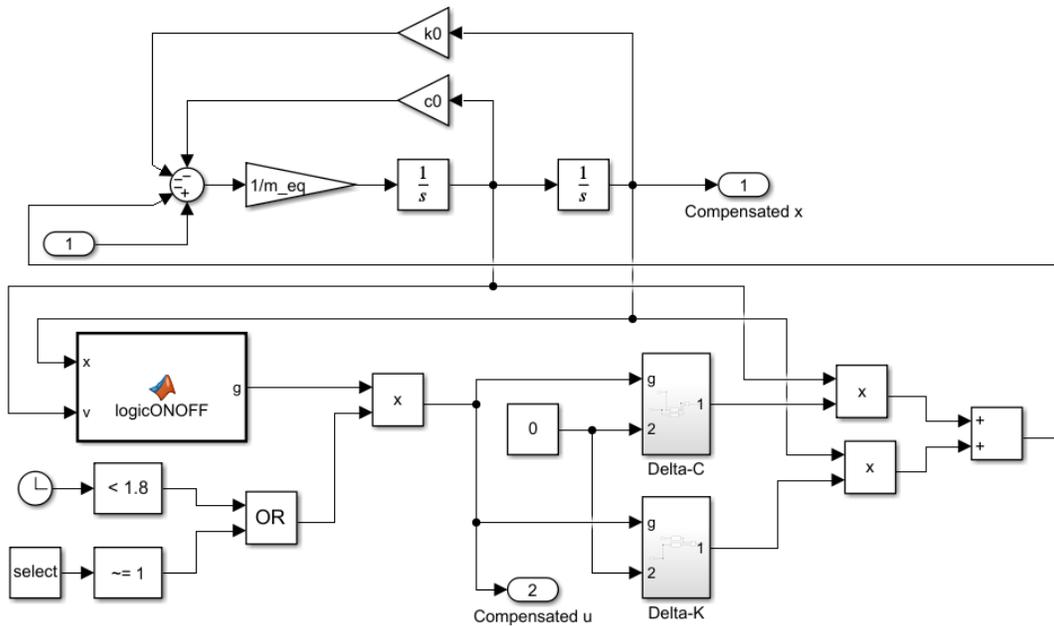
Figure 5-6: Simulink Model for On-Off-Controlled System

The NLP follows the same construct as the previous models; however, because NLP is designed offline, it is implemented using a feedforward approach. The result from NLP optimization is retrieved from the MATLAB workspace and is sent to the polynomial blocks.
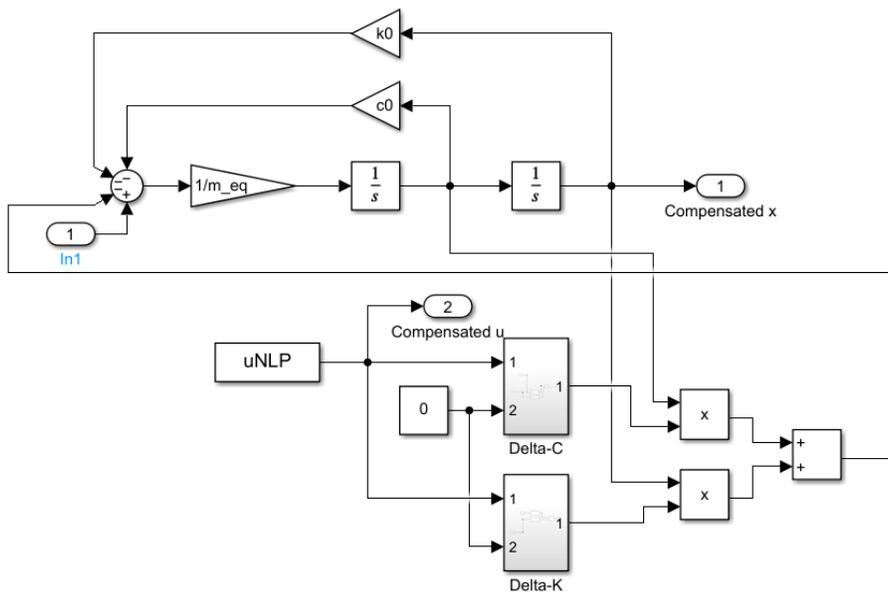
Figure 5-7 Simulink Model for NLP-Controlled System

Generally for active systems, the actuation goes to zero once all motion has been damped. Physically, this should also occur for semi-active systems, however, Figure 5-8 shows that both PID and on-off controllers never reach an input current of zero even at steady-state. Mathematically speaking, semi-active systems only change the behaviour of the time response described in Eqn. (1-8), which is governed by the exponential decay function. The exponential decay function asymptotically approaches zero, which means that the displacements never damp to exactly zero mathematically. For this reason, the input current never returns to zero once all dynamics is seemingly gone. On the other hand, the PID_{Ts} system does show a steadying of the input current, but to a value of -3, which was discussed previously as being due to the integral tuning causing a shift in current. Since the PID_{Ts} system is dependent on a diminishing error signal over time, then the input current steadies into a constant value. This occurs because of the magnitude of error over time being close to zero, where any amplification of a near-zero error will result in no changes in control.
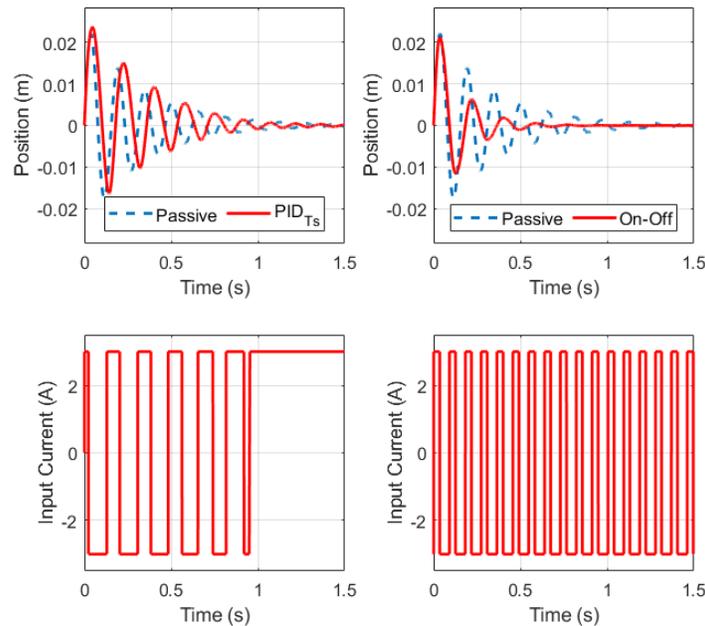
Figure 5-8: Example of Non-Zero Input for PID and On-Off Controllers Past Settling Time

To alleviate this issue, a logic is used to force the control law to zero once the system's dynamics have practically settled. Modification to both PID and on-off controllers requires knowledge of the settling time, which is to be discussed in the subsequent chapter. Once the simulation time

90

surpasses the settling time, then the input is forced to zero. The block diagram describing the input-off logic is shown in Figure 5-9.
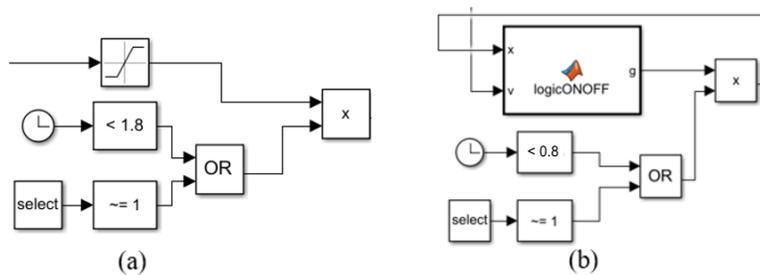
Figure 5-9: Modification to Controller Input for (a) PID and (b) On-Off

5.7 Summary

The control analysis of the MRE-based system will be accomplished using an offline optimal control approach determined by NLP, and two online control approaches using PID and on-off control. The NLP controller is designed to either minimize settling time, state energy, or input energy by adjusting the cost function's weighting coefficients. Selection of the PID tuning parameters is to be determined using NLP rather than by trial-and-error in order to either minimize the settling time, peak value, or state energy. The on-off controller logic was determined using similar logic to the skyhook controller, which causes an increase in stiffness and damping as the system moves away from equilibrium and a decrease as the system moves towards equilibrium. All systems were then modelled in Simulink in preparation for analysis under different loading conditions.

Chapter 6: Semi-active Vibration Control via Boundary Conditioning

6.1 Overview

In this chapter, the performance of the control strategies presented in Chapter 5 to attenuate the vibration response of the MRE-based equivalent SDOF system are tested under different loading conditions. The goal is to demonstrate that control via boundary condition using MRE at the support is capable of attenuating vibration under different loading conditions while assuring that the MRE does not undergo large deformation.

Section 6.2 compares the transient response of the MRE-based SDOF system under a shock load using different control strategies. The shock transient response of the system is alternatively modelled using the free-vibration response under zero initial displacement and non-zero initial velocity. The initial velocity, however, should match that produced from, a unit impulse input. Section 6.3 compares the performance of the control strategies in attenuation of vibration amplitudes under harmonic loading at different input frequencies, specifically within the range of the fundamental frequency. Section 6.4 compares the time and frequency response to white noise input. The RMS displacement has been used to evaluate the vibration response of the system using different control strategies. Furthermore, a spectral analysis is performed to understand the behaviour of the system at different frequencies by comparing the PSDs obtained by FFT.

6.2 Shock (Free Vibration) Response

The response due to shock loads requires analysis in the time domain, as discussed in section 1.2.2.1. In order to improve structural health due to shock loads, then both peak amplitude and cycles of vibration should be decreased, since peak amplitude directly corresponds to stress magnitude, and frequency leads to fatigue failure. Therefore, the settling time and peak value due to shock loads must be decreased to improve structural integrity. Having a shorter settling time reduces the number of potentially damaging cycles, while a lower peak reduces the associated stress levels.

6.2.1 System Initialization

A shock, or impulse, response can be represented as a free vibration problem with zero initial displacement and non-zero initial velocity. The free vibration problem approach is favored over the impulse response when solving Duhamel's integral having the Dirac-delta function as the input force. The issue with using the Dirac-delta function is due to its definition being an applied force over an infinitesimally small period of time. Methods requiring discretization will not capture the effects of the Dirac-delta function since the discretization time step will always be larger than the time step for the impulse function, which approaches zero. Hence, controller design via NLP will not be able to capture the Dirac-delta function due to the discretization of the time domain. To some extent, Simulink may not be able to experience the Dirac-delta function for fixed time-steps. For model simulation in Simulink, it would be required to use variable time-stepping methods.

Since the free vibration response will be used rather than the unit impulse function, then it is necessary to determine an initial velocity that would make the two responses equal. The equivalent initial velocity for a unit impulse function can be determined from a momentum analysis, where the change in momentum is dependent on the impulse, $\hat{F}$, applied on the body, and is formulated as [85]:

$$\hat{F} = mv \tag{6-1}$$

Since the SDOF system has an equivalent mass of 6.6 g, and considering a unit impulse load where $\hat{F} = 1$, this means that the initial velocity is 152 m/s. Such a high velocity causes a large displacement on the first peak; therefore, a lower initial velocity magnitude is required to prevent large shear strain amplitude in the MREs. Figure 6-1 shows the trend of how the peak displacement depends on the initial velocity, therefore, an initial velocity of 1 m/s will be used moving forward to prevent large shear strain amplitude on the MRE. It is noted that the objective here is to assess the performance of different controllers to attenuate free vibration (representing shock response) response under initial velocity and the amount of initial velocity would not affect the outcome of the assessment.
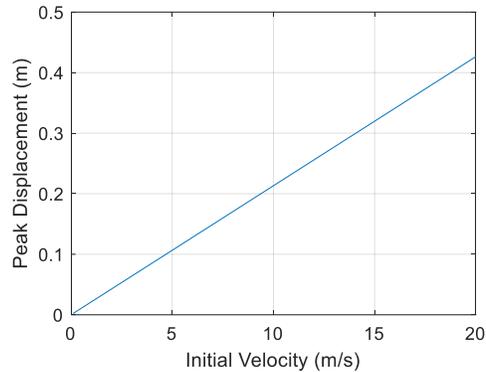
Figure 6-1: Peak Displacement vs Initial Velocity on Passive System

6.2.2   Results and Discussion

Under an initial velocity of 1 m/s and zero initial displacement, each controller is tested to validate their capabilities in decreasing both settling time and peak value. The NLP controllers are first examined to see the effects of different controllers derived from using different cost weights in the optimization problem presented in section 5.3. Similarly, the tuning parameters for three different PID controllers are determined from the corresponding optimization problem in section 5.4 and their performance are compared to see which provides the best results. Finally, the best performing NLP and PID controllers are compared to the passive and on-off controller to examine which of all controllers considered provides the best vibration attenuation.

The performance characteristics, as defined in section 1.2.2.1, can only be applied to the passive system as these definitions are only valid for LTI systems. Therefore, the stepinfo command in MATLAB will be used to measure the performance characteristics of the output signal of each controller. Because a shock load is of interest, both settling time and peak value are measured and considered in this analysis.

6.2.2.1   *Comparison of NLP Results*

Three different optimal controllers are developed using variations of the cost function in Eqn. (5-7). The first controller, NLP_{Ts}, minimizes the settling time while the second controller, NLP_X, minimizes the state energy, and the third controller, NLP_U, minimizes the input energy. Considering that the highest frequency attained is around 7 Hz, this would result in a period of about 0.14 seconds. To capture the physics as much as possible, a time step of 0.01 seconds (sampling frequency of 100 Hz) is used to discretize the period. This gives a total number of time

94

steps over the simulation time of 2.0 seconds to be 200. Essentially, a larger number of time steps would be ideal; however, having more discrete points increases the number of optimizer variables, thus requiring more computing power to converge to the true solution.

The settling time, input energy, and state energy associated with each controller are summarized in Table 6-1. The time response of the NLP controllers mentioned above along with the identified optimal input current are shown in Figure 6-2. Results show that the NLP_{Ts} indeed improves the settling time and that the NLP_X controller performs well in minimizing the state energy. The NLP_U controller maintains a zero input, thus being representative of the passive system with no input current. Comparison of the NLP_{Ts} and NLP_X controller shows that they may possibly be approaching towards the same solution. This could be since settling time minimization could also significantly lower the state energy since a smaller settling time would require less oscillations over a short period of time.

Table 6-1: Comparison of Time, State, and Energy Costs for Different NLP Controllers

Controller	Time Cost (s)	Input Energy Cost (J)	State Energy Cost (J)
NLP_{Ts}	0.809	8.25	3.30E−05
NLP_U	1.382	~0	4.84E−05
NLP_X	0.824	6.51	2.78E−05
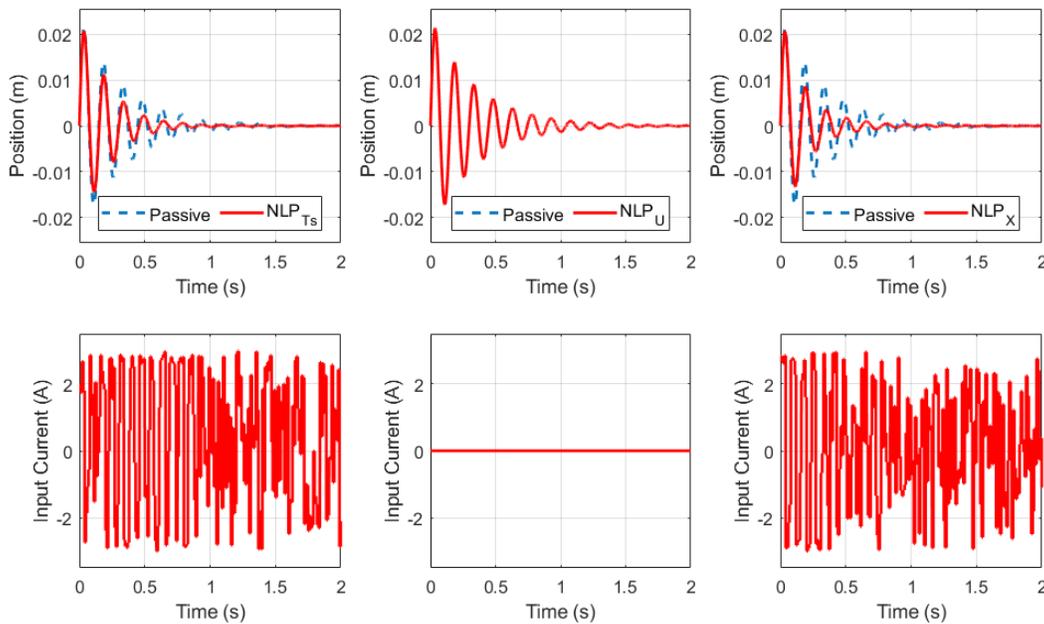
Figure 6-2: Time Response and Input for Different NLP Controllers

95

The input actuation obtained by NLP_{Ts} and NLP_X controllers are also compared to that obtained using on-off control as shown in Figure 6-3. It is interesting to note that both the NLP_{Ts} and NLP_X controllers tend to follow the pulses generated by the on-off controller, confirming that the on-off controller is indeed a time-optimal controller. Furthermore, the resulting time response of both NLP controllers looks similar to the response of the on-off controller. For further comparison, the on-off controller produces a settling time of 0.65 seconds with a state energy of 2.87E−05 J. Comparison with Table 6-1 suggests that both NLP_X and NLP_{Ts} controllers are tending towards having control laws similar to the on-off, as the optimization problem brings both settling time and state energies close to that of the on-off case. This may suggest that the on-off controller is a time-and-state-energy-optimal solution.
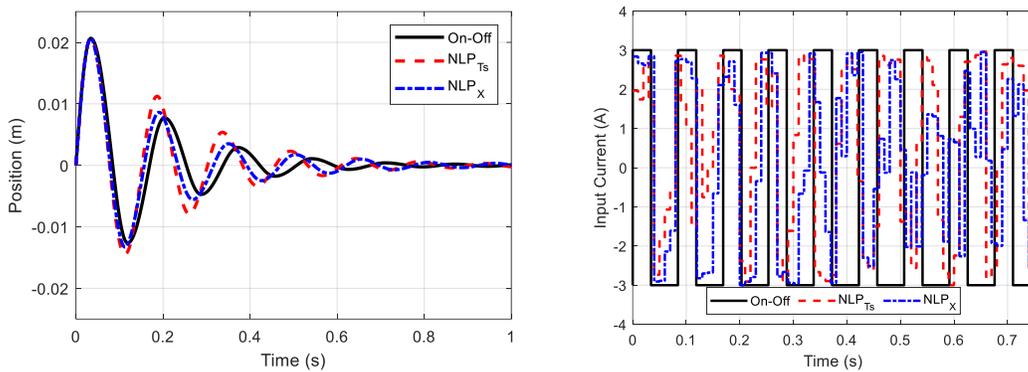
Figure 6-3: State and Control Comparison between NLP and On-Off Controllers

It would have been thought that the GA-SQP optimization algorithm find the global solution, which should have been the on-off controller. One main reason for the GA-SQP algorithm not being able to find the global solution is that there is a high number of optimizer variables, which increases the difficulty of finding a global solution. One way of increasing the chances of finding the global solution is by increasing the initial population size required by the genetic algorithm; however, increasing the population size requires more computational power thus becoming a limiting factor in determining the global solution.

Overall, the NLP_{Ts} controller provides the best vibration attenuation in terms of settling time while additionally providing a significantly low state energy. This is observed when comparing the optimized control law from NLP with that from the on-off case, where the two controllers are almost similar. The NLP_X controller is able to minimize state energy, however, the NLP_{Ts} controller also proves its capability of doing the nearly the same. The low state energy produced

96

by the NLP_{Ts} controller is most likely due to having less oscillations due to the lowered settling time.

6.2.2.2 Comparison of PID Tuning Results

The hybrid GA-SQP method was applied to solve the optimization problem using 5000 starting points because of the large range for the tuning parameters. Three PID controllers are developed based on the weight factors used. The PID_P controller minimizes the peak value, the PID_X minimizes the state energy, and PID_{Ts} minimizes the settling time. Table 6-2 provides the results of the optimization problem under different weight factors showing that the PID controller can effectively decrease the settling time or percent overshoot depending on the weight factor. Both PID_P and PID_X controllers are able to decrease the peak value by 2.8%; however, the settling time increases for both. The settling time for the PID_P controller increases by 32.1% while the PID_X controller increases the settling time by 1.7%. On the other hand, the PID_{Ts} controller is able to decrease the settling time by 3.1% while increasing the peak value by 8.5%. The most noticeable difference is in the control law, especially towards the end of the transient effects. This is shown in Figure 6-4 where the PID_{Ts} and PID_X controller tends toward a 3 A current input. According to Table 4-5, operation at a 3 A current provides the lowest settling time when compared to the −3 A current input. The reason why there is a lower settling time for the PID_{Ts} controller when compared to PID_X is that the latter controller spends more time having an input current of 3 A, thus having a settling time leaning towards the settling time of a passive system under an input current of 3 A, which is 1.56 seconds. The initial rippling effect on the input for the PID_{Ts} controller may attribute to the lower settling time when compared to PID_X; however, this rippling effect may also be the cause of the PID_{Ts} controller having more initial overshoot when compared to the other PID controllers. According to Figure 6-4, the PID_X and PID_{Ts} controllers behave almost alike shifting towards an input current of 3 A. This has the effect of stiffening the system due to the increase in magnetic flux density across the MRE, which ultimately causes a decrease in settling time.

Table 6-2: Summary of Performance Characteristics for PID Tuning Optimization Costs

Controller	K_P	K_I	K_D	Settling Time (s)		Peak (mm)	
				Value	% Change	Value	% Change
PID_P	26472	16178	−93056	1.823	+32.1%	20.7	−2.8%
PID_X	1169	−92175	−150	1.404	+1.7%	20.7	−2.8%
PID_{Ts}	35751	−89030	−1186	1.337	−3.1%	23.1	8.5%
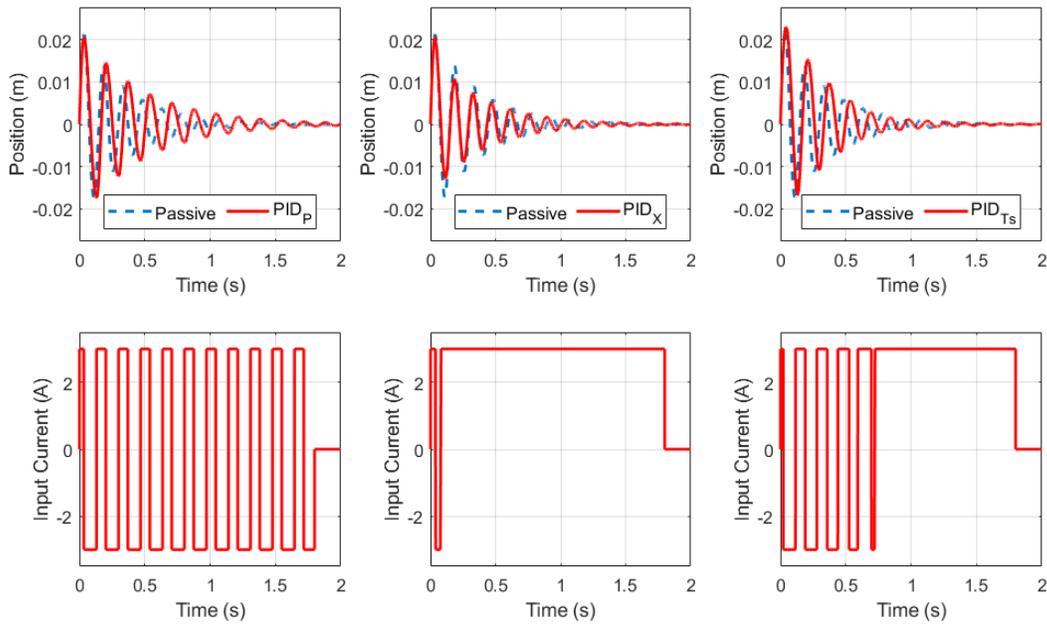
Figure 6-4: Comparison of Transient Response and Input Current between Passive and Different PID Systems

6.2.2.3 Comparison of Control Methods

The summary of the results for the settling time and peak response of the MRE-based equivalent SDOF system under shock response for different control methods are provided in Table 6-3. As a baseline for comparative purposes, the passive system performed with a settling time of 1.38 seconds and a peak value of 21.3 mm. Comparing all controllers show that the on-off controller performs the best with a settling time of 0.65 seconds and peak value of 20.7 mm. The NLP_{Ts} controller performs with a 0.80 second settling time and a peak value of 20.9 mm while the PID_{Ts} returned a settling time of 1.34 seconds and peak value of 23.1 mm. Figure 6-5 compares the time response and input current time history of the passive system with those of semi-active systems using PID_{Ts}, on-off, and NLP_{Ts} control strategies. The peak value of the PID-controlled system

tends to exceed that of the passive system since the controller is initially at 3 A, in which the percent overshoot is at 84.5% as opposed to the 80.7% for the passive system. It is interesting to notice how the settling time of the NLP_{Ts} system is close to that of the on-off, which is at a difference of 0.16 seconds, while the peak is almost the same. This again suggests that the NLP_{Ts} controller is approaching a control law similar to the on-off controller.

Overall, each controller type is capable of minimizing the settling time when comparing to the passive system. However, the peak value for the PID_{Ts}-controlled system is higher than the passive case, which is because the controller has an input value of 3 A during the first peak, resulting in a higher percent overshoot. The on-off, overall, is the better performer as it is capable of approximately halving the settling time while decreasing slightly the peak value.

Table 6-3: Settling Time and Peak Comparison

Method	Settling Time (s)	Peak (mm)
Passive	1.38	21.3
PID_{Ts}	1.34 (−3.3%)	23.1 (+8.4%)
On-Off	0.65 (−52.7%)	20.7 (−3.1%)
NLP_{Ts}	0.81 (−41.5%)	20.7 (−3.1%)
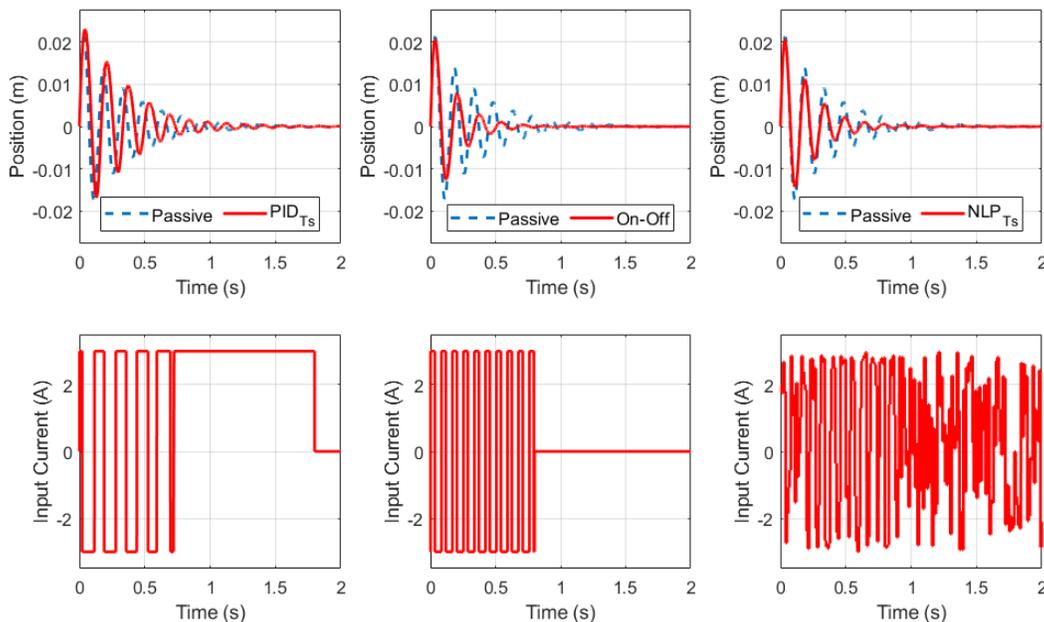
*Figure 6-5: Comparison of Transient Response and Input Current between Passive and Semi-active Systems due to different Control Strategies*

6.3 Harmonic Response

One crucial phenomenon that must be avoided in harmonically excited systems is that of resonance. Resonance causes the system to oscillate with increasing magnitude over time, which can quickly lead to structural failure. One interesting behavior for semi-active systems is that of resonance escape, where the system can shift its natural frequency away from the operating frequency to avoid catastrophic failure. Resonance escape can be achieved through adaptive semi-active control, which allows the system to oscillate at safer amplitudes.

6.3.1 System Initialization

The harmonic response of the MRE-based SDOF system is obtained under a harmonic load having an amplitude of 0.01 N to assure that the MRE operates under small shear strain. Figure 4-18(a) shows a maximum transfer function amplitude of 0.961 m/N for an input current of −3 A. Therefore, a force amplitude of 0.01 N will result in a maximum displacement amplitude of 9.61 mm. From the previous transient analysis due to shock loading in section 6.2.2.3, the maximum tip displacement was 23.1 mm, which satisfied the limit on shear strain on the MRE. Therefore, for a load of 0.01 N, all subsequent analyses should also satisfy the limitation on the shear strain.

To ensure proper steady-state results, a simulation time of 10 seconds is used in order to ensure that all transient effects due to initial conditions have decayed and that the response will be purely due to the harmonic load. The system will be tested for operating frequencies of 5.14 Hz, 6.74 Hz, and 7.06 Hz, which represent the natural frequencies when using an input current of −3, 0, and 3 A, respectively. The purpose of this section is to demonstrate the capability of the adaptive system to escape resonance. To understand the behavior of these semi-active systems, it is important to note how changes in the input current can shift the natural frequency either towards or away from the input frequency. This behavior has a strong impact on the steady-state vibration response due to harmonic loading and will be discussed in detail.

6.3.2 Results and Discussion

The goal of this section is to validate the effectiveness of resonance escape. Different controllers will provide different means of attenuating vibration; however, the key is to have a natural frequency different from the input frequency. In this case, it is only necessary for NLP to provide a controller that can minimize state energy, as this has a direct impact on the steady-state response. The PID controllers derived from section 6.2.2.2 are compared for their effectiveness in

dampening the steady-state vibration. A comparison of all controllers is conducted to see which can provide the best attenuation over the frequency range of 5.14 Hz to 7.06 Hz, which is the full range of the natural frequency.

For each controller, the results are obtained by running the system for 10 seconds such that the transient effects due to initial conditions dissipate, leaving only the steady-state response. A timeframe of 1 second at the end of the simulation, from 9 to 10 seconds, is used to analyze the steady-state response by measuring the maximum displacement in that timeframe. This, again, is assuming that there are no transient effects occurring during that 1 second timeframe at the end of the simulation.

6.3.2.1 Comparison of PID Tuning Results

The three different PID controllers presented in section 6.2.2.2 are used to see their capabilities in attenuating vibration due to harmonic loads. Table 6-4 gives the summary of results of the steady-state amplitudes due to each controller when operating under different input frequencies. Figure 6-6, Figure 6-7, and Figure 6-8 show the steady-state behavior of the different PID controllers compared to the passive system at input frequencies of 5.14 Hz, 6.74 Hz, and 7.06 Hz, respectively. Figure 6-9, Figure 6-10, and Figure 6-11 show the complete solution of each PID controller.

Interestingly, the PID_{TS} controller shows good attenuation for lower input frequency but shows poor attenuation at higher frequencies. Furthermore, Figure 6-10 and Figure 6-11 show that the PID_{TS} controller does not appear to reach steady-state since the system is continually increasing in amplitude. The resulting data in Table 6-4 are measured data at the end of the simulation, the asterisk (*) signifying that the solution has not reached steady state. The PID_X controller shows good attenuation at lower frequencies, while the PID_P causes amplification. The opposite can be said at higher frequencies, where the PID_P attenuates vibration while the PID_X amplifies. The PID_P controller amplifies when operating at 5.14 Hz since it spends more time having an input current of -3 A, causing the system to have a natural frequency matching the input frequency. On the other hand, the PID_X controller amplifies at 7.06 Hz since the controller dwells on an input current of 3 A, again, causing a match in natural and input frequency.

It would be beneficial to adjust the PID controller to attenuate vibration under all input frequencies. Such adjustment can be done through gain scheduling, where the PID gains can be

controlled based on some logic. For example, the PID gains would use that of the PID_X controller at low input frequencies and then use the PID_P controller gains at high input frequencies. For the purpose of this study, the PID_X controller will be used moving forward as this provides the least amount of amplification across all input frequencies. The PID_P controller shows amplification of two times that of the passive case at 5.14 Hz.

Table 6-4: Amplitude Comparison under Harmonic Input for Different PID Tuning Parameters

Controller	Steady-State Amplitude (mm)		
	5.14 Hz	6.74 Hz	7.06 Hz
PID_P	3.96	1.59	1.59
PID_X	3.59	5.19	4.85
PID_{Ts}	2.61	6.50*	4.25*
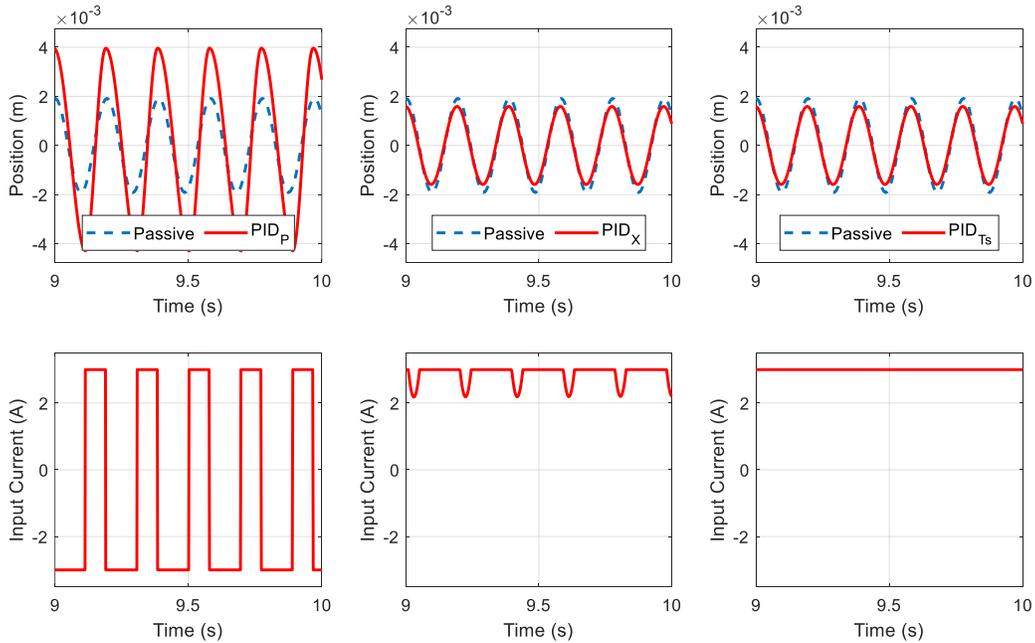
Figure 6-6: Steady-State Time Response and Control Current for PID Controllers under Harmonic Input at 5.14 Hz
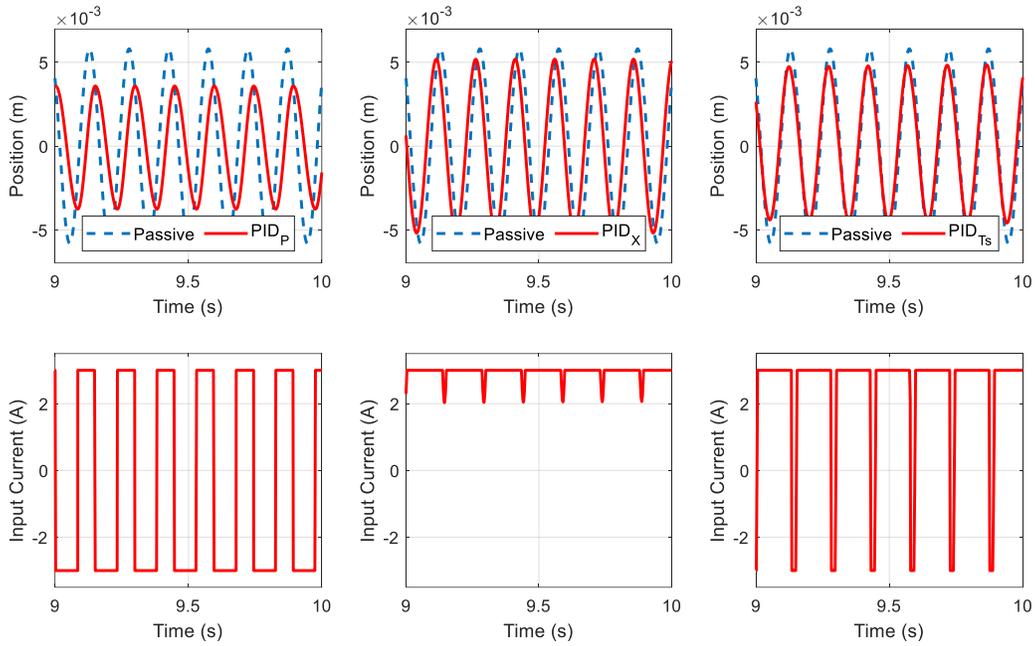
Figure 6-7: Steady-State Time Response and Control Current for PID Controllers under Harmonic Input at 6.74 Hz
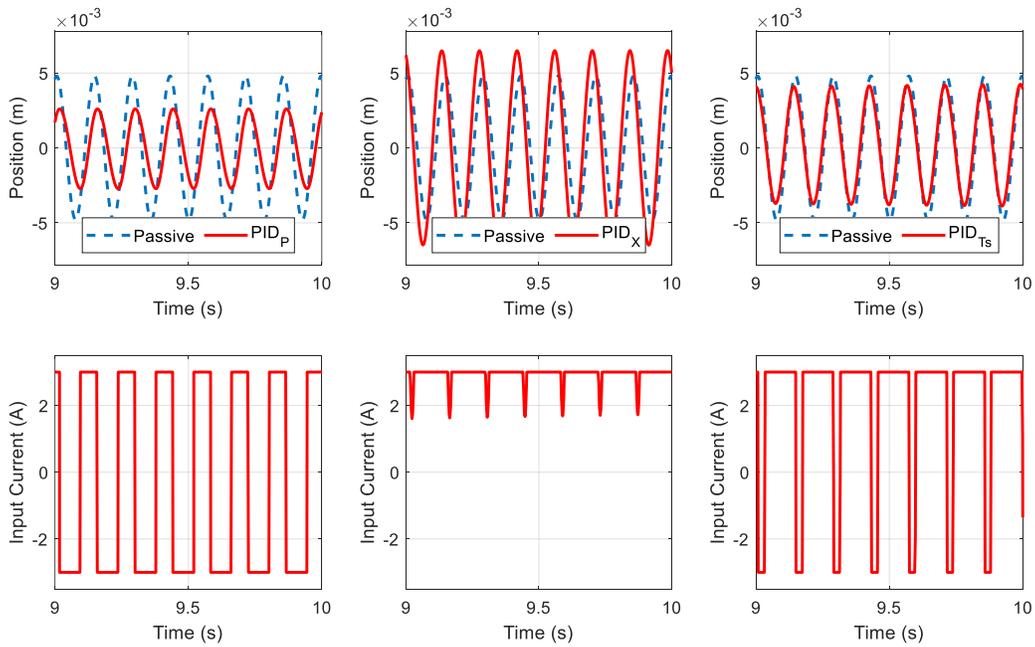

Figure 6-8: Steady-State Time Response and Control Current for PID Controllers under Harmonic Input at 7.06 Hz

103
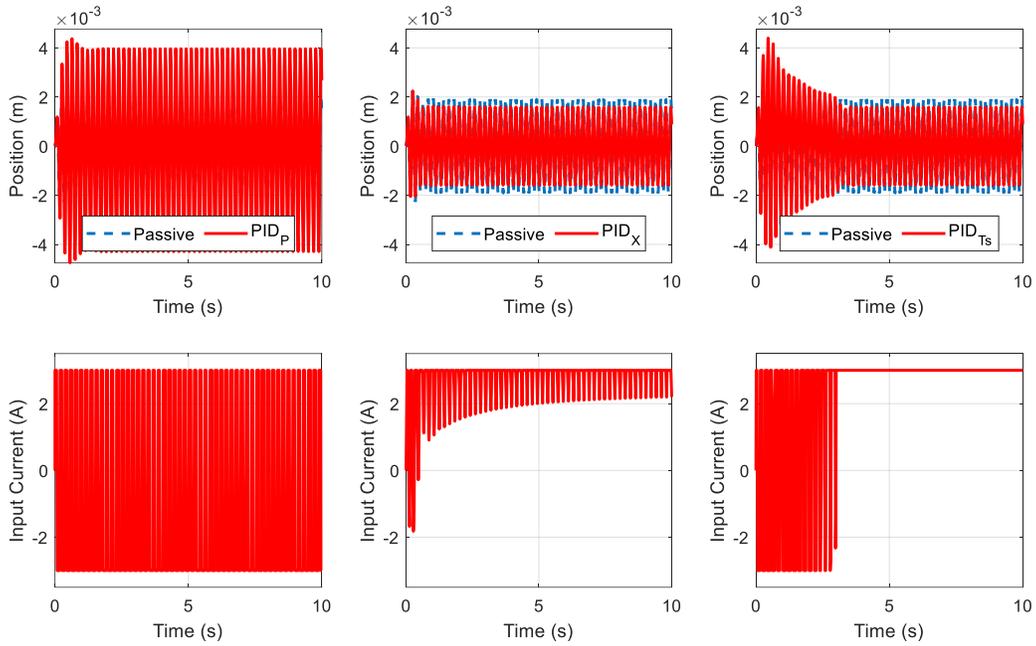
Figure 6-9: Complete Time Response and Control Current for PID Controllers under Harmonic Input at 5.14 Hz
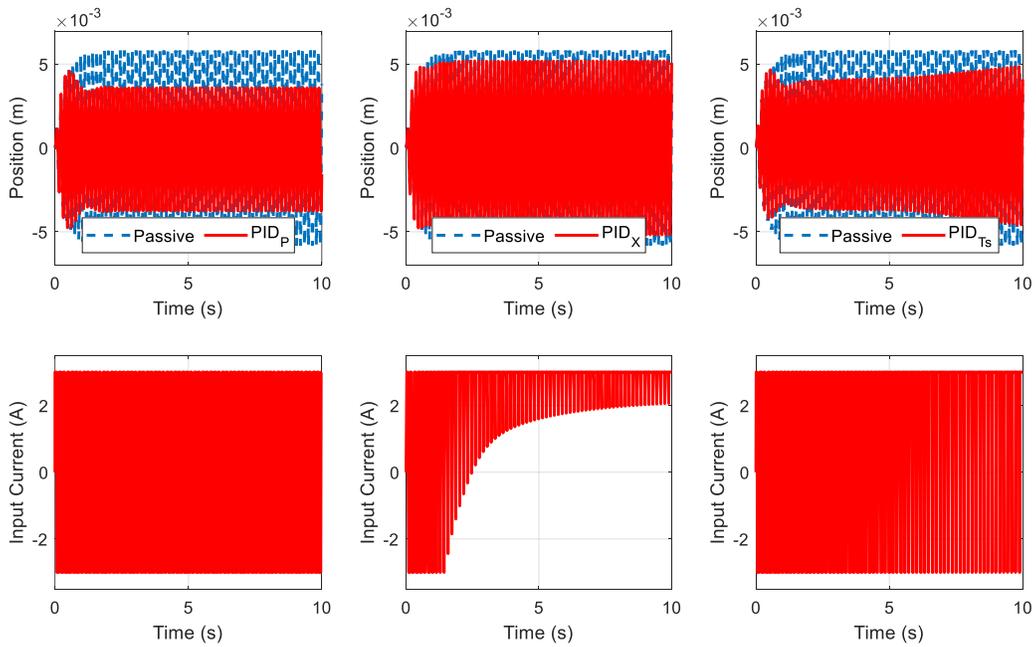

Figure 6-10: Complete Time Response and Control Current for PID Controllers under Harmonic Input at 6.74 Hz

104
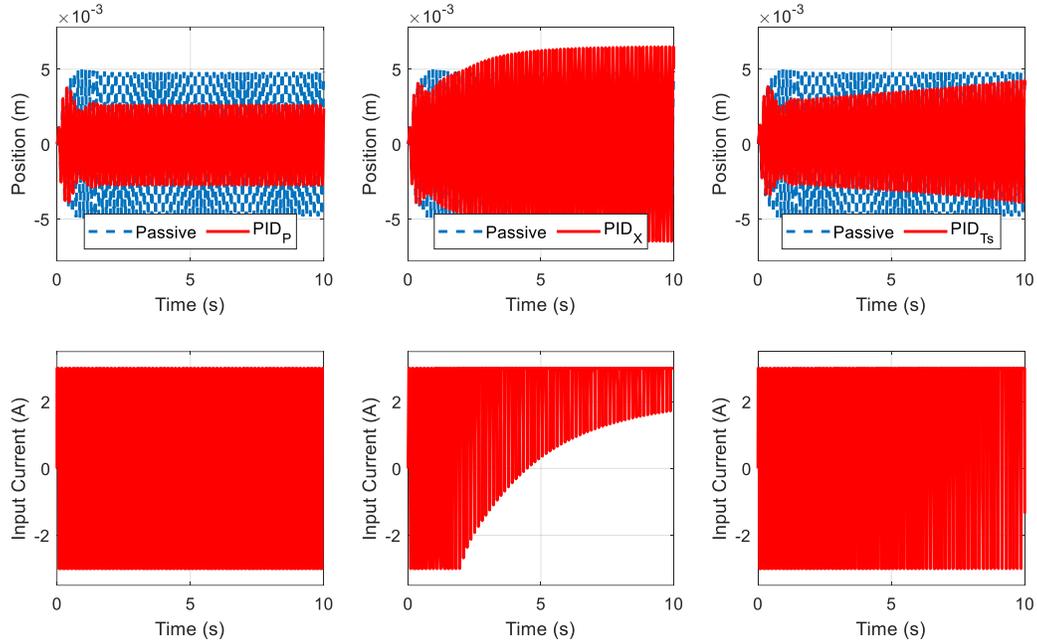
Figure 6-11: Complete Time Response and Control Current for PID Controllers under Harmonic Input at 7.06 Hz

6.3.2.2 Comparison of Control Methods

In the case of harmonic loads, vibration attenuation is achieved by lowering the steady-state amplitude. For the offline optimization control due to NLP methods, the NLP_X control strategy is preferred since it is based on minimizing the state energy, which is required to dampen the steady-state amplitude of vibration. Results for the total harmonic response and control current under harmonic force with excitation frequencies set at 5.14 Hz, 6.74 Hz, and 7.06 Hz are shown in Figure 6-12, Figure 6-13, and Figure 6-14, respectively. Figure 6-15, Figure 6-16, and Figure 6-17, show only the steady-state response for the same excitation frequencies. The steady-state amplitudes are summarized in Table 6-5.

At an input frequency of 5.14 Hz, the PID_X shows the best attenuation compared to the other two controllers with a 17.0% decrease in vibration amplitude. Figure 6-15 shows that, at steady-state, the PID_X controller remains at 3 A, which causes the system to have a natural frequency to be safely away from the input frequency. The NLP_X controller performs well with a steady-state amplitude reduction of 4.5%. A histogram of the NLP_X controller under different operating frequencies is shown in Figure 6-18. For the operating frequency of 5.14 Hz (natural frequency at $I = -3$ A), the NLP_X controller puts more weight on having input currents between 0 and 3 A to

105

avoid resonance. The on-off controller causes amplification to give a steady-state amplitude increase of 25.0% when compared to the passive system. The on-off spends time having a natural frequency equal to the input frequency since the controller is limited to −3 and 3 A.

At 6.74 Hz, the on-off outperforms the other two controllers, having an attenuated steady-state amplitude, having a decrease of 55.3%. Reason being because the on-off controller will never have a natural frequency close to the input frequency since the input current can never reach 0 A. The NLP_X controller also has good comparable vibration response having a decrease in steady-state amplitude of 16.6%, since the optimal controller puts more weight towards lower input current, as shown in Figure 6-18. The PID_X controller still decreases the steady-state amplitude since having an input current of 3 A causes the natural frequency to be different that the input frequency. Under these conditions, the PID_X controller is capable of decreasing the steady-state amplitude by 10.6%.

For the input frequency of 7.06 Hz, the on-off controller provides the best attenuation at a decrease of 54.4%. Interestingly, although the system does spend time having a natural frequency equal to the input frequency when at 3 A, there is still good attenuation unlike when operating at 4.67 Hz. Figure 4-19 suggests that amplification is far worse at −3 A than at 3 A, hence the effects of attenuation at −3 A outweigh the amplification at 3 A when operating at 7.06 Hz. In Figure 6-18, the NLP_X controller tends to lower input currents which causes good attenuation, having a decrease in amplitude of 26.7%. The histogram in Figure 6-18 demonstrates that the controller tends to lower values of input current to avoid having a natural frequency close to the operating frequency. The PID_X amplifies the vibration by 35.3% because the input current of 3 A causes the natural frequency to match the input frequency, thus causing resonance. As explained in section 6.3.2.1, this issue can be mitigated by gain scheduling, where the PID_P gains can be used when operating at a frequency of 7.06 Hz.

Overall, the on-off controller provides safe vibrations for all input frequencies except when operating at lowest frequency of 5.14 Hz. The PID_X controller can provide good attenuation at all frequencies except at 7.06 Hz. The NLP_X controller sheds light to a possible type of optimal controller when dealing with harmonic inputs. Because of the number of discrete points used in the optimization problem, then there will be difficulty in converging to the global optimal solution. However, it seems that the NLP_X controller wants to select an input current that drives the natural frequency away from the input frequency. It could be that an optimal solution would be to operate

at a constant input current such that the system would be passive at a specific current with a natural frequency far from the input frequency.

Table 6-5: Amplitude Comparison under Harmonic Input

Controller	Steady-State Amplitude (mm)		
	5.14 Hz	6.74 Hz	7.06 Hz
Passive	1.9	5.8	4.8
PID	1.6 (−17.0%)	5.2 (−10.6%)	6.5 (+35.3%)
On-Off	2.4 (+25.0%)	2.6 (−55.3%)	2.2 (−54.4%)
NLP	1.8 (−4.5%)	4.8 (−16.6%)	3.5 (−26.7%)
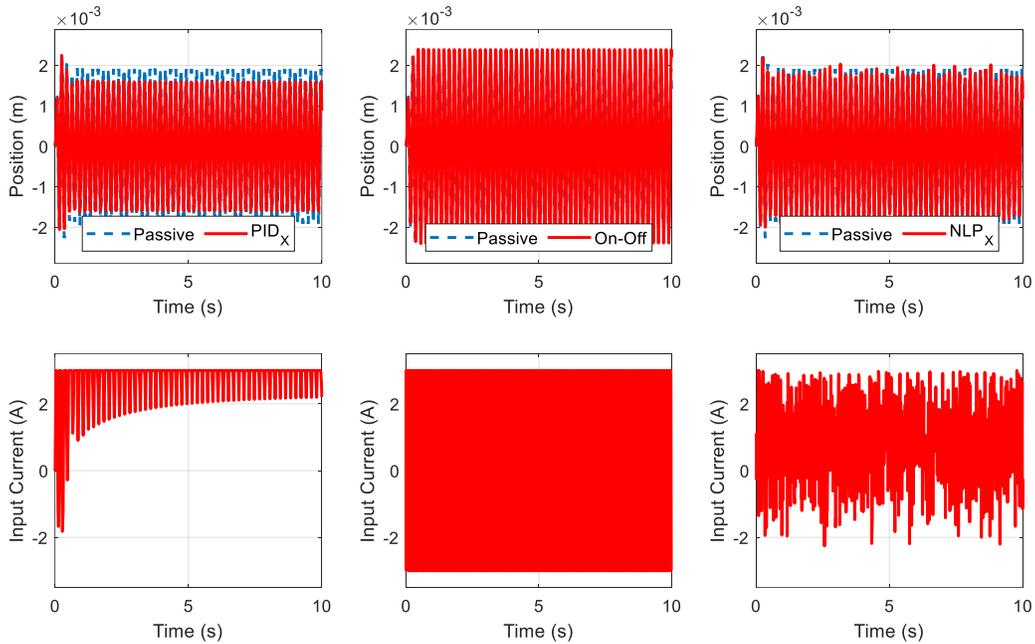
Figure 6-12: Complete Time Response and Control Current for Different Controllers under Harmonic Input at 5.14 Hz
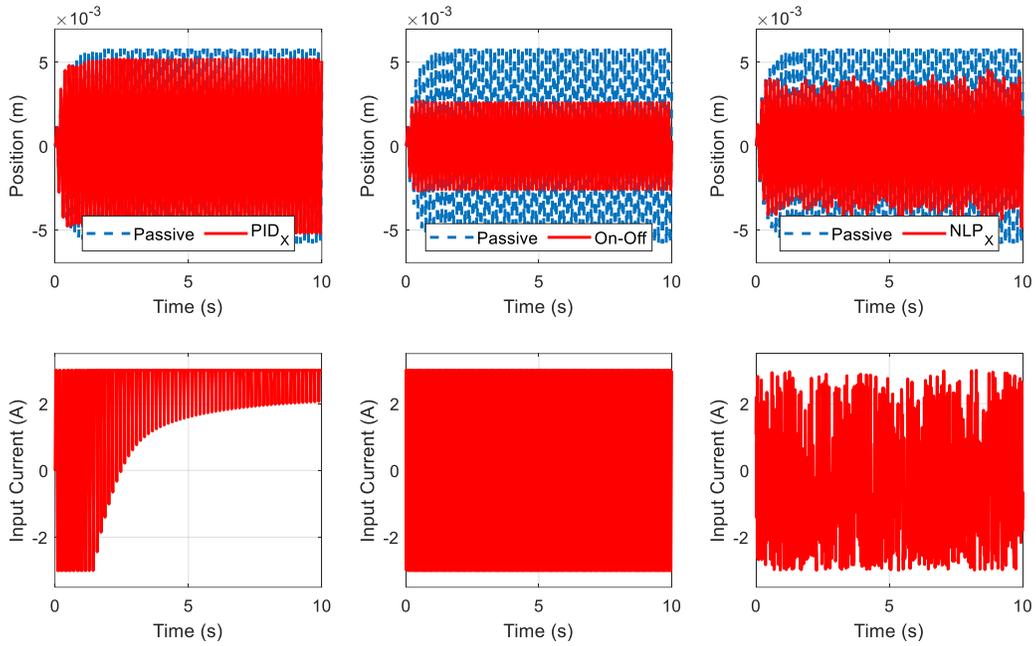
Figure 6-13: Complete Time Response and Control Current for Different Controllers under Harmonic Input at 6.74 Hz
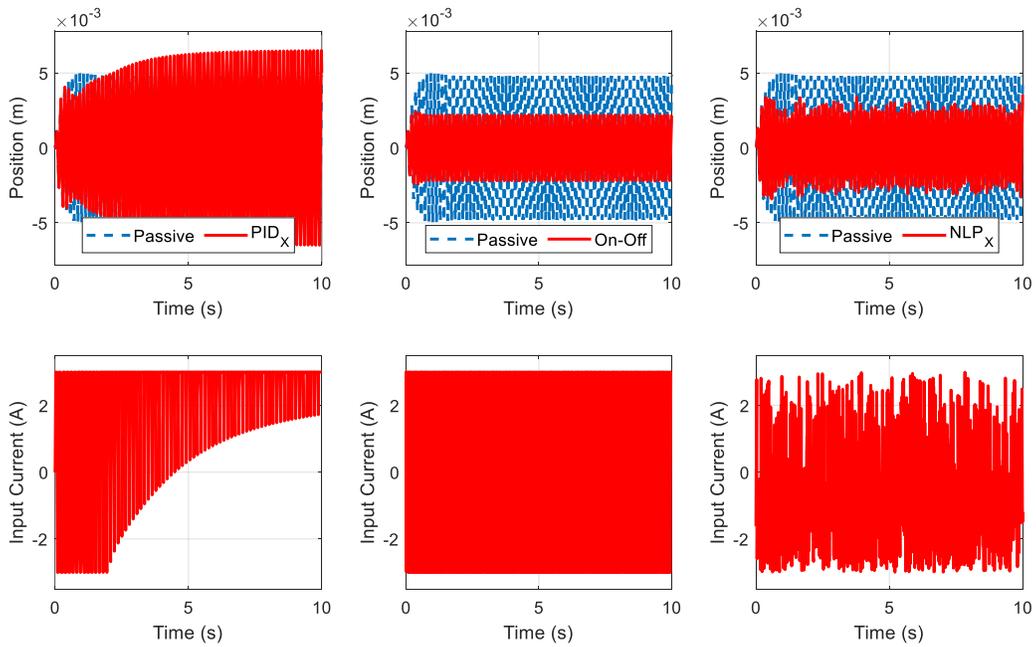
Figure 6-14: Complete Time Response and Control Current for Different Controllers under Harmonic Input at 7.06 Hz

108
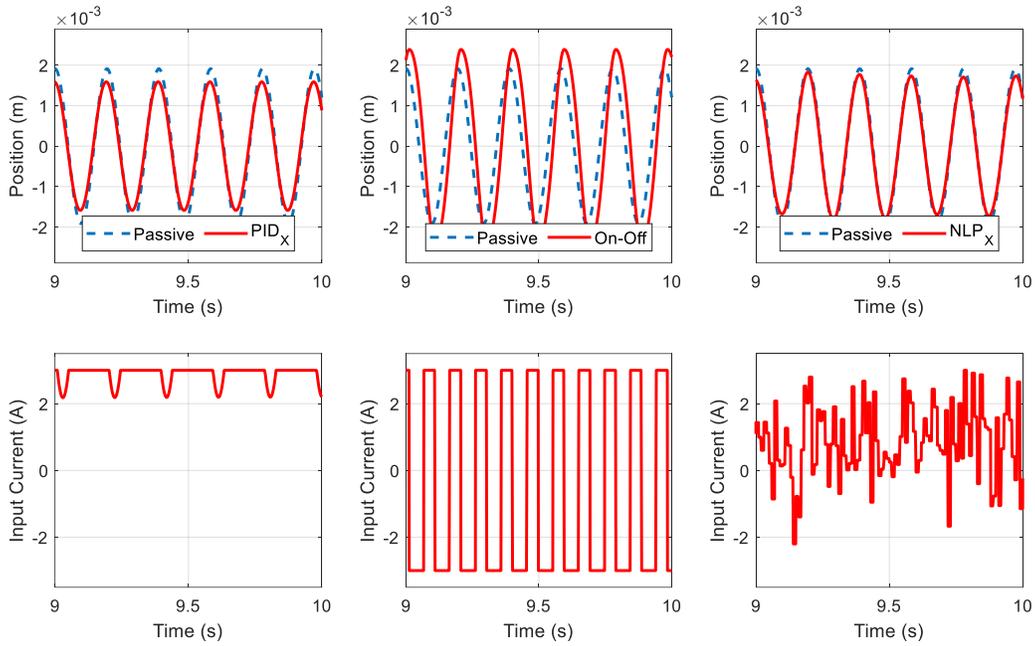
Figure 6-15: Steady-State Time Response and Control Current for Different Controllers under Harmonic Input at 5.14 Hz
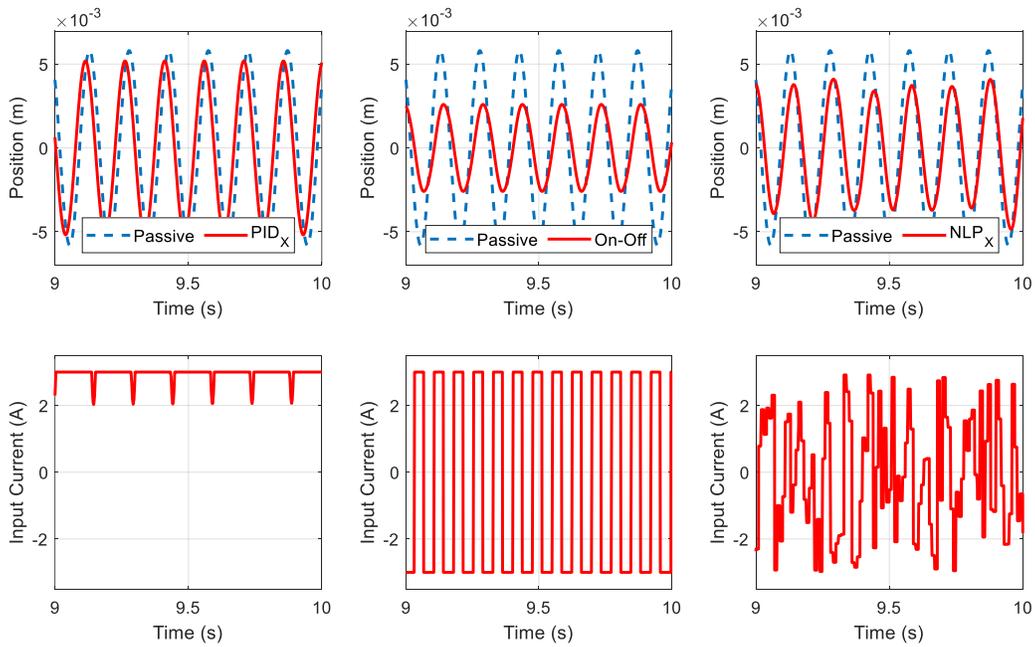
Figure 6-16: Steady-State Time Response and Control Current for Different Controllers under Harmonic Input at 6.74 Hz

109
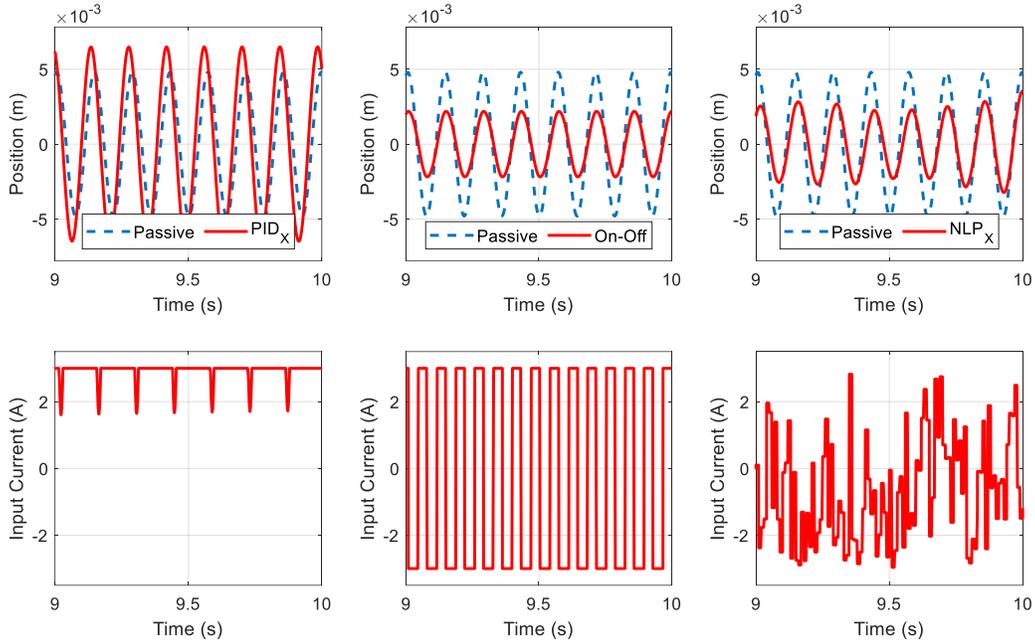
Figure 6-17: Steady-State Time Response and Control Current for Different Controllers under Harmonic Input at 7.06 Hz
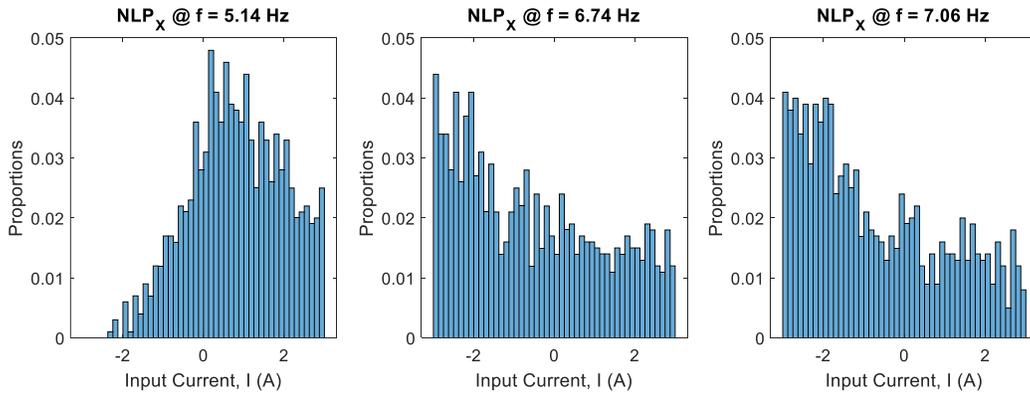
Figure 6-18: Histogram of NLP$_X$ Controller under Different Operating Frequencies

6.4 Random Vibration Response

Being non-deterministic, random loads and their response must be treated using statistical methods. In the time domain, both mean and standard deviation in the displacement are measured to shed light on the statistical behavior of the system. In the frequency domain, a spectral analysis is done to understand what bandwidth of frequencies gives a significant amount of power to the system to cause harsh vibrations. Normally the PSD of the displacement response is obtained analytically through Eqn. (1-25); however, because the transfer function cannot be obtained for

110

LTV systems, then the FFT method is used. The FFT method is performed directly in Simulink, which has built-in features of obtaining the PSD.

6.4.1   System Initialization

The performance of control strategies to attenuate vibration under white noise load has been investigated. The band-limited white noise block in Simulink is used to simulate a white noise input with a power of 1 mW. The suggested sampling rate is:

$$t_{sample} = \frac{2\pi}{100\omega} \qquad\qquad (6\text{-}2)$$

when using the band-limited white noise block in Simulink [86]. Since the highest natural frequency of the system is 7.04 Hz, this gives a sampling time of around 1 ms, or a sampling rate of around 1 kHz. A sampling rate of 10 kHz is used to ensure good representation of white noise. Note that NLP was not applied for the random input case. A runtime of 500 seconds is used to measure a proper mean and standard deviation since more data points is retrieved. This would require at least 5 million control points in order to capture the time response using NLP. This would require more computing power; therefore, NLP was not possible due to this limitation.

Normally, the power spectral density can be obtained through Eqn. (1-25), which requires the transfer function. However, due to the complexity of obtaining the transfer function for an LTV system, FFT was used to obtain the PSD. In Simulink, this can be achieved by using the spectral analyzer block. The spectral analyzer block requires that the incoming signal be discrete, therefore, as seen in Figure 6-19, the output signal is first sent to a zero-order hold block to convert the continuous signal to a discrete one.
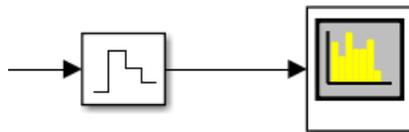
Figure 6-19: Simulink Setup to Measure Power Spectral Density

For a non-deterministic system, the transient response is defined by its mean and RMS displacement. Assuming zero-mean, then the RMS response can be defined by its transfer function and the power spectral density for white noise. Again, the issue with applying Eqn. (1-27) is that

the transfer function cannot be obtained for LTV systems. Alternatively for white noise, the mean-square response for a force-excited passive system is approximated by [26]:

$$\sigma_X^2 = \frac{0.785 f_n W_0}{\zeta k^2} \tag{6-3}$$

Using the above equation for the passive system with a white noise power of 1 mW would give a root-mean-square (RMS) response of 23.5 mm. This result differs from the measured output of 33.2 mm for the passive system. Generally, the power spectral density of white noise is constant at all frequencies; in other words, the PSD is flat with a power at W_0. However, the spectral density of the band-limited white noise block in MATLAB outputs fluctuations in magnitudes across the range in frequencies, as shown in Figure 6-20. These fluctuations may be the cause in the difference between the theoretical and measured RMS value of the displacement. Under these circumstances, both mean and standard deviation of the mass displacement are measured directly from the output signal.
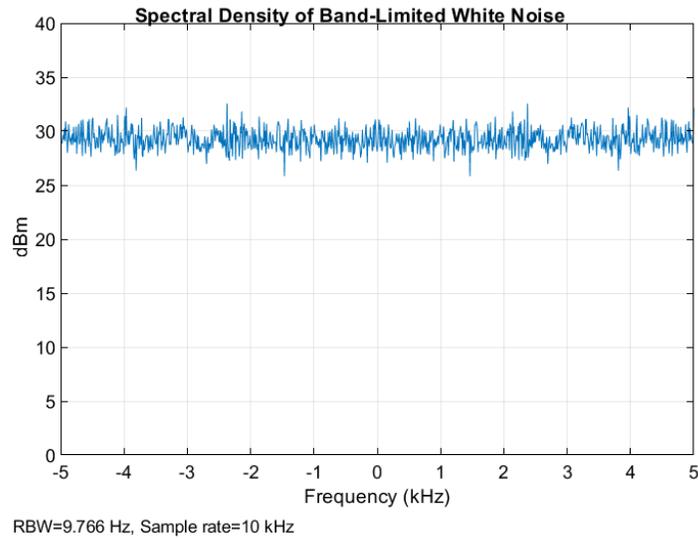
Figure 6-20: Spectral Density of Band-Limited White Noise Simulink Block

6.4.2   Results and Discussion

To improve the structural integrity under random loads, then the RMS displacement is the parameter of interest as this has a direct impact on the stress levels. Therefore, attenuation of the RMS displacement must be achieved by the different controllers. Firstly, the PID controllers derived in section 6.2.2.2 are tested to see their capabilities in lowering the RMS displacement. Again, all controllers are compared to see which of them provides the best results. Note that the

NLP controller is not implemented due to the number of control points required to obtain a solution, which would require high computational power.

In order to have good confidence on the statistical results, a longer sampling time is required. A longer sampling time is also beneficial when performing FFT as this will provide better confidence on the corresponding PSD. For the time response, the mean and standard deviation was measured directly from the output signal of each controller. The PSD was obtained through the spectral analyzer block in Simulink, which applies the FFT method.

6.4.2.1 Comparison of PID Tuning Results

Similar behavior as discussed in the previous two sections regarding the PID tuning parameters can also be seen when under the influence of random loads. Table 6-6 shows how the PID_{Ts} and PID_X system performs almost equally well, both having a low RMS displacement value. The PID_P has a higher RMS displacement value compared to the other two PID controllers. As shown in Figure 6-23, this is due to the PID_P system dwelling on an input current of -3 A, which induces the worst amplification as discussed in section 4.6.2. Figure 6-21 and Figure 6-22 show the time response and PSD of each PID-controlled system, respectively. The histogram in Figure 6-23 also shows that the PID_{Ts} and PID_X systems have a tendency to dwell on an input current of 3 A, which causes a stiffening of the MRE thus hindering motion. Because of the tendency of the PID_{Ts} and PID_X controllers to dwell on an input current of 3 A, this causes a higher power density in the power spectral density of systems. Overall, the PID_{Ts} controller is preferred as it provides the lowest RMS displacement.

Table 6-6: Time and Spectral Response for Random Input for Different PID Tuning Parameters

Controller	**Time Response**		**Spectral Response**		
	Mean Displacement (mm)	RMS Displacement (mm)	Max Power Density Frequency (Hz)	Max Power Density (mW/Hz)	Bandwidth (Hz)
PID_P	-0.7	45.3	5.93	1.765	5.46 – 6.80
PID_X	0.0	34.0	7.40	2.349	6.60 – 7.40
PID_{Ts}	0.2	33.2	7.40	2.322	6.60 – 7.40
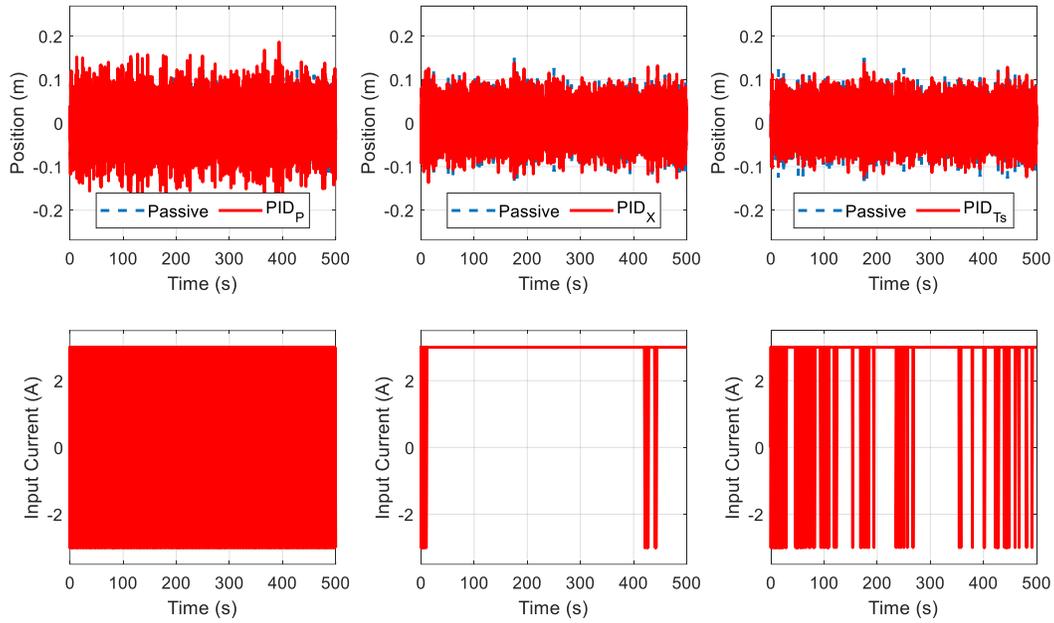
Figure 6-21: Time Response and Controller Input for Random Input for Different PID Tuning Parameters
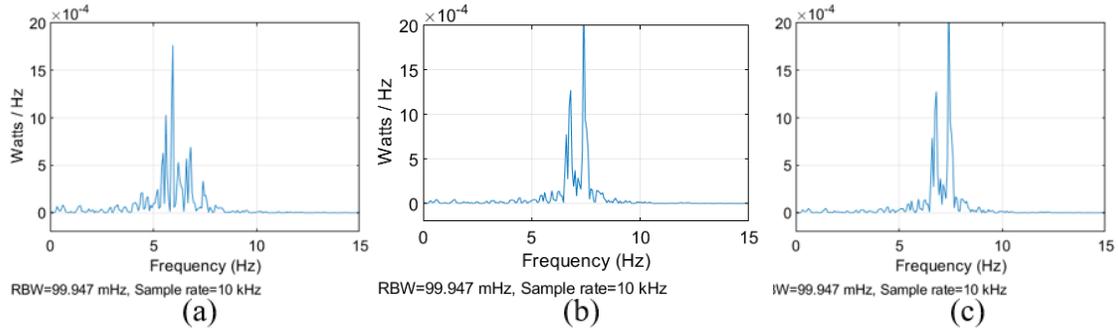
Figure 6-22: PSD for PID$_P$ (a), PID$_M$ (b), and PID$_{Ts}$ Systems subject to White Noise
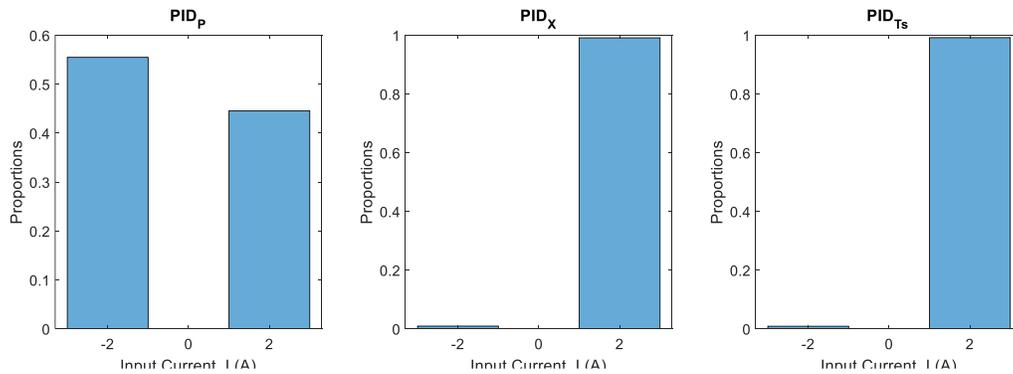
Figure 6-23: Histogram of Different PID Controllers subject to White Noise

114

6.4.2.2 Comparison of Control Methods

Summary of the random vibration response can be found in Table 6-7, which includes both time and frequency response. Figure 6-24 and Figure 6-25 show the time response over a time interval of 500 seconds and 50 seconds, respectively. Visualizing the input current over a smaller interval helps in understanding the behavior of the different controllers. Validation of Eqn. (1-27) requires that the mean displacement be approximately zero, which has been verified for each control case. Comparison of the different controllers shows that the on-off controller is better at attenuating the RMS displacement by 23.5%. The PID_{Ts} controller has almost no change in RMS displacement compared to the passive case, which may be due to the PID_{Ts}-controlled system having a controller input of 3 A for a significant amount of time, as shown in Figure 6-25. The histogram in Figure 6-27 shows the same trend, where the controller spends almost 100% of its time at 3 A. This may cause some overshooting from time to time for the PID_{Ts} system, which may be the underlying factor as to why there are no improvements to the RMS displacement. Although the on-off controller is capable of good vibration suppression, the control input for the on-off controller shown in Figure 6-24 and Figure 6-25 is subject to chatter [87]. In context, this would mean that there would be a high amount of switchings between the on and off state over a short period of time.

Table 6-7: Mean and RMS Response for Random Input

Controller	Time Response		Spectral Response		
	Mean Displacement (mm)	RMS Displacement (mm)	Max Power Density Frequency (Hz)	Max Power Density (mW/Hz)	Bandwidth (Hz)
Passive	0.0	33.2	6.80	1.553	6.60 – 7.40
PID$_{Ts}$	0.2	33.2 (0%)	7.13	2.144	6.00 – 7.53
On-Off	0.1	25.4 (−23.5%)	6.26	0.455	4.60 – 6.73
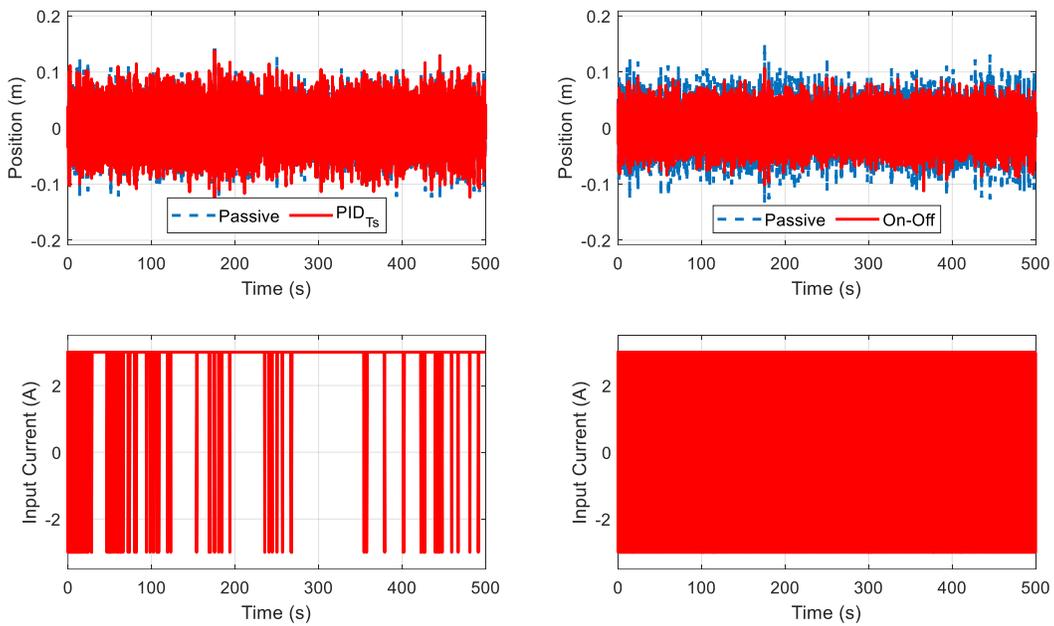
Figure 6-24: Time Response and Controller Input for Random Input over 500 Seconds
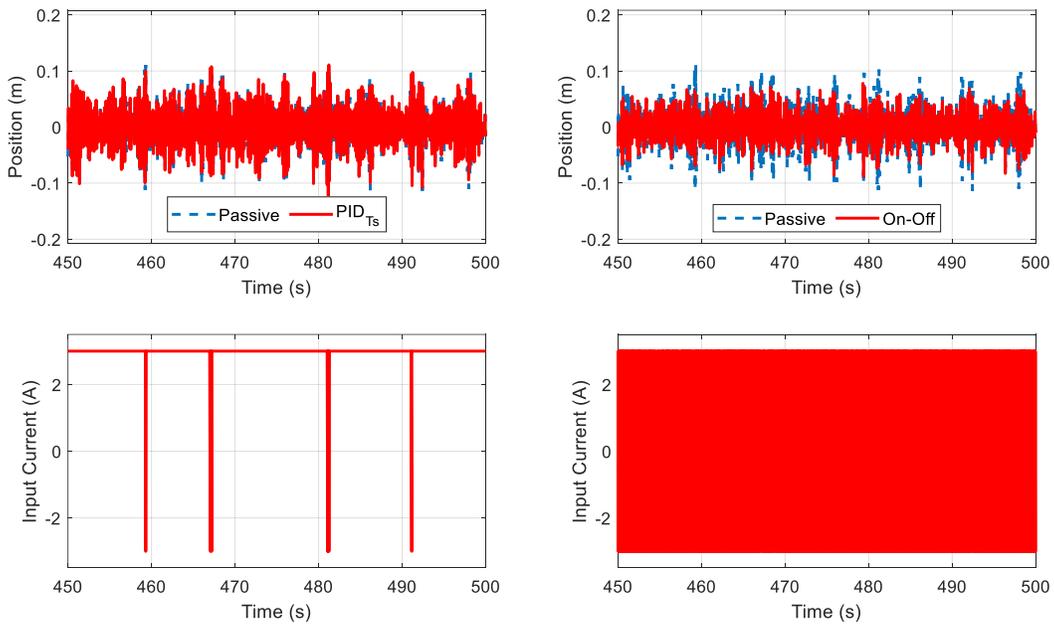
Figure 6-25: Time Response and Controller Input for Random Input over 50 Seconds

In order to capture a good power spectral density for each system, the simulation was conducted for a total of 500 seconds such that there is a large number of samples for FFT. The PSD for the passive, PID_{Ts}, and on-off systems are shown in Figure 6-26. The PSD for the passive

116

system shows a highest response at a frequency of around 6.80 Hz. This is expected since the fundamental frequency for the passive system with an input current of 0 A is 6.74 Hz. Furthermore, the bandwidth ranges from approximately 6.60 to 7.40 Hz, which bound the natural frequency of 6.74 Hz. The PSD for the PID_{TS} system shows a maximum response for a frequency of 7.13 Hz with a bandwidth of around 6.00 to 7.53 Hz. The PID_{TS} system tends to amplify at higher frequencies approaching 7.13 Hz since more time is spent having a natural frequency of 7.06 Hz due to the 3 A input. This trend can be seen in Figure 6-25 and Figure 6-27 where the input of the PID system spends more time at 3 A, making up about 98% of the total time. This behavior also affects the bandwidth being at a higher range of frequencies. The PSD of the on-off controller shows peak excitation at around 6.26 Hz; however, this peak is comparably much lower than those from the passive and PID_{TS} systems. The associated bandwidth is roughly between 4.60 to 6.73 Hz, which is almost the full range of the frequency shift being from 5.14 to 7.06 Hz. The percentage of time of having an input of 3 A over the total simulation time is measured to be 49%. Therefore, the controller spends half the time having a natural frequency of 5.14 Hz and the other half at 7.06 Hz. This behavior can explain why the bandwidth for the on-off controller is much wider with very low power due to a possible distribution of power across the frequencies.

RBW=99.947 mHz, Sample rate=10 kHz
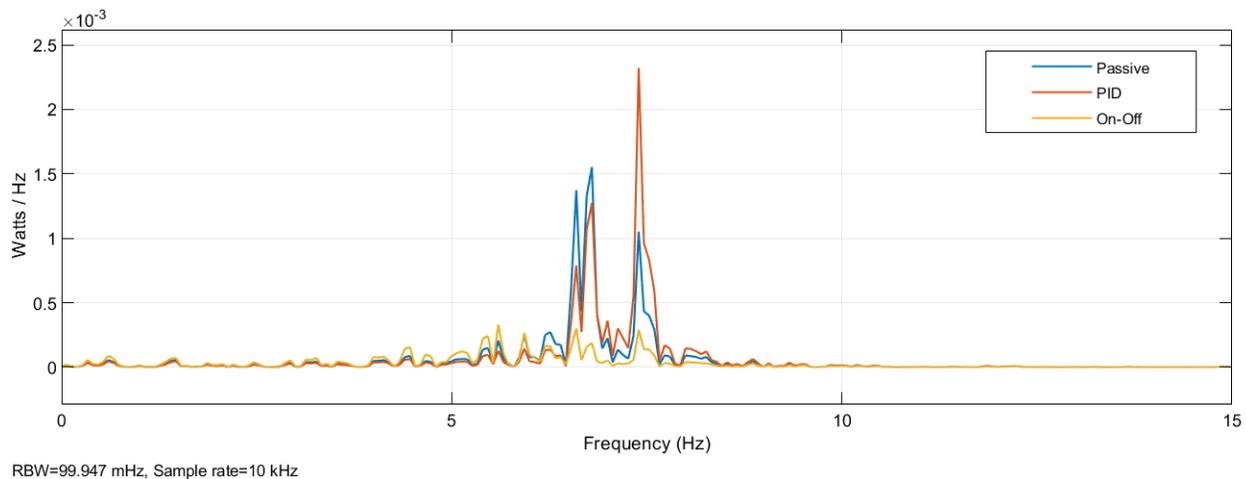
Figure 6-26: PSD Comparison of Passive, PID, and On-Off Systems subject to White Noise Input

117
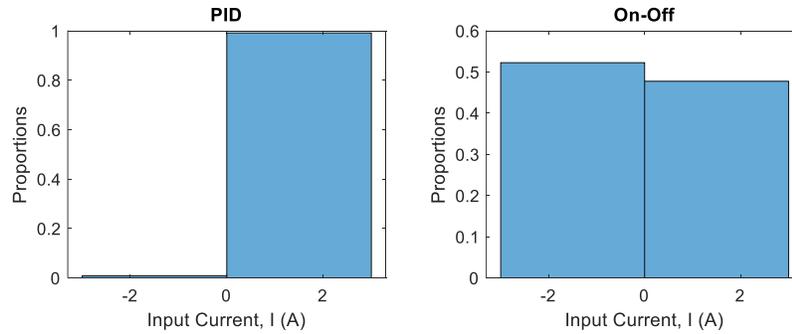
Figure 6-27: Histogram of PID and On-Off Controllers under White Noise Loading

Overall, the on-off controller provides the best random vibration control. This can be seen in both the time response and associated PSD. The fact that the PSD of the on-off system shows a distribution of power across all frequencies directly results in a lower RMS displacement. The passive and PID_{Ts} systems have the same RMS displacement, which is attributed to both systems having nearly similar PSDs.

6.5   Summary

The performance of the passive, PID, and on-off control systems undergoing different loading scenarios has been investigated to understand their behavior and to demonstrate their capabilities in attenuating vibration. Comparison of the two online types of controllers, PID and on-off, show that the on-off controller performs better under all loading conditions except for harmonic input having frequency of 5.14 Hz.

The gain of the PID controller depends on the loading condition. For shock loading, the PID_{Ts} gains are used as they minimize settling time. For harmonic loading, gain scheduling can be used to alternate between the PID_X and PID_P gains to attenuate vibration for all input frequencies. For random loading, either PID_X or PID_{Ts} gains can be used since they perform almost equally well. In essence, gain scheduling can be implemented to attenuate vibration for all loading conditions, where the gains are controlled by some logic controller.

The offline controllers designed by NLP show that the on-off controller is a type of optimal controller for minimizing settling time with the exception that those designed by NLP can take intermediate values of current between -3 and 3 A. Furthermore, NLP controllers designed for minimal state energy under harmonic loading tends to shift the natural frequency away from the input frequency, suggesting another possible optimal controller. This possible optimal controller is

118

simply an adaptive passive system, where the controller simply shifts the natural frequency away from the input frequency at constant current.

Overall, these results demonstrate that control by boundary conditioning using MRE is feasible for certain types of controllers. Because the mechanical system has a wide range of natural frequencies that was made possible by a larger-sized electromagnet, this allowed for good levels of attenuation for a wide range of input frequencies. Thus, control via boundary condition is an alternative method of attenuating vibrations for different loading conditions.

Chapter 7: Contributions, Conclusions, and Future Work

7.1 Contributions

The purpose of this present research study is to present a novel approach in the control of flexible beams for lightweight applications through boundary conditioning using an MRE-based system. Most previous research on the topic of vibration control of flexible structures were based on sandwich structures using MRE as the core layer; however, there appears to be a lack in alternative control approaches, as discussed in the literature review. The proposed design using MRE at the support opens the way for possibly new control techniques, and the contributions of this research are as follows:

    i.   Vibration control of flexible structures through the support. Normally, beam supports are rigid, but the new design proposes to make the supports flexible by introducing MRE.

    ii.   Increase in the fundamental frequency shift due to larger-sized electromagnets. No size constraint is placed on the electromagnet, thus being able to maximize the magnetic flux density such that the mechanical properties of the MRE saturate.

    iii.   Applications for light-weight operations with beams having a small payload that may be sensitive to vibrations.

    iv.   Applications for already existing beams. The proposed design can be fitted retroactively and does not require a change of structure to the sandwich type since the MRE is in a separate external control unit.

7.2 Conclusions

This research demonstrates the use of MRE as a means of controlling flexible structures through boundary conditioning. The proof-of-concept was conducted for a cantilever beam using an overhanging beam as an alternative such that the overhang support can be made flexible using MRE. Different control methods were implemented on the proposed model, such as PID, on-off, and those developed through NLP to adaptively tune the MRE for vibration attenuation. The conclusions drawn from this research are the following:

    i.   Design of the electromagnet is not limited by its weight. In general, a larger-sized electromagnet is required to generate higher magnetic flux densities. Previous control

strategies required the electromagnet being mounted on the beam; thus, size and weight were a constraint. Without this limitation, the electromagnet can be designed to reach a magnetic flux density which would saturate the mechanical properties of the MRE.

ii. The rigidity of any boundary condition can be controlled by introducing an MRE-based system at the support. The larger-sized electromagnet allows the MRE-based support to have a wide range of stiffness and damping, thus leading to a larger frequency shift under changing magnetic flux densities.

iii. Different controller laws can be implemented to adjust the rigidity of the MRE-based boundary condition to attenuate vibrations. The on-off controller showed the best performance in attenuating vibrations for almost every case, whereas the PID performed poorly.

7.3 Future Work

The present research study has provided an essential guidance on application of MRE technology to semi-actively attenuate vibration through boundary conditioning. Several limitations and assumptions have been made to facilitate the development of the model and design optimization method. For instance, MRE model was assumed to be independent of frequency and strain amplitude in the studied frequency range, thus effects of strain softening and frequency stiffening typically observe in MREs are ignored. Also, the proposed overhang beam with MRE support does not accurately represent the cantilever beam model. The electromagnet to activate the MRE has been designed through trial and error as the weight of electromagnet was not a primary constraint. Moreover, while on-off control performed well, they are inherently subject to chattering. Due to these limitations, the following are recommended areas for future work:

i. Investigate the validity of the developed model by conducting an experimental study.

ii. Develop the current MRE model by incorporating the effect of strain amplitude and frequency besides the magnetic field to account for the effect of softening and stiffening in MRE due to strain amplitude and frequency, respectively. This will allow to design the beam to have higher deflections, which can lead to different applications.

iii. Perform theoretical and experimental studies on the alternative beam model using MRE under torsion at the support, which is representative of a torsional spring. This

will accurately represent the cantilever beam model as rigidity of the torsional spring becomes very large.

iv.   Explore different control laws, such as ANN, to overcome the limitations present in the controllers used in this study. Previous studies have shown that ANN is capable of also overcoming the issues of nonlinearity present in the MRE and also issues associated with the PID, on-off, and other conventional controllers. Furthermore, control methods specifically dedicated to LTV systems can be explored.

v.   Improve the current control strategies employed in this study. Gain scheduling can be applied to the PID controllers such that proper gains can be utilized under different loading conditions. Modification to the on-off controller can be done to minimize the chattering effect.

vi.   Design of the electromagnet using optimization. The current design of the electromagnet was done through an ad-hoc trial-and-error method in determining the dimensions. The dimensions and material selection can be optimized to reduce the weight while maximizing the magnetic flux density at the MRE region.

vii.   Application on different flexible structures such as plates and beams subject to different boundary conditions.

viii.   Enhancement of the model by including a payload at the tip of the beam, which would be more representative of a light-weight load-carrying application.

References

[1] D. Miljković, *Review of Active Vibration Control*. 2009.

[2] A. Rasooli, R. Sedaghati, Q. Concordia University (Montréal, and Q. D. of M. Concordia University (Montréal Industrial and Aerospace Engineering., "Fabrication, Characterization and Control of a Novel Magnetorheological Elastomer-based Adaptive Tuned Vibration Absorber," [Concordia University], [Montréal, Québec], 2021. [Online]. Available: https://spectrum.library.concordia.ca/id/eprint/987877/

[3] N. Hoang, N. Zhang, and H. Du, "An adaptive tunable vibration absorber using a new magnetorheological elastomer for vehicular powertrain transient vibration reduction," *Smart Materials and Structures*, vol. 20, no. 1, 2011, doi: 10.1088/0964-1726/20/1/015019.

[4] Y.-K. Kim, J. H. Koo, K.-S. Kim, and S. H. Kim, "Suppressing harmonic vibrations of a miniature cryogenic cooler using an adaptive tunable vibration absorber based on magneto-rheological elastomers.," *The Review of scientific instruments*, vol. 82, no. 3, p. 035103, 2011, doi: 10.1063/1.3553198.

[5] U.-C. Jeong, "Application of Adaptive Tuned Magneto-Rheological Elastomer for Vibration Reduction of a Plate by a Variable-Unbalance Excitation," vol. 10, no. 3934, p. 3934, 2020, doi: 10.3390/app10113934.

[6] Y. T. Choi and N. M. Wereley, "Adaptively tunable magnetorheological elastomer-based vibration absorber for a propeller aircraft seat," vol. 12, no. 3, pp. 035332–035332, 2022, doi: 10.1063/9.0000323.

[7] T. Komatsuzaki and Y. Iwata, "Design of a Real-Time Adaptively Tuned Dynamic Vibration Absorber with a Variable Stiffness Property Using Magnetorheological Elastomer," *Shock and Vibration*, vol. 2015, p. 676508, Jul. 2015, doi: 10.1155/2015/676508.

[8] X. Gu, Y. Yu, Y. Li, J. Li, M. Askari, and B. Samali, "Experimental study of semi-active magnetorheological elastomer base isolation system using optimal neuro fuzzy logic control," *Mechanical Systems and Signal Processing*, vol. 119, pp. 380–398, 2019, doi: 10.1016/j.ymssp.2018.10.001.

[9] T. Jin *et al.*, "Development and evaluation of a versatile semi-active suspension system for high-speed railway vehicles," *Mechanical Systems and Signal Processing*, vol. 135, 2020, doi: 10.1016/j.ymssp.2019.106338.

[10] C. Liu, M. Hemmatian, R. Sedaghati, and G. Wen, "Development and Control of Magnetorheological Elastomer-Based Semi-active Seat Suspension Isolator Using Adaptive Neural Network," vol. 7, 2020, doi: 10.3389/fmats.2020.00171.

[11] X. B. Nguyen, H. T. Truong, and T. Komatsuzaki, "Novel semiactive suspension using a magnetorheological elastomer (MRE)-based absorber and adaptive neural network controller for systems with input constraints," *Mechanical Sciences*, vol. 11, no. 2, pp. 465–479, 2020, doi: 10.5194/ms-11-465-2020.

[12] L.-J. Qian, F.-L. Xin, X.-X. Bai, and N. M. Wereley, "State observation–based control algorithm for dynamic vibration absorbing systems featuring magnetorheological elastomers: Principle and analysis," *Journal of Intelligent Material Systems and Structures*, vol. 28, no. 18, pp. 2539–2556, Nov. 2017, doi: 10.1177/1045389X17692047.

[13]   M. A. Khanouki, R. Sedaghati, and M. Hemmatian, "Multidisciplinary Design Optimization of a Novel Sandwich Beam-Based Adaptive Tuned Vibration Absorber Featuring Magnetorheological Elastomer," *Materials*, vol. 13, no. 10, 2020, doi: 10.3390/ma13102261.

[14]   M. Long, G. L. Hu, and S. L. Wang, "Vibration Response Analysis of MRE Cantilever Sandwich Beam under Non-Homogeneous Magnetic Fields," *Applied Mechanics and Materials*, vol. 303–306, pp. 49–52, 2013, doi: 10.4028/www.scientific.net/AMM.303-306.49.

[15]   B. V. Ramesh, R. Vasudevan, N. B. Kumar, and peer reviewed papers from the 2014 I. M. E. C. (IMEC 2014) Selected June 13-15, 2014, Tamil Nadu, India, "Vibration Analysis of a Laminated Composite Magnetorheological Elastomer Sandwich Beam," *Applied Mechanics and Materials*, vol. 592–594, pp. 2097–2101, 2014, doi: 10.4028/www.scientific.net/AMM.592-594.2097.

[16]   U. Sharif *et al.*, "Dynamic Behavior of Sandwich Structures with Magnetorheological Elastomer: A Review," vol. 14, no. 7025, p. 7025, 2021, doi: 10.3390/ma14227025.

[17]   R. Selvaraj and M. Ramamoorthy, "Dynamic analysis of laminated composite sandwich beam containing carbon nanotubes reinforced magnetorheological elastomer," *Journal of Sandwich Structures & Materials*, vol. 23, no. 5, pp. 1784–1807, 2021, doi: 10.1177/1099636220905253.

[18]   K. Wei, G. Meng, W. Zhang, and S. Zhu, "Experimental investigation on vibration characteristics of sandwich beams with magnetorheological elastomers cores," *Journal of Central South University of Technology : Science & Technology of Mining and Metallurgy*, vol. 15, no. 1, pp. 239–242, 2008, doi: 10.1007/s11771-008-0354-7.

[19]   G. Hu, M. Guo, W. Li, H. Du, and G. Alici, "Experimental investigation of the vibration characteristics of a magnetorheological elastomer sandwich beam under non-homogeneous small magnetic fields," *Smart Materials and Structures*, vol. 20, no. 12, 2011, doi: 10.1088/0964-1726/20/12/127001.

[20]   U. R. Poojary, S. Hegde, K. Kiran, and K. V. Gangadharan, "Dynamic response of a MRE sandwich structure under a non-homogenous magnetic field," *Journal of the Korean Physical Society*, vol. 79, no. 9, pp. 864–873, 2021, doi: 10.1007/s40042-021-00281-1.

[21]   T. Soleymani and A. G. Arani, "On aeroelastic stability of a piezo-MRE sandwich plate in supersonic airflow," *Composite Structures*, vol. 230, 2019, doi: 10.1016/j.compstruct.2019.111532.

[22]   S. Bornassi, H. M. Navazi, and H. Haddadpour, "Coupled bending-torsion flutter investigation of MRE tapered sandwich blades in a turbomachinery cascade," *Thin-Walled Structures*, vol. 152, 2020, doi: 10.1016/j.tws.2020.106765.

[23]   W. Brogan, *Modern Control Theory*, 3rd ed. Upper Saddle River, NJ: Prentice Hall.

[24]   R. Dorf and R. Bishop, *Modern Control Systems*, 12th ed. Upple Saddle River, NJ: Prentice Hall, 2011.

[25]   S. Rao, *Mechanical Vibrations*, 6th ed. Hoboken, NJ: Pearson Education, Inc., 2017.

[26]   P. Wirsching, T. Paez, and K. Ortiz, *Random Vibrations: Theory and Practice*. New York: Dover, 2006.

[27]   E. Guglielmino, T. Sireteanu, C. Stammers, G. Ghita, and M. Giuclea, *Semi-Active Suspension Control: Improved Vehicle Ride and Road Friendliness*. Springer-Verlag London Limited, 2008.

[28]   Z. Shiller, "Off-Line and On-Line Trajectory Planning," in *Mechanisms and Machine Science*, vol. 29, 2015, pp. 29–62. doi: 10.1007/978-3-319-14705-5_2.

[29]   F. Lewis, D. Vrabie, and V. Syrmos, *Optimal Control*, 3rd ed. Hoboken, NJ: John Wiley & Sons, Inc.

[30]   D. Karnopp, "Active and Semi-Active Vibration Isolation," *J. Vib. Acoust*, vol. 117, no. B, pp. 177–185, 1995, doi: 10.1115/1.2838660.

[31]   M. VALÁŠEK, M. NOVÁK, Z. ŠIKA, and O. VACULÍN, "Extended Ground-Hook - New Concept of Semi-Active Control of Truck's Suspension," *Vehicle System Dynamics*, vol. 27, no. 5–6, pp. 289–303, Jun. 1997, doi: 10.1080/00423119708969333.

[32]   S. Rakheja and S. Sankar, "Vibration and Shock Isolation Performance of a Semi-Active 'On-Off' Damper," *Journal of Vibration, Acoustics, Stress, and Reliability in Design*, vol. 107, no. 4, pp. 398–403, Oct. 1985, doi: 10.1115/1.3269279.

[33]   D. W. Felt, M. Hagenbuchle, J. Liu, and J. Richard, "Rheology of a Magnetorheological Fluid," *Journal of Intelligent Material Systems and Structures*, vol. 7, no. 5, pp. 589–593, Sep. 1996, doi: 10.1177/1045389X9600700522.

[34]   E. Lemaire *et al.*, "Influence of the particle size on the rheology of magnetorheological fluids," *Journal of Rheology*, vol. 39, no. 5, pp. 1011–1020, Sep. 1995, doi: 10.1122/1.550614.

[35]   X. Zhang, X. Liu, R. Xiaohui, J. Zhao, and X. Gong, "The Influence of Additives on the Rheological and Sedimentary Properties of Magnetorheological Fluid," *Frontiers in Materials*, vol. 7, doi: 10.3389/fmats.2020.631069.

[36]   T. Ma *et al.*, "Optimized Fuzzy Skyhook Control for Semi-Active Vehicle Suspension with New Inverse Model of Magnetorheological Fluid Damper," vol. 14, no. 1674, p. 1674, 2021, doi: 10.3390/en14061674.

[37]   X. Liu *et al.*, "A new AI-surrogate model for dynamics analysis of a magnetorheological damper in the semi-active seat suspension," vol. 29, no. 3, 2020, doi: 10.1088/1361-665X/ab6ba5.

[38]   A. Boltoşi, C. Opriţescu, and A. Ţîrdea, "Magneto Rheological Semi-Active Damper with External By-pass Circuit in Modular Structure," vol. XVII, no. 2, pp. 41–48, 2010.

[39]   Ö. Şahin *et al.*, "A comparative evaluation of semi-active control algorithms for real-time seismic protection of buildings via magnetorheological fluid dampers," *Journal of Building Engineering*, vol. 42, 2021, doi: 10.1016/j.jobe.2021.102795.

[40]   W. He, Q. Ouyang, H. Hu, X. Ye, and L. Lin, "Semi-active control of crankshaft skyhook based on magnetorheological torsional damper," vol. 9, 2022, doi: 10.3389/fmats.2022.933076.

[41]   K. E. Majdoub, F. Giri, and F.-Z. Chaoui, "Adaptive Backstepping Control Design for Semi-Active Suspension of Half-Vehicle With Magnetorheological Damper," *IEEE/CAA Journal of Automatica Sinica*, vol. 8, no. 3, 2021, doi: 10.1109/JAS.2020.1003521.

[42]   J. Yang *et al.*, "A semi-active suspension using a magnetorheological damper with nonlinear negative-stiffness component," *Mechanical Systems and Signal Processing*, vol. 147, 2021, doi: 10.1016/j.ymssp.2020.107071.

[43]   B. Kasemi, A. G. A. Muthalif, M. M. Rashid, and S. Fathima, "Fuzzy-PID Controller for Semi-Active Vibration Control Using Magnetorheological Fluid Damper," *Procedia Engineering*, vol. 41, pp. 1221–1227, 2012, doi: 10.1016/j.proeng.2012.07.304.

[44]   A. Alrefaie, M. Ibrahim, H. Ibrahim, and C. S. and A. C. (CCE) M. C. 2022 19th International Conference on Electrical Engineering Mexico 2022 Nov. 9.-2022 Nov. 11, "Semi-Active Road-Vehicle Dynamics by implementing Neuro-Fuzzy Controlled damper," in *2022 19th International Conference on Electrical Engineering, Computing Science and Automatic Control (CCE)*, IEEE, 2022, pp. 1–5. doi: 10.1109/CCE56709.2022.9975986.

[45]   C. Poussot-Vassal, O. Sename, L. Dugard, R. Ramirez-Mendoza, and L. Flores, "OPTIMAL SKYHOOK CONTROL FOR SEMI-ACTIVE SUSPENSIONS," *IFAC Proceedings Volumes*, vol. 39, no. 16, pp. 608–613, 2006, doi: 10.3182/20060912-3-DE-2911.00106.

[46]   J. Rabinow, "The Magnetic Fluid Clutch," *Transactions of the American Institute of Electrical Engineers*, vol. 67, no. 2, 1948, doi: 10.1109/T-AIEE.1948.5059821.

[47]   S. Segla and M. Orecny, "Balance Control of Semiactive Seat Suspension with Elimination of Dynamic Jerk," *Procedia Engineering*, vol. 96, pp. 419–427, 2014, doi: 10.1016/j.proeng.2014.12.111.

[48]   Aji Masa'id, Bhre Wangsa Lenggana, U. Ubaidillah, Didik Djoko Susilo, and Seung-Bok Choi, "A Review on Vibration Control Strategies Using Magnetorheological Materials Actuators: Application Perspective," vol. 12, no. 113, p. 113, 2023, doi: 10.3390/act12030113.

[49]   M. Valasek, M. Babic, Z. Sika, and L. Magdolen, "Development of Semi-Active Truck Suspension," *IFAC Proceedings Volumes*, vol. 30, no. 8, pp. 467–472, Jun. 1997, doi: 10.1016/S1474-6670(17)43865-1.

[50]   H.-S. Lee and S.-B. Choi, "Control and Response Characteristics of a Magneto-Rheological Fluid Damper for Passenger Vehicles," *Journal of Intelligent Material Systems and Structures*, vol. 11, no. 1, pp. 80–87, Jan. 2000, doi: 10.1106/412A-2GMA-BTUL-MALT.

[51]   M. Zapateiro, N. Luo, H. R. Karimi, and J. Vehí, "Vibration control of a class of semiactive suspension system using neural network and backstepping techniques," *Mechanical Systems and Signal Processing*, vol. 23, no. 6, pp. 1946–1953, 2009, doi: 10.1016/j.ymssp.2008.10.003.

[52]   S. S. Kang, K. Choi, J.-D. Nam, and H. J. Choi, "Magnetorheological Elastomers: Fabrication, Characteristics, and Applications.," *Materials (Basel)*, vol. 13, no. 20, Oct. 2020, doi: 10.3390/ma13204597.

[53]   A. M. H. Salem, A. Ali, R. B. Ramli, A. G. A. Muthalif, and S. Julai, "Effect of Carbonyl Iron Particle Types on the Structure and Performance of Magnetorheological Elastomers: A Frequency and Strain Dependent Study.," *Polymers (Basel)*, vol. 14, no. 19, Oct. 2022, doi: 10.3390/polym14194193.

[54]   A. Franck, "Viscoelasticity and Dynamical Mechanical Testing," TA Instruments, Germany.   Accessed: Aug.   05,   2023.   [Online].   Available: https://www.tainstruments.com/pdf/literature/AAN004_Viscoelasticity_and_DMA.pdf

[55]   A. Boczkowska and S. Awietjan, "Microstructure and Properties of Magnetorheological Elastomers," in *Advanced Elastomers*, A. Boczkowska, Ed., Rijeka: IntechOpen, 2012, p. Ch. 6. doi: 10.5772/50430.

[56]   J. Winger, M. Schümann, A. Kupka, and S. Odenbach, "Influence of the particle size on the magnetorheological effect of magnetorheological elastomers," *Journal of Magnetism and Magnetic Materials*, vol. 481, pp. 176–182, 2019, doi: 10.1016/j.jmmm.2019.03.027.

[57]   N. Moksin, R. K. Shuib, H. Ismail, and M. K. Harun, "Frequency and Amplitude Dependence of Magnetorheological Elastomers Composites," *IOP Conference Series: Materials Science and Engineering*, vol. 548, no. 1, p. 012006, 2019, doi: 10.1088/1757-899X/548/1/012006.

[58]   M. Norouzi, S. M. Sajjadi Alehashem, H. Vatandoost, Y. Q. Ni, and M. M. Shahmardan, "A new approach for modeling of magnetorheological elastomers," *Journal of Intelligent Material Systems and Structures*, vol. 27, no. 8, pp. 1121–1135, 2016, doi: 10.1177/1045389X15615966.

[59]   Y. Yu, Y. Li, and J. Li, "Nonparametric modeling of magnetorheological elastomer base isolator based on artificial neural network optimized by ant colony algorithm," *Journal of Intelligent Material Systems and Structures*, vol. 26, no. 14, pp. 1789–1798, 2015, doi: 10.1177/1045389X15577649.

[60]   M. A. Tariq, M. Usman, S. H. Farooq, I. Ullah, and A. Hanif, "Investigation of the Structural Response of the MRE-Based MDOF Isolated Structure under Historic Near- and Far-Fault Earthquake Loadings," vol. 11, no. 2876, p. 2876, 2021, doi: 10.3390/app11062876.

[61]   H. NISHIMURA, T. KOMATSUZAKI, and Y. MATSUMURA, "Wave absorption control of a lumped mass system using a dynamic absorber with variable stiffness property," vol. 89, no. 920, pp. 22–00257, 2023, doi: 10.1299/transjsme.22-00257.

[62]   Y.-Q. Guo, J. Zhang, D.-Q. He, and J.-B. Li, "Magnetorheological Elastomer Precision Platform Control Using OFFO-PID Algorithm," vol. 2020, 2020, doi: 10.1155/2020/3025863.

[63]   X. B. Nguyen, T. Komatsuzaki, Y. Iwata, and H. Asanuma, "Fuzzy Semiactive Vibration Control of Structures Using Magnetorheological Elastomer," *Shock and Vibration*, vol. 2017, 2017, doi: 10.1155/2017/3651057.

[64]   Q. Yang, Y. Yang, Q. Wang, and L. Peng, "Study on the fluctuating wind responses of constructing bridge towers with magnetorheological elastomer variable stiffness tuned mass damper," *Journal of Intelligent Material Systems and Structures*, vol. 33, no. 2, pp. 290–308, 2022, doi: 10.1177/1045389X211014574.

[65]   T. Szmidt, D. Pisarski, R. Konowrocki, S. Awietjan, and A. Boczkowska, "Adaptive Damping of a Double-Beam Structure Based on Magnetorheological Elastomer," *Shock and Vibration*, vol. 2019, 2019, doi: 10.1155/2019/8526179.

[66]   Y. Ni, Z. Ying, and Z. Chen, "Magneto-rheological elastomer (MRE) based composite structures for micro-vibration control," *Earthquake Engineering and Engineering Vibration*, vol. 9, no. 3, pp. 345–356, 2010, doi: 10.1007/s11803-010-0019-z.

[67]   V. Rajamohan, R. Sedaghati, and S. Rakheja, "Optimal vibration control of beams with total and partial MR-fluid treatments," *Smart Materials and Structures*, vol. 20, no. 11, p. 115016, Oct. 2011, doi: 10.1088/0964-1726/20/11/115016.

[68] A. Fitzgerald, *Electric Machinery*, 7th ed. McGraw Hill, 2013.

[69] W. Callister and D. Rethwisch, *Materials Science and Engineering: An Introduction*, 8th ed. Hoboken, NJ: John Wiley & Sons, Inc., 2010.

[70] P. B. Nguyen and S. Choi, "A new approach to magnetic circuit analysis and its application to the optimal design of a bi-directional magnetorheological brake," *Smart Materials and Structures*, vol. 20, p. 125003, Nov. 2011, doi: 10.1088/0964-1726/20/12/125003.

[71] Remington Industries, "Remington Copper and Magnet Wire Data Chart." Accessed: Jul. 03, 2023. [Online]. Available: https://www.remingtonindustries.com/content/Remington%20Copper%20and%20Magnet%20Wire%20Data%20Chart.pdf

[72] The Engineering Toolbox, "Copper Wire - Electrical Resistance vs. Gauge." Accessed: Aug. 02, 2023. [Online]. Available: https://www.engineeringtoolbox.com/copper-wire-d_1429.html

[73] K&J Magnetics, "K&J Magnetics - Specifications," Neodymium Magnet Physical Properties. Accessed: Aug. 02, 2023. [Online]. Available: https://www.kjmagnetics.com/specs.asp

[74] Finite Element Method Magnetics, "NdFeB Properties." Accessed: Jun. 17, 2023. [Online]. Available: https://www.femm.info/wiki/NeoProperties

[75] LORD Corporation, "Lord Technical Data: MRF-132DG Magneto-Rheological Fluid." Lord Corporation, 2019. Accessed: Jun. 17, 2023. [Online]. Available: https://lordfulfillment.com/pdf/44/DS7015_MRF-132DGMRFluid.pdf

[76] Finite Element Method Magnetics, "Open Boundary Example," Open Boundary Example. Accessed: Aug. 02, 2023. [Online]. Available: https://www.femm.info/wiki/OpenBoundaryExample

[77] S. Rao, *Vibration of Continuous Systems*, 2nd ed. Hoboken: John Wiley & Sons, Inc., 2006. doi: 10.1002/9780470117866.ch17.

[78] G. Szego 1895-, *Orthogonal polynomials / by Gabor Szego*. in Colloquium publications (American Mathematical Society); v. 23., no. Accessed from https://nla.gov.au/nla.cat-vn2358422. Providence: American Mathematical Society, 1939.

[79] D. Zill and M. Cullen, *Advanced Engineering Mathematics*, 3rd ed. Sudbury, MA: Jones and Bartlett Publishers, LLC.

[80] M. AMABILI and R. GARZIERA, "A TECHNIQUE FOR THE SYSTEMATIC CHOICE OF ADMISSIBLE FUNCTIONS IN THE RAYLEIGH–RITZ METHOD," *Journal of Sound and Vibration*, vol. 224, no. 3, pp. 519–539, Jul. 1999, doi: 10.1006/jsvi.1999.2198.

[81] The Engineering Toolbox, "Permeability," Permeability. Accessed: Aug. 11, 2023. [Online]. Available: https://www.engineeringtoolbox.com/permeability-d_1923.html

[82] J. Arora, *Introduction to Optimum Design*, 4th ed.

[83] A. Chopra, *Dynamics of Structures: Theory and Application to Earthquake Engineering*, 3rd ed. Upple Saddle River, NJ: Prentice Hall.

[84] A. Gilat, *Numerical Methods for Engineers and Scientists*, 3rd ed. Hoboken, NJ: John Wiley & Sons, Inc., 2014.

[85]   W. Thomson and M. Dahleh, *Theory of Vibration with Applications*, 5th ed. Upper Saddle River, NJ: John Wiley & Sons, Inc.

[86]   The Mathworks, Inc., "Band-Limited White Noise." Accessed: Jul. 26, 2023. [Online]. Available: https://www.mathworks.com/help/simulink/slref/bandlimitedwhitenoise.html

[87]   L. A. Manita, "Optimal operating modes with chattering switching in manipulator control problems," *Journal of Applied Mathematics and Mechanics*, vol. 64, no. 1, pp. 17–24, 2000, doi: 10.1016/S0021-8928(00)00021-6.